

Direct Energy Bandgap Group IV Alloys and Nanostructures

Thesis by

Regina Ragan

In Partial Fulfillment of the Requirements

for the Degree of

Doctor of Philosophy



California Institute of Technology

Pasadena, California

2002

(Submitted January 2, 2002)

© 2002

Regina Ragan

All Rights Reserved

This thesis is dedicated to

Calum Andrew Ragan

The sweetest angel who has ever lived

Acknowledgements

It is with great pleasure that I thank and acknowledge the many people who have contributed to my thesis as well as to my academic career and life over the past several years. I have had the good fortune to work with and learn from many talented people at Caltech. I thank my thesis advisor, Harry Atwater, for being an enthusiastic scientist. Harry gave me an enormous amount of encouragement in my graduate career. Harry also provided opportunities for me to attend many scientific conferences where I could be further inspired. Besides Harry's contagious excitement, he was critical in providing unlimited ideas. Channing Ahn gave me infinite support in the area of transmission electron microscopy. I am forever indebted to Channing (*I hope I do not regret putting this in writing*) for his scientific insight as a collaborator as well as his expertise in working with the microscope. In addition, Channing was always there when I simply needed a friend to talk. I thank my other scientific collaborators whom I worked with during my Ph.D. Jon Guyer, I thank for the work we were able to do on kinetic modeling of growth instabilities. Thanks to Mark Goorsky for X-ray analysis. I thank Shouleh Nikzad, Douglas Bell and Peter Möck for stimulating scientific discussions.

I thank Bill Johnson, Tom McGill, Kerry Vahala, and Brent Fultz for serving on my candidacy committee and teaching my core courses. Thanks to

Michael Ortiz and Steve Quake for serving on my defense committee. I must also thank those who molded me during my undergraduate career, my two undergraduate advisors, Eli Yablonovitch and Delroy Baugh. I give special thanks to Del who introduced me to the wonders and complexity of quantum mechanics. He spent countless hours answering my questions and has been a good friend over the years. Had it not been for Del, I would have a MBA and be making a high salary now. *Maybe I should not be thanking him.*

I want to thank the many people in the Atwater group who trained me to use the equipment in the lab and to survive as a graduate student. Although I had little overlap with my predecessor, Gang He, I must thank him for the time he spent training me as well as the numerous slides and schematics I was able to use in my early presentations. Kyu Sung Min was there to discuss my research and help me fix the MBE chamber. Maggie Taylor trained me to use the X-ray diffractometer and shared many amusing stories with me. I enjoyed the ski trips and ethnic dinners out with Kyu and Maggie. *(Unfortunately, we never wrote our Dilbert at Caltech cartoon strip.)* Claudine Chen trained me to make TEM cross sections. I owe her much for her help in formatting this thesis. *(Sorry, not enough to become a vegetarian.)* Elizabeth Boer taught me about plumbing and soldering. She also was first to congratulate me when I passed candidacy. Renato Camata taught me how to perform RBS. Thanks to Michael Easterbrook and Rob Gorris, the technicians who maintained the accelerator. There are other previous Atwater group members whom I would like to thank: Jimmy Yang, Kirill

Scheglov and Joseph Christopherson who taught me to use the MBE chamber and organized the bolts.

There are many talented people remaining in the Atwater group whom I have learned from and with whom I have enjoyed interactions. Rhett Brewer is an excellent scientist and competent programmer and furthermore is extremely talented in fixing equipment. I have been fortunate to have him as a colleague and friend; *I am ignoring the fact that I had to guard my chamber from his green eyes.* Martha Gallivan and I persevered together and managed to make an operational MBE chamber despite design flaws with the heater and electron gun. I have enjoyed my friendship and coffee breaks with Jason Holt in addition to many interesting scientific discussions (*especially about multi-phonon processes*). I must thank Maribeth Swaitek, Julie Casperson, and Claudine Chen for getting up early in the morning to go to the gym with me and of course for their friendship. I enjoyed Aditi Risbud's cheery personality and tenacity as a SURF student under my supervision. I thank Vanessa Sih who was also a SURF student under my supervision. I have had countless hours of fun sharing an office with Ben Kauffman, Cecily Ryan and Jimmy Zahler. Thanks to Cecily for the foresight in installing a CD writer that allowed me to back up my thesis. *Jimmy, thanks for the analysis regarding ultra-thin materials.* I have enjoyed interactions with the new crop of students Tao Feng, Rob Walters, Andrea Martin, Beth Lachut, and Luke Sweatlock.

I have also had the pleasure of meeting some very talented Post Docs: John Hartman, David Boyd, Anna Fontcuberta Morral, Mark Brongersma and Pieter Kik and research scientist, Chang-Geun Ahn. I give special thanks to Mark and Pieter, both of whom helped me as a young ignorant graduate student during my first visit to Albert Polman's Group at the FOM institute in Amsterdam, the Netherlands and later became post-docs in the Atwater group. Pieter was also critical in helping me prepare my job interview talks (*maybe a little too critical*).

I have had the good fortune to visit other research groups. I thank Angelo Mascarenhas for hosting my visit to NREL. In addition, I thank Sebastian Francoeur and Jason Verley for helping me in the lab at NREL and Andrew Norman for helping with my education on growth instabilities. I also thank Albert Polman for inviting me to visit his lab at the FOM institute on two occasions. I thank Lenneke Slooff, Mark and Pieter for help during my first visit. Regarding the second visit, I thank Michiel de Dood for helping with the details of the trip as well as help in the lab. I thank Max Siem for training me to operate the accelerator. Thanks to Jeroen Kalkman, Teun van Dillen and Christof Strohhöfer for their help as well. Special thanks I give to Christof for entertaining me, *especially for taking me to the forever memorable mime show*, for being an empathetic ear regarding the tribulation associated with writing one's thesis, and for his friendship.

I thank Carol Garland for maintaining the electron microscope so well and teaching me to be thorough when operating the TEM. Thanks to Rosalie Rowe, Lyn Hein, Eleonora Chetverikova, and Greg Dunn for their secretarial help.

I thank my family for their support and all the confidence they have had in me. Finally, I thank my husband, Matthew Ragan. Matthew has more confidence in me than anyone else and loves me more than I could have ever imagined. Matthew has taken care of Calum and me over the last month so I could write my thesis, *without a single complaint*.

Abstract

Novel group IV nanostructures were fabricated and the optical properties of such nanostructures were investigated for monolithic integration of optically active materials with silicon. The $\text{Sn}_x\text{Ge}_{1-x}$ alloy system was studied due to the previous demonstration of an indirect to direct energy bandgap transition for strain-relieved $\text{Sn}_x\text{Ge}_{1-x}$ films on Si(001). Quantum confined structures of Sn were fabricated and the optical properties were investigated. Due to the small electron effective mass of α -Sn, quantum confinement effects are expected at relatively large radii. Quantum size effects were observed in α -Sn quantum dots. Coherently strained, epitaxial $\text{Sn}_x\text{Ge}_{1-x}$ films on Ge(001) substrates were synthesized with film thickness exceeding 100 nm for the first time. The demonstration of dislocation-free $\text{Sn}_x\text{Ge}_{1-x}$ films is a step toward the fabrication of silicon-based integrated infrared optoelectronic devices. The optical properties of coherently strained $\text{Sn}_x\text{Ge}_{1-x}/\text{Ge}(001)$ alloys were investigated both theoretically and experimentally. Deformation potential theory calculations were performed to predict the effect of coherency strain on the extrema points of the conduction band and the valence band. The energy bandgap of $\text{Sn}_x\text{Ge}_{1-x}/\text{Ge}(001)$ alloys was measured via Fourier transform infrared spectroscopy. Coherency strain did not change the $\text{Sn}_x\text{Ge}_{1-x}$ energy bandgap when the strain axis was along [001] but deformation potential theory predicted

the absence of an indirect to direct energy bandgap transition when the strain axis was along [111].

In addition to being the only group IV alloy exhibiting a direct energy bandgap, when grown beyond a critical thickness, $\text{Sn}_x\text{Ge}_{1-x}/\text{Ge}(001)$ exhibits an interesting phenomenon during MBE growth. Sn segregates via surface diffusion to the crest of a surface undulation during growth and forms ordered Sn-enriched $\text{Sn}_x\text{Ge}_{1-x}$ rods oriented along [001]. The $\text{Sn}_x\text{Ge}_{1-x}$ alloy system was used as a model system to gain insight to the physical mechanisms governing self-assembly and ordering during molecular beam epitaxy.

Sn nanowires were fabricated in anodic alumina templates with lengths exceeding 1 μm and diameters on the order of 40 nm. Anodic alumina templates can be fabricated non-lithographically with ordered domains of hexagonally packed pores greater than 1 μm and pore densities on the order of 10^{11} cm^{-2} . The achievement of single crystal Sn nanowires fabricated using pressure injection in porous alumina templates was demonstrated.

The fabrication of α -Sn quantum dots embedded in Ge was achieved by annealing 1 μm thick $\text{Sn}_x\text{Ge}_{1-x}$ films. The measured diameter of the quantum dots was 32 nm and a 10% size variation was observed. Optical transmittance measurements yield a value of 0.45 eV for the direct energy bandgap as a result of quantum confinement. A high degree of tunability of the bandgap energy with the quantum dot radius is expected for α -Sn. Thus quantum-confined structures of α -Sn are promising for optoelectronic device applications

Table of Contents

Acknowledgements	iv
Abstract	ix
Table of Contents	xi
Table of Figures	xvi
List of Tables	xxiv
Chapter 1 Introduction	1
1.1 The big picture	1
1.2 Small feature sizes via self-assembly	3
1.3 A variety of integration techniques	4
1.4 Our integration approach = Outline of thesis	6
1.4.1 Bandstructure engineering via alloying	7
1.4.2 Self assembly via growth instabilities	9
1.4.3 Bandstructure engineering via quantum confinement	10
1.5 Bibliography	13
Chapter 2 Growth of Coherent, Homogeneous	
$\text{Sn}_x\text{Ge}_{1-x}/\text{Ge}(001)$ Epitaxial Films	15
2.1 Introduction	15
2.2 Molecular beam epitaxy of $\text{Sn}_x\text{Ge}_{1-x}$ alloys	18
2.3 $\text{Sn}_x\text{Ge}_{1-x}/\text{Ge}/\text{Ge}(001)$ superlattices	22

2.4	$\text{Sn}_x\text{Ge}_{1-x}/\text{Ge}_{1-x}(001)$ epitaxial films.....	31
2.4.1	Growth conditions	31
2.4.2	<i>In situ</i> crystal structure analysis.....	31
2.4.3	Post-growth film characterization	33
2.5	Thermodynamics of coherency	40
2.6	Conclusions	42
2.7	Bibliography	44
Chapter 3	Optical Characterization of Coherent, Homogeneous $\text{Sn}_x\text{Ge}_{1-x}$ Alloys	46
3.1	Introduction	46
3.2	Photoluminescence of dilute $\text{Sn}_x\text{Ge}_{1-x}/\text{Ge}(001)$ superlattices.....	49
3.3	Deformation potential theory	50
3.3.1	Background.....	50
3.3.2	Theoretical calculation for $\text{Sn}_x\text{Ge}_{1-x}/\text{Ge}(001)$ and $\text{Sn}_x\text{Ge}_{1-x}/\text{Ge}(111)$ bandstructure	51
3.3.2.1	Valence band.....	52
3.3.2.2	Conduction band.....	54
3.3.2.3	Hydrostatic component.....	57
3.3.3	Summary of DPT predictions for $\text{Sn}_x\text{Ge}_{1-x}/\text{Ge}(001)$ and $\text{Sn}_x\text{Ge}_{1-x}/\text{Ge}(111)$ bandstructure	60
3.4	Measurement of the $\text{Sn}_x\text{Ge}_{1-x}/\text{Ge}(001)$ energy bandgap	61

3.4.1	Experiment.....	61
3.4.2	Comparison between theory and experiment for Sn _x Ge _{1-x} / Ge(001).....	66
3.5	Conclusion.....	68
3.6	Bibliography.....	69
Chapter 4	Non-Lithographic Epitaxial Sn_xGe_{1-x} Dense Nanowire Arrays on Ge(001)	71
4.1	Introduction	71
4.1.1	Motivation.....	71
4.1.2	Microstructure analysis.....	72
4.1.3	Statistical analysis and comparison with theoretical models.....	73
4.1.4	Optical characterization	74
4.2	Sn _x Ge _{1-x} microstructure	74
4.2.1	Rutherford backscattering spectroscopy	75
4.2.2	Raman spectroscopy	75
4.2.3	Transmission electron microscopy analysis.....	80
4.2.4	Scanning transmission electron microscopy	87
4.3	Theoretical models of growth instabilities versus experiment.....	90
4.3.1	Description of the experiment.....	92
4.3.2	Experimental determination of instability wavelength	97

4.3.3	Thermodynamic model.....	106
4.3.3.1	Description	106
4.3.3.2	Comparison with experiment	109
4.3.4	Kinetic model.....	114
4.3.4.1	Description	114
4.3.4.2	Comparison to experiment	118
4.4	Optical characterization	120
4.5	Conclusion.....	125
4.6	Bibliography.....	128
Chapter 5	Quantum Confined Structures: Sn Nanowires and Nanocrystals	130
5.1	Introduction	130
5.2	Sn nanowires.....	132
5.2.1	Quantum confinement effects.....	132
5.2.2	Overview: Sn nanowire fabrication.....	133
5.2.3	Template fabrication.....	134
5.2.4	Sn nanowire fabrication	137
5.2.5	Sn nanowire structural characterization.....	139
5.3	α -Sn quantum dots.....	144
5.3.1	Fabrication and structural characterization	144
5.3.2	Optical characterization	155

5.4	Conclusion.....	158
5.5	Bibliography.....	160
Chapter 6	Conclusions	162

Table of Figures

Figure 1.1: Theoretical prediction of bandgap energy versus nanocrystal diameter for (a) Si and (b) Ge.	12
Figure 2.1: Binary phase diagram for Sn in Ge. [Massalski, et al 1990] The alloy forms a simple eutectic system with eutectic temperature of 231.9 °C.	16
Figure 2.2: RHEED diffraction patterns along [110] zone axis (a) before growth of Ge buffer layer and (b) after growth of Ge buffer layer.	20
Figure 2.3: RHEED pattern of 35 nm $\text{Sn}_x\text{Ge}_{1-x}$ epitaxial film with $x = 0.02$. The Bragg rods are modulated along their length.	21
Figure 2.4: Rutherford backscattering spectrum of $\text{Sn}_{0.02}\text{Ge}_{0.98}$ superlattice with 15 nm $\text{Sn}_x\text{Ge}_{1-x}$ layers and a period thickness of 70 nm. The Ge and Sn leading edge energies are represented by lines.	24
Figure 2.5: Schematic of tetragonal distortion of $\text{Sn}_x\text{Ge}_{1-x}$ unit cell on Ge(001).	26
Figure 2.6: HR-XRD ω - 2θ scan around Ge (004) Bragg reflection for the experiment (solid curve) and the simulation (open circles). The $\text{Sn}_{0.02}\text{Ge}_{0.98}$ peak is shifted to smaller values of θ .	27
Figure 2.7: TEM of analysis of a 5 period $\text{Sn}_{0.02}\text{Ge}_{0.98}/\text{Ge}$ superlattice. Imaged with (a) 2 beam conditions with $\bar{g} = [004]$ where strain contrast is visible and (b) down the [110] zone axis where the $\text{Sn}_{0.02}\text{Ge}_{0.98}$ films appear uniform in composition.	28
Figure 2.8: Cross-sectional TEM analysis of $\text{Sn}_{0.03}\text{Ge}_{0.97}$ with $t = 23$ nm. Imaged (a) with $\bar{g} = [004]$ 2 beam conditions where strain contrast is observed at the interfaces and (b) down the [110] zone axis indicating uniform Sn composition in the layer.	29

- Figure 2.9: HR-TEM image down [110] zone axis of $\text{Sn}_{0.03}\text{Ge}_{0.97}$ (a) at the $\text{Sn}_{0.03}\text{Ge}_{0.97}/\text{Ge}$ cap layer interface and (b) at the $\text{Sn}_{0.03}\text{Ge}_{0.97}/\text{Ge}$ buffer layer interface. The lattice fringes are continuous across both interfaces. The line is drawn to indicate the interface. 30
- Figure 2.10: RHEED pattern of $\text{Sn}_x\text{Ge}_{1-x}$ alloy on Ge(001) with $t = 16$ nm and $x = 0.06$. The diffraction rods have transformed into spots that is indicative of 3-dimensional growth. 32
- Figure 2.11: RBS spectra of $\text{Sn}_x\text{Ge}_{1-x}/\text{Ge}(001)$ for $x = 0.035, 0.06,$ and 0.115 and $t = 100$ nm. The Sn peaks are uniform in height and thus composition with depth. The leading edge of Sn and Ge are represented as dashed lines. 33
- Figure 2.12: Representative HR-XRD ω - 2θ scan of 100 nm $\text{Sn}_x\text{Ge}_{1-x}/\text{Ge}(001)$ films around the Ge(004) reflection. (a) with $x = 0.035, 0.06$ and 0.115 and (b) $\text{Sn}_{0.06}\text{Ge}_{0.94}$ (solid curve) overlaid with dynamical simulation (hollow circles). 36
- Figure 2.13: Comparison between calculated (solid lines) and experimentally measured strains along the growth direction, e_{zz} (triangles), and in the substrate plane, e_{xx} (squares), for 100 nm coherently-strained $\text{Sn}_x\text{Ge}_{1-x}$ films on Ge(001). 37
- Figure 2.14: $\text{Sn}_{0.06}\text{Ge}_{0.94}/\text{Ge}(004)$ imaged (a) under $\bar{g} = [004]$ 2 beam conditions and (b) along [110] zone axis at high resolution. The $\text{Sn}_{0.06}\text{Ge}_{0.94}/\text{Ge}$ interface (represented as a dashed line) has continuous lattice fringes. 39
- Figure 2.15: Thermodynamic critical thickness, solid curve, compared with experimentally determined thickness of metastable coherently strained $\text{Sn}_x\text{Ge}_{1-x}$ films on Ge(001) substrates (solid circles). The experimental film thickness exceeded the calculated thermodynamic critical thickness. 42

- Figure 3.1: Alloy effect on relaxed $\text{Sn}_x\text{Ge}_{1-x}$ bandstructure: experimental measurement (symbols) [He & Atwater, 1997] and tight-binding calculation (dotted and dashed lines) [Jenkins & Dow, 1987]. 47
- Figure 3.2: Uniaxial deformation of the $E_{V_{hh}}$ and $E_{V_{lh}}$. The lines represent strain axis along [001] and the symbols along [111]. 54
- Figure 3.3: Schematic of ellipsoidal constant energy surfaces in Ge. 55
- Figure 3.4: Uniaxial splitting of the conduction band at L_6 due to uniaxial strain along [111]. 57
- Figure 3.5: Energy levels versus lattice spacing for diamond.[Kimball, 1935] 58
- Figure 3.6: Hydrostatic component of ΔE_g represented by squares for strain along [111] and a line for strain along [001]. 59
- Figure 3.7: Plot of E_C , Γ for strained (closed squares) and relaxed (closed triangles) [He & Atwater, 1997], of E_C , L for strained (open squares) and relaxed (open triangles), and strained $E_{V_{lh}}$ (dotted) for $\text{Sn}_x\text{Ge}_{1-x}$ on Ge(111). E_g is shaded for the strained alloy. 60
- Figure 3.8: FTIR spectra of 100 nm thick $\text{Sn}_x\text{Ge}_{1-x}$ alloys on (a) n-type Ge(001) with $x = 0.05$ and 0.08 in reflectance mode at 50° incidence and (b) on p-type Ge(001) with $x = 0.035$, 0.06 , and 0.115 in transmittance mode at normal incidence. 65
- Figure 3.9: Measurement of coherently strained $\text{Sn}_x\text{Ge}_{1-x}/\text{Ge}(001)$ energy bandgap. Closed (open) triangles represent the Γ (L) point. 67
- Figure 3.10: Plot of E_g , Γ for strained (squares) and relaxed [He & Atwater, 1997] (triangles) for $\text{Sn}_x\text{Ge}_{1-x}$ on Ge(001). The deformation potential theory is represented by a solid line. 67
- Figure 4-1: Raman shift of zone center optical phonons for (a) 100 nm thick $\text{Sn}_x\text{Ge}_{1-x}$ alloys and (b) $1 \mu\text{m}$ thick $\text{Sn}_x\text{Ge}_{1-x}$ alloys. 78
- Figure 4-2: Raman spectra of Ge $\omega_{2TA}(x)$ and Sn $\nu_{LTO}(\Gamma_{25})$ peaks for (a) 100 nm thick $\text{Sn}_x\text{Ge}_{1-x}$ alloys and (b) $1 \mu\text{m}$ thick $\text{Sn}_x\text{Ge}_{1-x}$ alloys. 79

- Figure 4-3: Cross-sectional TEM images of $\text{Sn}_x\text{Ge}_{1-x}$ alloy with an average Sn composition of 0.03 imaged down the (a) $[110]$ zone axis and (b) $[\bar{1}\bar{1}0]$ zone axis. 81
- Figure 4-4: Schematic representing Sn-enrichment of $\text{Sn}_x\text{Ge}_{1-x}$ rods along $[001]$. 81
- Figure 4-5: $\text{Sn}_{0.03}\text{Ge}_{0.97}$ diffraction patterns taken along the (a) $[110]$ and (b) $[001]$ zone axes. In (c) the $(0\bar{6}0)$ reflection is enlarged. Arrow points to additional diffraction spot on the left. 82
- Figure 4-6: $\text{Sn}_{0.06}\text{Ge}_{0.94}/\text{Ge}(001)$ TEM images under 2 beam conditions with (a) $\bar{g} = (004)$ and (b) $\bar{g} = [\bar{1}\bar{1}\bar{1}]$. (c) HR-TEM image where the dashed line represents the interface. 83
- Figure 4-7: TEM images of $1\ \mu\text{m}$ thick $\text{Sn}_{0.03}\text{Ge}_{0.97}$ film imaged under 2 beam conditions (a) $\bar{g} = [2\bar{2}0]$ and (b) $\bar{g} = [004]$. 84
- Figure 4-8: Cross-sectional TEM images of $1\ \mu\text{m}$ thick $\text{Sn}_{0.07}\text{Ge}_{0.93}/\text{Ge}(100)$ with (a) $\bar{g} = [2\bar{2}0]$ and (b) $\bar{g} = [004]$. 86
- Figure 4-9: Schematic of STEM experiment with annular detector to image elastically scattered electrons and to exclude diffracted and transmitted beams. 87
- Figure 4-10: STEM analysis of $100\ \text{nm}$ thick $\text{Sn}_{0.06}\text{Ge}_{0.94}$ film: (a) Bright field image includes diffracted and transmitted beams and (b) dark field image includes only elastically scattered electrons. 89
- Figure 4-11: STEM images of $1\ \mu\text{m}$ thick $\text{Sn}_{0.03}\text{Ge}_{0.97}$ (a) bright field image with transmitted and diffracted beams and (b) dark field image that includes only elastically scattered electrons. 90
- Figure 4-12: Schematic demonstrating how the misfit is tuned independent of Sn composition in the $\text{Sn}_x\text{Ge}_{1-x}$ alloy film by changing the Si composition in the $\text{Si}_y\text{Ge}_{1-y}$ virtual substrate. 93

- Figure 4-13: AFM images of $\text{Si}_y\text{Ge}_{1-y}$ virtual substrates with Si composition (a) 0 (b) 0.035 (c) 0.06 and (d) 0.15. 93
- Figure 4-14: Reciprocal X-ray space maps for (a) (004) and (b) (224) reflections of the $\text{Sn}_{0.018}\text{Ge}_{0.982}/\text{Si}_{0.06}\text{Ge}_{0.94}/\text{Ge}(001)$ sample. 95
- Figure 4-15: TEM image of $\text{Sn}_{0.018}\text{Ge}_{0.982}/\text{Si}_{0.06}\text{Ge}_{0.94}/\text{Ge}(001)$ with $\bar{g}=[2\bar{2}0]$. 97
- Figure 4-16: Correlation between the measured value of the instability wavelength using (a) AFM surface morphology and (b) TEM cross-section of a 1 μm thick $\text{Sn}_{0.07}\text{Ge}_{0.93}/\text{Ge}(001)$ film. 98
- Figure 4-17: Planar view AFM images with $\epsilon = 0.5\%$ of (a) Ge/SiGe (b) $\text{Sn}_{0.018}\text{Ge}_{0.982}/\text{Ge}$. 101
- Figure 4-18: Planar view AFM images of $\text{Sn}_x\text{Ge}_{1-x}/\text{Ge}$ with $x = 0.018$ and (a) $\epsilon = 0.26\%$ (b) $\epsilon = 0.5\%$. 101
- Figure 4-19: Autocorrelation function versus wave vector for Ge/ $\text{Si}_{0.24}\text{Ge}_{0.76}$ with $\epsilon = 0.98\%$. 102
- Figure 4-20: AFM image of Ge/ $\text{Si}_{0.24}\text{Ge}_{0.76}$ film with $\epsilon = 0.98\%$. 102
- Figure 4-21: Autocorrelation versus instability wave vector for $\text{Sn}_{0.018}\text{Ge}_{0.982}/\text{Ge}(001)$ with $\epsilon = 0.264\%$. The error in determining the peak value is represented as λ_{max} and λ_{min} , referring to the minimum and maximum value of k at the peak, respectively. 103
- Figure 4-22: Autocorrelation function versus wavevector for a stochastic surface (squares) and $\text{Sn}_{0.018}\text{Ge}_{0.982}/\text{Ge}(001)$ alloy (triangles). The decay of the peak value scales as k^{-n} . The solid line represents a decay of $n = 2$ and the dashed line of $n = 4$. 104
- Figure 4-23: Autocorrelation function versus wave vector for unstrained Ge film grown at $T = 160^\circ\text{C}$. 105
- Figure 4-24: Schematic representing phase-separation of Sn to regions of positive curvature on the surface with a characteristic period of λ and Δ represents the height of the surface undulation. 108

- Figure 4-25: Autocorrelation function, $G(k)$ versus wave vector for $\text{Sn}_x\text{Ge}_{1-x}/\text{Ge}(001)$ with misfit of 0.26% and $T = 433$ K (closed squares) and $T = 623$ K (open squares). 110
- Figure 4-26: Autocorrelation function, $G(k)$ versus wave vector for Ge/SiGe and $\text{Sn}_x\text{Ge}_{1-x}/\text{SiGe}$ with $x = 0.018$ and 0.035 . The misfit of the three films is 0.5% . 110
- Figure 4-27: Experimental value for fastest growing instability wavelength versus value predicted by kinetic model. The line is a guide to the eye. 118
- Figure 4-28: Transmittance versus wavenumber for $\text{Sn}_x\text{Ge}_{1-x}$ with average Sn composition between $0 < x < 0.085$ and film thickness of $1 \mu\text{m}$. 120
- Figure 4-29: Absorption coefficient generated by simulation (closed symbols) and fit of the absorption edge (open circles) using the power law dependence on the bandgap energy and an Urbach tail for $x =$ (a) 0.05, (b) 0.07, and (c) 0.085. 124
- Figure 4-30: Bandgap energy versus Sn composition for homogeneous $\text{Sn}_x\text{Ge}_{1-x}$ alloys (triangles) and phase-separated $\text{Sn}_x\text{Ge}_{1-x}$ alloys (squares). 125
- Figure 5.1: Energy of valence band and conduction band with nanowire radius from semi-empirical tight binding calculation. 132
- Figure 5.2: Sn nanowire fabrication: (a) Polish Al foil, (b) anodize foil in oxalic acid until ordering begins, (c) etch oxide to expose patterned Al foil, (d) anodize a second time to produce ordered arrays of pores, (e) deposit a layer of Sn in UHV and (f) inject Sn into pores with Ar gas at high pressures. 134
- Figure 5.3: (a) Formation of pores during anodization process.[Jessensky,*et al.* 1998] (b) Variation of interpore spacing as a function of anodization voltage.[Li,*et al.* 1998] 135

- Figure 5.4:** Alumina templates fabricated with (a) 45 nm pores at 20 V planar view, (b) cross-section and (c) 30 nm pores anodized at 15 V. 136
- Figure 5.5:** Sn nanowires in alumina templates fabricated by method 1. Images in (a) and (b) show the fraction of filled pores was less than 1%. In (c) and (d), 20 nm nanowires of lengths exceeding 1 μm are shown. 140
- Figure 5.6:** SEM images of Sn nanowires prepared by method 2: (a) individual nanowire and (b) nanowires embedded in alumina template. 141
- Figure 5.7:** SEM images of templates after Sn pressure injection and Ar^+ ion etching. 141
- Figure 5.8:** TEM analysis of single 40 nm nanowire: (a) dark regions corresponded to Sn and (b) the diffraction pattern demonstrated that the nanowire was a single crystal. 142
- Figure 5.9:** TEM image taken down the [110] zone axis of $\text{Sn}_{0.01}\text{Ge}_{0.99}$ annealed at $T = 750\text{ }^\circ\text{C}$. Dark bands are seen to run along $[\bar{1}\bar{1}\bar{1}]$. 145
- Figure 5.10:** Cross-sectional TEM image down the [110] zone axis of a $\text{Sn}_x\text{Ge}_{1-x}$ film with $x = 0.03$ and annealed at $T = 550\text{ }^\circ\text{C}$. 146
- Figure 5.11:** MBE Grown $\text{Sn}_x\text{Ge}_{1-x}/\text{Ge}(001)$ with average Sn composition of 3% annealed post-growth at $T = 750\text{ }^\circ\text{C}$. 148
- Figure 5.12:** Size distribution of Sn nanocrystals in Ge matrix formed by post-growth annealing $\text{Sn}_{0.03}\text{Ge}_{0.97}/\text{Ge}(001)$ at $T = 750\text{ }^\circ\text{C}$. The average nanocrystal diameter is 32 nm. 148
- Figure 5.13:** HR-TEM images down [110] zone axis of MBE grown $\text{Sn}_{0.03}\text{Ge}_{0.97}/\text{Ge}(001)$ annealed at $T = 750\text{ }^\circ\text{C}$. (a) Cross-section slices a particle of diameter 28.4 nm and (b) a particle of diameter 26.5 nm is still embedded in the Ge matrix. 149

- Figure 5.14:** On the left, HR-TEM of Sn quantum dot in Ge matrix. Fourier transform of Ge and Sn quantum dot lattice fringes is seen in image on the right . 151
- Figure 5.15:** (a) On the left, HR-TEM image of Ge matrix with corresponding Fourier transform seen on the right. (b) On the left, diffraction pattern with Ge reflections subtracted and on the right is the back transform calculated from this pattern. 151
- Figure 5.16:** Indexed diffraction pattern of Sn nanocrystal observed in Figure 5.13. The Ge reflections are circled. A 5 degree tilt was observed along the [001] direction between the nanocrystal and the Ge matrix. Arrows point to Moiré reflections. 153
- Figure 5.17:** Transmittance versus wavenumber for $\text{Sn}_{0.03}\text{Ge}_{0.97}$: unannealed (line), annealed at $T = 550\text{ }^{\circ}\text{C}$ (circles), $650\text{ }^{\circ}\text{C}$ (crosses) and $750\text{ }^{\circ}\text{C}$ (triangles). 156
- Figure 5.18:** Absorption coefficient versus wavenumber calculated from best fit of simulation with experimental transmittance spectra (closed triangles) and the fit (open circles) using the functional form of the absorption coefficient for $\text{Sn}_{0.03}\text{Ge}_{0.97}$ annealed at $T = 550\text{ }^{\circ}\text{C}$. 158

List of Tables

- Table 2.1:** Description of $\text{Sn}_x\text{Ge}_{1-x}/\text{Ge}$ superlattice films on Ge(001). All superlattice structures have an approximately 200 nm Ge buffer layer and a 200 nm Ge capping layer. 25
- Table 4.1:** Experimentally determined values of instability wavelength versus the values predicted by the thermodynamic model. Double lines distinguish between sets of data with constant strain and varying Sn composition. The maximum and minimum values of λ represent the error in determining the peak value. 112
- Table 4.2:** Experimentally determined values of instability wavelength versus the values predicted by the thermodynamic model. Double lines distinguish between sets of data with constant Sn composition and varying strain. The maximum and minimum values of λ represent the error in determining the peak value. 113
- Table 5.1:** Interplanar spacing calculated from measured distance of reflection (columns 1 and 2) in comparison to known d_{hkl} spacing for $\alpha\text{-Sn}$ (column 3). The minimum (maximum) corresponds to the minimum (maximum) value calculated for the lattice spacing, taking into account measurement error. 154

Chapter 1 Introduction

1.1 The big picture

Today, we live in a society where information is passed in enormous quantities between computers through optical fibers and across wireless telephones. The end user demands that the information be passed quickly. Portable electronic devices have the additional requirements of being small, cheap and fashionable. The invention of the transistor in 1947 coupled with that of the integrated circuit in 1958 has revolutionized computation by dramatically reducing cost while increasing performance. (*The impact of the integrated circuit on modern society was deemed so important that Jack Kilby was awarded the Nobel prize in physics in 2000 for its invention.*) Yet, consumers still thirst for more. Hand-held electronic apparatuses are becoming increasingly popular and the demand for increased computational abilities and functionality in these devices grows. In order to meet these demands, a high density of components per chip and low power consumption are necessary. Multimedia services, such as interactive video, are tantalizing prospects, but wide spread use will not occur until large scale real time data transfer is actualized.

We are all familiar with Moore's law, a self-fulfilling prophecy, that states that device dimensions decrease by a factor of two every 18 months. It is self-fulfilling because Moore's law has been used as the benchmark for chip advancement in the micro-processing industry. To put this in perspective, in 1975 a chip had 5,000 transistors, in 2000 the Pentium 4 had 42 million transistors, and in 2010, a chip is expected to have 1 billion transistors. However, in order to maintain the rate of advancement of high-speed electronics, two major issues must be addressed.

One issue entails the integration of optical components with the mature technology of silicon-based electronics. Why integrate optics and electronics? you may ask. In addition to high-speed data transfer and the higher bandwidths associated with optical versus electronic signals, optical devices may also play a key role in high-speed integrated circuits. As the density of components per chip increases, the number of interconnects multiplies. A high density of interconnects increases cost and limits device performance and reliability.¹ One solution is the integration of wireless, or optical, interconnects with silicon ultra large-scale integration. Unfortunately, Si is an indirect energy bandgap semiconductor; thus, it has a low radiative efficiency and is not appropriate for optoelectronic devices in its bulk form. A major bottleneck in the integration of optoelectronics and microelectronics is the lack of Si-compatible light emitters

and detectors. Group IV elements in the periodic table are iso-electronic with Si, yet as bulk elements none of these are direct energy bandgap semiconductors.

Additionally, to further increase speed and performance in electronic devices, feature size must continue to decrease. As feature size continues to scale down, quantum effects, such as tunneling and carrier confinement, are no longer negligible. Furthermore, small features require exotic and costly lithographic techniques. But consumers require that electronics be cheap. Hence, scientists and engineers are faced with some interesting challenges.

1.2 Small feature sizes via self-assembly

As the density of components per chip increases, more exotic and costly lithographic techniques, such as extreme ultraviolet (XUV) and electron beam lithography, or physical manipulation techniques, such as atomic force microscopy, are necessary to produce small features. Self-assembly or directed self-assembly is a promising technique for producing small feature sizes, on the order of 1 nm, and can serve as a low cost alternative to e-beam and XUV lithography. A wide variety of methods are employed to fabricate self-assembled nanostructures. DNA templating may be used to pattern gold nanowires and nanospheres,² the Langmuir-Blodgett technique can produce self-assembled monolayers of molecules,^{3,4} and various epitaxial growth techniques

produce quantum dots and wires. The epitaxial growth techniques are further developed than the former two methods. Coherent Ge quantum dots are aligned by preferential growth along surface facets on mesas etched on Si(001) surfaces⁵ and uniform size and spacing is engineered through strain induced interactions between dots.⁶ Epitaxial growth of quantum wires can be achieved by preferential growth along step edges,^{7,8} and along a lattice matched crystallographic direction due to an anisotropic lattice constant.⁹ Additionally, the development of compositional uniformities during epitaxial growth can be utilized to produce quantum dots and wires.¹⁰⁻¹² A deeper understanding of the physical mechanisms leading to self-assembled quantum dots and wires is necessary in order to engineer uniform size and spacing.

1.3 A variety of integration techniques

Many integration approaches are being investigated. What about using another material for integrated circuit fabrication? Gallium arsenide integrated circuits are currently fabricated with compatible III-V materials acting as optical components. Nevertheless, Si remains the dominant material in microelectronics due to the superior passivating properties of its thermal oxide, the natural abundance of sand (low cost), and decades of research. Over 95% of

semiconductor devices sold worldwide are fabricated with Si. GaAs integrated circuits are viable only for applications where high performance outweighs cost.

One hybrid-type approach involves wafer bonding different materials to Si substrates. InGaN light-emitting diodes that have been fabricated on sapphire substrates, removed post processing and transferred to Si substrates exhibit no degradation in device performance due to layer transfer.¹³ Si has been bonded to SiO₂ as a continuous layer on wafers with diameters up to 8 inches, producing Si on insulator substrates (SOI). Increased device performance and lower power consumption has been demonstrated for SOI devices in comparison to devices fabricated on bulk Si with the same generation of technology.¹⁴ Although wafer bonding is a promising technique, issues regarding integration with Si ULSI processing, such as differing thermal expansion coefficients and inter-diffusion, must be addressed. Furthermore, wafer bonding must be automated and reproducible for cheap and reliable manufacturing.

Another approach involves the monolithic integration of novel, optically active and most importantly Si-compatible materials with Si ULSI. Bandstructure engineering of group IV elements via quantum confinement and alloying can produce dramatic changes in optical and electronic properties.^{15,16} Si nanocrystals with radii on the order of 5 nm show a blue shift in the luminescence wavelength and exhibit significantly higher luminescence

efficiencies than bulk Si.¹⁷ Carbon nanotubes exhibit semiconducting or metallic properties depending on the chiral vector of the tube and the semiconducting bandgap of the nanotube scales inversely with the radius of the tube.¹⁸ Alloying Sn and Ge produces a direct energy bandgap material by mixing a semimetal and an indirect bandgap semiconductor.¹⁵

1.4 Our integration approach = Outline of thesis

The work presented in this thesis took the latter integration approach. That is, the bandstructure, and thereby, the optical and electronic properties of Group IV elements, was manipulated via alloying and quantum confinement to achieve direct energy bandgap group IV semiconductors. Two material systems were studied from a fundamental perspective to determine if the bandstructure could be engineered such that desired optical properties, not seen in the bulk elements, evolved. $\text{Sn}_x\text{Ge}_{1-x}$ alloys have already been demonstrated to undergo an indirect to direct bandgap transition,¹⁵ but improvement of the structural properties was necessary to further progress in achieving an actual device. Thus, coherently strained $\text{Sn}_x\text{Ge}_{1-x}$ alloys were grown and the effect of coherency strain on the $\text{Sn}_x\text{Ge}_{1-x}$ bandgap was investigated to see if further manipulation of the bandgap energy was possible. The $\text{Sn}_x\text{Ge}_{1-x}$ alloy system also exhibited an interesting phenomenon when grown beyond a critical thickness. That is, Sn segregated

laterally across the surface to produce Sn enriched $\text{Sn}_x\text{Ge}_{1-x}$ dense nanowire arrays ordered along the [001] growth direction. The $\text{Sn}_x\text{Ge}_{1-x}$ alloy system was used as a model system in order to gain insight into the physical origins of phase separation and ordering (*self-assembly*) during dynamic growth. Finally, nanostructures of Sn were fabricated to investigate the effect of quantum confinement on the bandgap of α -Sn. Two types of structures were fabricated and characterized, Sn nanowires and Sn quantum dots.

1.4.1 Bandstructure engineering via alloying

The $\text{Sn}_x\text{Ge}_{1-x}$ binary alloy is an interesting material system due to the potential for monolithic integration of a continuously tunable direct energy gap material with Si(001). Interest in $\text{Sn}_x\text{Ge}_{1-x}$ alloys was incited by a semi-empirical tight-binding calculation¹⁹ that predicted an indirect to direct energy bandgap transition at $x = 0.2$ and a continuously tunable energy bandgap in the infrared from 0.55 eV to 0 eV for Sn compositions $x = 0.2$ to 0.6. The actual measurement of the $\text{Sn}_x\text{Ge}_{1-x}$ energy bandgap as function of Sn composition was not published until 1997, in which the indirect to direct energy bandgap transition was determined to occur near $x = 0.10$ for strain relieved $\text{Sn}_x\text{Ge}_{1-x}$ alloys on Si(001).¹⁵ The ten year lapse between the measurement of the $\text{Sn}_x\text{Ge}_{1-x}$ energy bandgap and the theoretical prediction is attributed to challenges associated with growth of these alloys.

In Chapter 2 of this thesis, the growth of coherently strained $\text{Sn}_x\text{Ge}_{1-x}$ alloys on Ge(001) substrates was demonstrated.²⁰ The challenges associated with growth of $\text{Sn}_x\text{Ge}_{1-x}$ alloys, a low equilibrium solid solubility of Sn in Ge, the tendency for Sn surface segregation, and a large lattice misfit with respect to Si were overcome. Molecular beam epitaxy, a non-equilibrium growth technique, produced metastable alloy compositions exceeding the thermodynamic solid solubility of Sn in Ge. Sn surface segregation was eliminated by low temperature growth. In order to reduce the dislocation density of $\text{Sn}_x\text{Ge}_{1-x}$ films, the substrate was changed from Si to Ge. Coherency to the Ge substrate was determined via high-resolution X-ray diffraction and transmission electron microscopy.

In Chapter 3, the optical properties of coherently strained $\text{Sn}_x\text{Ge}_{1-x}/\text{Ge}(001)$ alloys were investigated both experimentally and theoretically. Speculation in the literature suggested that coherency energy could induce the indirect to direct energy bandgap transition at lower Sn compositions than in strain relieved alloys.²¹ Due to the aforementioned challenges associated with Sn incorporation in the Ge lattice, the occurrence of the indirect to direct energy bandgap transition at lower Sn compositions would be serendipitous. Deformation potential theory calculations were performed to predict the effect of coherency strain on the energy bandgap. The energy bandgap of $\text{Sn}_x\text{Ge}_{1-x}/\text{Ge}(001)$ alloys was measured via Fourier transform infrared

spectroscopy. Both theory and experiment showed that coherency strain had a negligible effect on the energy bandgap. Coherency strain did not change the $\text{Sn}_x\text{Ge}_{1-x}$ energy bandgap when the strain axis was along [001], but deformation potential theory predicted the absence of an indirect to direct energy bandgap transition when the strain axis is oriented along [111].²²

1.4.2 Self assembly via growth instabilities

In Chapter 4, we have studied the $\text{Sn}_x\text{Ge}_{1-x}$ alloy system that undergoes phase separation and forms ordered arrays of Sn enriched $\text{Sn}_x\text{Ge}_{1-x}$ rods oriented along the [001] growth direction. Sn segregates via surface diffusion to the crest of a surface undulation during growth and forms Sn enriched $\text{Sn}_x\text{Ge}_{1-x}$ rods.²³ The $\text{Sn}_x\text{Ge}_{1-x}$ alloy system was used as a model system to study the physical mechanisms governing growth instabilities occurring during molecular beam epitaxy. The experimentally measured period of the growth instability was compared to both a thermodynamic and kinetic model gain insight into the dominant physical mechanisms driving the phase separation. Optical characterization of the energy bandgap was performed via Fourier transform infrared spectroscopy. A decrease in the energy bandgap was observed for phase separated $\text{Sn}_x\text{Ge}_{1-x}$ films in comparison to homogeneous films with the same average Sn composition.

1.4.3 Bandstructure engineering via quantum confinement

Quantum confinement perturbs the energy levels of carriers in a crystal. The perturbation can be understood simply by reviewing the basic quantum mechanical problem - *a particle in a box*. Using the effective mass approximation, an electron, with an effective mass, m_e , and a hole, with an effective mass, m_h , are confined in a one-dimensional infinite potential well. The solution to the time-independent Schrödinger equation yields discrete energy levels and the energy is inversely proportional to the square of the width of the well. Thus, the ground state energy increases as the width of the well decreases. Using this analysis, the energy of the electrons in the conduction band (E_c) and the holes in the valence band (E_v) are:

$$E_c = \frac{E_g}{2} + \frac{\hbar^2 k^2}{2m_e} + \frac{\hbar^2 \pi^2}{2m_e a^2} \quad (1)$$

$$E_v = -\frac{E_g}{2} + \frac{\hbar^2 k^2}{2m_h} - \frac{\hbar^2 \pi^2}{2m_h a^2} \quad (2)$$

where E_g is the bandgap energy, $\hbar k$ is the crystal momentum, and a is the width of the potential well. Equations (1) and (2) are combined to obtain the bandgap energy:

$$E_g^{confined} = E_g + \frac{\hbar^2 \pi^2}{2a^2} \left(\frac{1}{m_e} + \frac{1}{m_h} \right) \quad (3)$$

The bandgap energy due to quantum confinement increases with respect to the unconfined or bulk bandgap energy.

Using more sophisticated theoretical approaches, the variation of the bandgap energy with quantum dot size is plotted in Figure 1.1 for Ge and Si.²⁴⁻²⁷ For Ge, quantum confinement effects are expected to open the bandgap when the radius is on the order of 10 nm and for Si, quantum confinement effects are expected for radii on the order of 5 nm. A semi-empirical tight-binding calculation was performed for diamond cubic (α) Sn quantum wires and quantum confinement effects are expected for relatively large radii, 40 nm due to a much smaller electron effective mass versus Si and Ge.²⁸

In Chapter 5, the fabrication and optical characterization of Sn nanostructures is discussed. Two different nanostructures were studied, Sn nanowires and Sn quantum dots. Sn nanowires were fabricated by pressure injection of molten Sn into hexagonally ordered alumina two-dimensional templates. The fabrication of ordered alumina templates is an example of directed self-assembly. The templates are fabricated non-lithographically using an electrochemical etching process. The second type of nanostructures fabricated were α -Sn quantum dots. By annealing 1 μm thick $\text{Sn}_x\text{Ge}_{1-x}$ alloy films at temper-

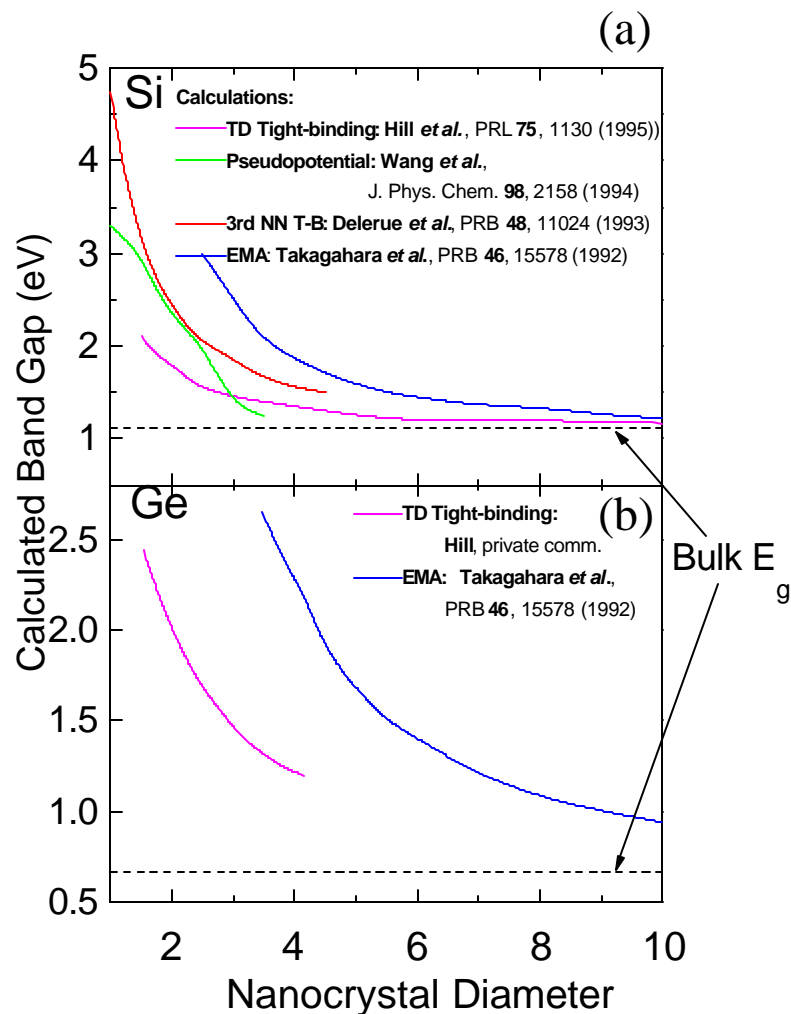


Figure 1.1: Theoretical prediction of bandgap energy versus nanocrystal diameter for (a) Si and (b) Ge.

atures exceeding 550 °C, Sn phase separates and forms quantum dots embedded in a Ge matrix. The Ge matrix stabilizes the α phase of Sn. Optical characterization of 32 nm α -Sn quantum dots demonstrated a widening of the bandgap due to quantum confinement effects.

1.5 Bibliography

1. E. A. Fitzgerald and L. C. Kimmerling, *Mat. Res. Soc. Bull.* **23**, 39 (1998)
2. J. K. N. Mbindyo, B. D. Reiss, B. R. Martin, C. D. Keating, M. J. Natan, and T. E. Mallouk, *Adv. Mat.* **13**, 249 (2001)
3. C. D. Bain and G. M. Whitesides, *Angew. Chem.* **101**, 522 (1989)
4. A. Ulman, *Introduction to Thin Organic Films: From Langmuir-Blodgett to Self-Assembly* (Academic Press, Boston, 1991).
5. T. I. Kamins, R. S. Williams, and D. P. Basile, *Nanotechnology* **10**, 117 (1999)
6. F. Liu, A. H. Li, and M. G. Lagally, *Phys. Rev. Lett.* **87**, 6103 (2001)
7. H. Sunamura, N. Usami, Y. Shiraki, and S. Fukatsu, *Appl. Phys. Lett.* **68**, 1847 (1996)
8. J. Viernow, D. Y. Petrovykh, F. K. Men, A. Kirakosian, J.-L. Lin, and F. J. Himpsel, *Appl. Phys. Lett.* **74**, 2125 (1999)
9. Y. Chen, D. A. A. Ohlberg, G. Medeiros-Ribeiro, Y. Chang, and R. S. Williams, *Appl. Phys. Lett.* **76**, 4004 (2000)
10. R. D. Twisten, D. M. Follstaedt, S. R. Lee, E. D. Jones, J. L. Reno, J. Mirecki Millunchick, A. G. Norman, S. P. Ahrenkiel, and M. A., *Phys. Rev. B* **60**, 13619 (1991)
11. A. G. Norman, J. M. Olson, J. F. Geisz, H. R. Moutinho, A. Mason, and M. M. Al-Jassim, *Appl. Phys. Lett.* **74**, 1382 (1999)

12. A. G. Norman, S. P. Ahrenkiel, H. Moutinho, M. M. Al-Jassim, A. Mascarenhas, J. M. Millunchick, S. R. Lee, R. D. Twesten, D. M. Follstaedt, J. Reno, and E. D. Jones, *Appl. Phys. Lett.* **73**, 1844 (1998)
13. W. Wong, T. Sands, N. Cheung, M. Kneissl, D. Bour, P. Mei, L. Romano, and N. Johnson, *Appl. Phys. Lett.* **75**, 1360 (1999)
14. S. Cristoloveanu, *Solid State Electron.* **45**, 1403 (2001)
15. G. He and H. A. Atwater, *Phys. Rev. Lett.* **79**, 1937 (1997)
16. L. E. Brus, P. F. Szajowki, W. L. Wilson, T. D. Harris, S. Schuppler, and P. H. Citrin, *J. Am. Chem. Soc.* **117**, 2915 (1995)
17. R. T. Collins, P. M. Fauchet, and M. A. Tischler, *Physics Today* **50**, 24 (1997)
18. J. W. G. Wildoer, L. C. Venema, A. G. Rinzler, R. E. Smalley, and C. Dekker, *Nature* **391**, 59 (1998)
19. D. W. Jenkins and J. D. Dow, *Phys. Rev. B* **36**, 7994 (1987)
20. R. Ragan and H. A. Atwater, *Appl. Phys. Lett.* **77**, 3418 (2000)
21. R. A. Soref and L. Friedman, *Superlattices Microstruct.* **14**, 189 (1993)
22. R. Ragan, K. S. Min, and H. A. Atwater, *Mat. Sci. Eng. B* **87**, 204 (2001)
23. R. Ragan, C. C. Ahn, and H. A. Atwater, manuscript in prep. (2001)
24. N. A. Hill and K. B. Whaley, *Phys. Rev. Lett.* **75**, 1130 (1995)
25. L. W. Wang and A. Zunger, *J. Phys. Chem* **98**, 2158 (1994)
26. C. Delerue, G. Allan, and M. Lannoo, *Phys. Rev. B* **48**, 11024 (1993)
27. T. Takagahara and K. Takeda, *Phys. Rev. B* **46**, 15578 (1992)
28. V. Sih, in *Applied Physics* (Caltech, Pasadena, 2000).

Chapter 2 Growth of Coherent, Homogeneous Sn_xGe_{1-x}/Ge(001) Epitaxial Films

2.1 Introduction

Over the last 10 years, there has been considerable interest by many groups in the growth of Sn_xGe_{1-x} alloys with Sn compositions in excess of 20% in order to obtain the first group IV direct energy bandgap alloy.¹⁻⁴ High Sn composition Sn_xGe_{1-x} alloys proved to be challenging to grow due to the limited equilibrium solid solubility, $x < 0.01$, for both Sn in Ge and Ge in Sn as shown in the phase diagram in Figure 2.1.^{5,6} and the tendency for Sn surface segregation during growth due to a lower surface free energy of Sn versus Ge.⁷ A non-equilibrium growth technique such as molecular beam epitaxy was employed to produce metastable Sn_xGe_{1-x} alloys with $x > 0.01$. In order to eliminate Sn surface segregation, low growth temperatures ($T < 180$ °C)^{1,8} were necessary to inhibit diffusion of Sn from the near surface bulk to the surface.

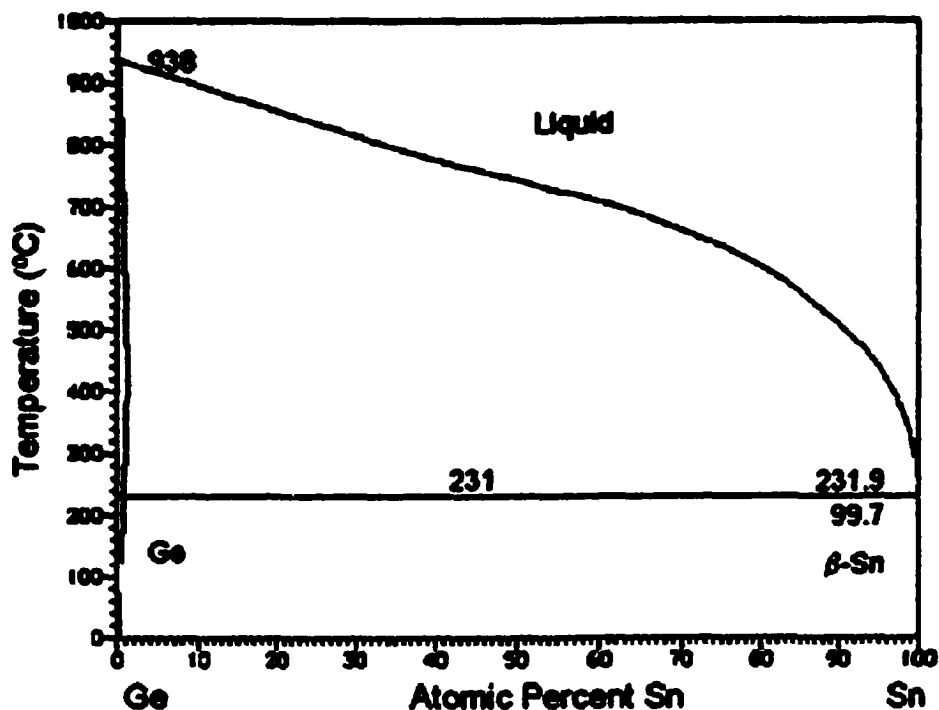


Figure 2.1: Binary phase diagram for Sn in Ge. [Massalski, et al 1990] The alloy forms a simple eutectic system with eutectic temperature of 231.9 °C.

It is well known that during low temperature epitaxy the film thickness in which epitaxial single crystals are obtained during film growth decreases as the growth temperature decreases due to surface kinetic roughening.^{9,10} Epitaxial growth of coherent $\text{Sn}_x\text{Ge}_{1-x}$ on Ge(001) at a substrate temperature of 100 °C was possible up to 3.5 nm for $x = 0.26$.^{1,7} Beyond 3.5 nm the $\text{Sn}_x\text{Ge}_{1-x}$ films transformed from crystalline to highly defective and then became amorphous as the growth progressed. The film thickness at which the crystalline to amorphous phase transition occurred has an exponential dependence on the growth temperature,¹⁰ and hence, small increases in the growth temperature can greatly increase this thickness. Ar^+ ion beam assisted deposition allows the

incorporation of Sn in the Ge lattice with Sn compositions up to $x = 0.34$ and a film thickness of 20 nm at higher substrate temperatures, $T = 140 - 160$ °C.¹¹ A drawback to ion beam assisted deposition is the incorporation of ion-induced defects and interstitial Ar atoms in the lattice that may hinder optoelectronic device performance.

The driving force for Sn surface segregation increases with Sn composition at a fixed temperature.⁴ Therefore, another approach to obtaining thick, single crystal, epitaxial $\text{Sn}_x\text{Ge}_{1-x}$ films is growth of Sn dilute alloys at relatively high temperatures, $T = 160 - 180$ °C. He and Atwater¹² were able to grow epitaxial $\text{Sn}_x\text{Ge}_{1-x}$ films with thickness up to 300 nm for $0 < x < 0.15$ at a higher substrate temperature, 180 °C. Infrared absorption of these homogeneous, strain-relieved $\text{Sn}_x\text{Ge}_{1-x}$ epitaxial films grown on Si(001) demonstrated that the indirect to direct energy gap transition occurs near $x = 0.09$,¹² yielding the first known example of a direct energy gap group IV semiconductor alloy. The occurrence of the indirect to direct energy bandgap transition at lower Sn composition is serendipitous due to the previously described difficulties associated with incorporation of Sn beyond $x = 0.15$.

Using the virtual crystal approximation, the lattice misfit for the $\text{Sn}_{0.1}\text{Ge}_{0.9}$ alloy on Si(001) is 5.7%, which is a larger misfit than Ge on Si(001), 4.2%. The maximum thickness of a coherently strained epitaxial film, that is, before strain-relieving dislocations form to reduce the coherency energy, has an inverse dependence on the misfit.¹³ The presence of strain-relieving dislocations

severely degrades optoelectronic device performance since dislocations serve as non-radiative recombination sites, reducing quantum efficiency. In order for $\text{Sn}_x\text{Ge}_{1-x}$ to be a viable material as an infrared detector or emitter, it is necessary to reduce the dislocation density or eliminate dislocations in the epitaxial films. By changing the substrate from Si(001) to Ge(001), the misfit for $\text{Sn}_{0.1}\text{Ge}_{0.9}$ is reduced from 5.7% to 1.5%.

In this chapter, the critical thickness for coherent epitaxial growth of $\text{Sn}_x\text{Ge}_{1-x}$ on Ge(001) was explored both experimentally and theoretically. The first series of films grown were coherent $\text{Sn}_x\text{Ge}_{1-x}/\text{Ge}$ superlattices with $0.01 < x < 0.05$ and thickness up to 250 nm. The second group of films grown was single layer epitaxial films with $0.02 < x < 0.115$ and film thickness of 50 - 300 nm. A thermodynamic model predicting the critical thickness was compared with the experimental results. Experimentally, $\text{Sn}_x\text{Ge}_{1-x}$ films were grown beyond the predicted thermodynamic critical thickness. Growth of metastable, coherent epitaxial films was consistent with previous reports from other strained semiconductor alloys, such as the $\text{Si}_{1-x}\text{Ge}_x$ system.¹⁴

2.2 Molecular beam epitaxy of $\text{Sn}_x\text{Ge}_{1-x}$ alloys

The $\text{Sn}_x\text{Ge}_{1-x}$ films were grown by molecular beam epitaxy (MBE) on Ge(001) substrates with a resistivity of 30 Ω cm and miscut of $\pm 1.0^\circ$. The system was pumped with a cryopump to achieve base pressures of 10^{-10} Torr. The base pressure arose from the presence of residual H_2O , CO_2 and O_2 . High purity

(99.9999%) solid sources of Sn and Ge were used with a Knudsen effusion cell for Sn evaporation and electron beam evaporation of Ge. The substrate was clamped to a molybdenum block that was radiatively heated and a thermocouple was attached to the assembly to monitor the substrate temperature. The measured substrate temperature was accurate to within ± 10 °C. The deposition rate at the substrate was controlled with a quartz crystal thickness monitor that was calibrated post-growth with Rutherford backscattering spectroscopy film thickness and compositional analysis.

The Ge(001) surface preparation¹⁵ consisted of a wet chemical process that included a solvent degrease (acetone, methanol and 18 M Ω water), each step for 2 minutes, followed by H₂O₂ oxidation (5% H₂O₂/H₂O) for 2 minutes, H₂O rinse for 1 minute, and a HF acid dip (5% HF/H₂O) for 20 seconds. The HF removed the oxide layer and provided a hydrogen-terminated surface. Prior to growth, the Ge(001) substrate was baked for 1.5 hours at 200 °C in ultra high vacuum in order to desorb any residual hydrocarbon contamination. The temperature was then ramped to 550 °C to desorb the passivating hydrogen layer at the surface, thus, obtaining a 2 \times 1 surface reconstruction. Despite the surface preparation technique, through secondary ion mass spectroscopy analysis, residual carbon and oxygen contamination at the Ge substrate/Ge buffer layer interface was detected, up to 5×10^{18} cm⁻². A 100 - 200 nm Ge buffer layer was grown to smooth the Ge surface that roughened during the chemical cleaning process and to bury the hydrocarbon contamination. The surface reconstruction and crystal

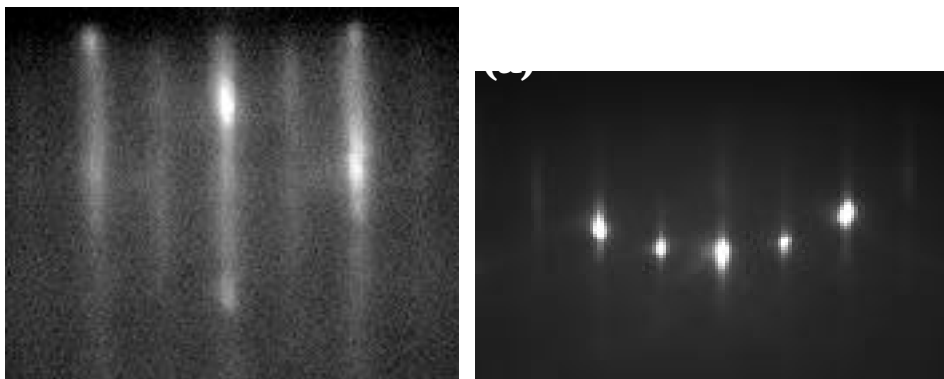


Figure 2.2: RHEED diffraction patterns along [110] zone axis (a) before growth of Ge buffer layer and (b) after growth of Ge buffer layer.

quality were probed *in situ* with reflection high energy electron diffraction (RHEED) at 17 keV along the [110] zone axis. Typical RHEED patterns before and after growth of the Ge buffer layer are shown in Figure 2.2(a) and Figure 2.2(b), respectively. Before buffer layer growth, the fundamental diffraction rods were modulated in intensity along their length and the half order diffraction rods have slightly lower intensity, indicative of a slightly rough surface. After the buffer layer was grown, the RHEED pattern consisted of sharp 2×1 diffraction rods superimposed with the Ewald sphere and the half order and fundamental diffraction rods were equi-intense (Figure 2.2b). This type of RHEED pattern is characteristic of a flat surface.

The substrate was then cooled to 160 °C prior to $\text{Sn}_x\text{Ge}_{1-x}$ growth in order to inhibit Sn surface segregation. During the cool down period that took approximately 20 minutes, the sample was subject to ultra high vacuum. Growth of the

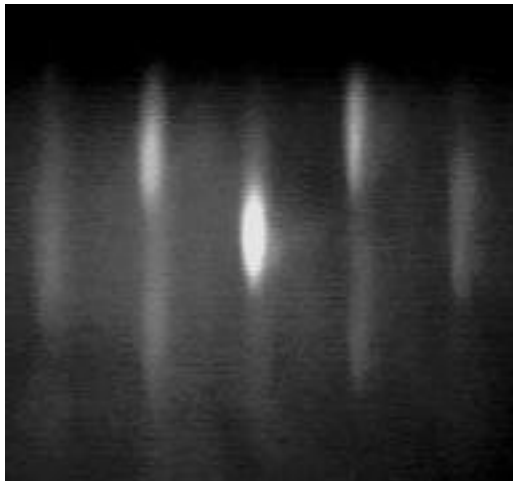


Figure 2.3: RHEED pattern of 35 nm $\text{Sn}_x\text{Ge}_{1-x}$ epitaxial film with $x = 0.02$. The Bragg rods are modulated along their length.

$\text{Sn}_x\text{Ge}_{1-x}$ film began immediately after the substrate reached the target growth temperature, 160 °C, to minimize surface contamination with the hydrocarbons present in the base pressure. The growth rate of Ge was controlled by feedback from the quartz crystal monitor to the power supply and held at 0.05 nm/sec. The Sn effusion cell was calibrated and controlled with temperature to obtain the target Sn composition in the alloy. During deposition, surface kinetic roughening due to the low growth temperature was evident in the RHEED patterns. The intensity of the fundamental diffraction rods became modulated along their length as the temperature was lowered below $T = 200$ °C. When the Sn deposition began, the half order diffraction rod intensity decreased as the surface evolved into a 1×1 surface. This film thickness was 35 nm for $x = 0.02$ (Figure 2.3). The final RHEED pattern was indicative of a decrease in the average

terrace length, increasing step density, and stochastic surface roughening.¹⁰ Despite surface roughening, single crystal $\text{Sn}_x\text{Ge}_{1-x}$ epitaxial films were obtained.

2.3 $\text{Sn}_x\text{Ge}_{1-x}/\text{Ge}/\text{Ge}(001)$ superlattices

A series of $\text{Sn}_x\text{Ge}_{1-x}/\text{Ge}$ superlattice films were grown with $0.01 < x < 0.05$ and thickness up to 70 nm (Table 2.1). The $\text{Sn}_x\text{Ge}_{1-x}$ epitaxial films were characterized post-growth with Rutherford backscattering spectroscopy (RBS), high resolution X-ray diffraction (HR-XRD) and transmission electron microscopy (TEM). Due to the large Rutherford cross-section (large atomic size) of Sn, RBS is a sensitive technique to measure the Sn composition in the superlattice layers and to probe the sample to determine if Sn surface segregation occurred. A typical RBS spectrum using 2 MeV He^{++} with the sample tilted 7° to the beam normal is shown in Figure 2.4 for a 5 period $\text{Sn}_{0.02}\text{Ge}_{0.98}$ superlattice. The period of the superlattice was 70 nm and each period was composed of a 15 nm¹ $\text{Sn}_x\text{Ge}_{1-x}$ layer and a 55 nm Ge layer. The top three $\text{Sn}_x\text{Ge}_{1-x}$ layers of the superlattice were distinguishable. Beyond the third layer of the superlattice, the Sn peaks were superimposed in the Ge signal and not resolvable. The Ge and Sn leading edge energies were represented as lines in Figure 2.4. The leading edge energy corresponds to the maximum energy of a recoiled He^{++} ion after colliding

¹ Note that in the table the target $\text{Sn}_x\text{Ge}_{1-x}$ layer thickness was 14 nm. The error in measuring the thickness of the film during growth is approximately 10%.

with an atom. This maximum energy increases as the atomic mass of the scatterer increases, thereby yielding compositional analysis. As the He^{++} ion penetrates the sample, it loses energy. The thickness of a layer, if the energy spread is greater than the resolution of the electronics, can be determined from the width of the peak in the RBS spectrum. In Figure 2.4, the $\text{Sn}_x\text{Ge}_{1-x}$ layers were too thin to resolve the thickness. Yet, the uniform peak height with energy in these three layers (shown in the inset to Figure 2.4) indicated the absence of Sn surface segregation. Sn segregation would be associated with an enhanced peak at the Sn leading edge energy, that is, at the surface.

The relaxed or equilibrium lattice parameter ($a_{\text{SnGe}}^{\text{eq}}$) of the $\text{Sn}_x\text{Ge}_{1-x}$ alloy was calculated as a function of composition using the virtual crystal approximation. The virtual crystal approximation has been shown to hold experimentally for the lattice parameter of the $\text{Sn}_x\text{Ge}_{1-x}$ alloy system.¹² The bulk lattice constants of α -Sn and Ge are 0.6489 nm and 0.5658 nm, respectively; hence, by alloying Sn and Ge, the equilibrium lattice constant of the resulting film is larger than Ge. In order to obtain coherent registry between the epitaxial film and the Ge(001) substrate, the lattice parameter in the plane of the films ($a_{\text{SnGe}}^{\parallel}$) is in compression. The out of plane lattice parameter (a_{SnGe}^{\perp}) is free to expand due to the free surface. The in plane compression and out of plane expansion of the lattice constant is referred to as a tetragonal distortion depicted

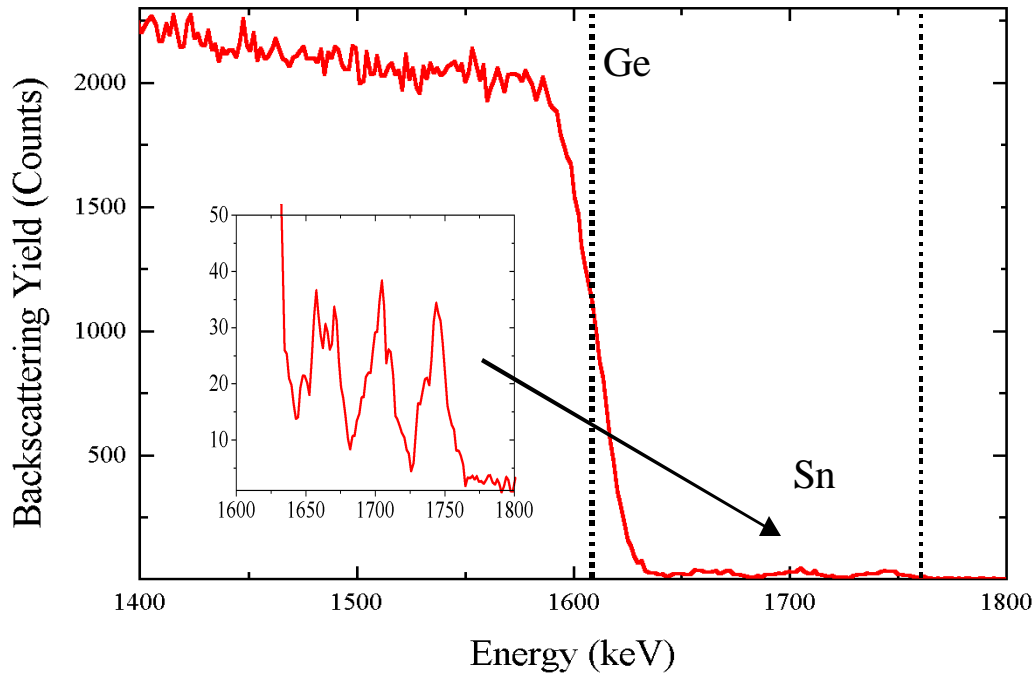


Figure 2.4: Rutherford backscattering spectrum of $\text{Sn}_{0.02}\text{Ge}_{0.98}$ superlattice with 15 nm $\text{Sn}_x\text{Ge}_{1-x}$ layers and a period thickness of 70 nm. The Ge and Sn leading edge energies are represented by lines.

in Figure 2.5. The expansion along the [001] direction is a function of the Poisson ratio(ν), 0.273 for Ge and 0.298 for Sn. The Poisson ratio is also linearly interpolated for the alloy. Thus, for a coherently-strained $\text{Sn}_x\text{Ge}_{1-x}$ film, the out of plane lattice constant, along the [001] direction, will be larger than the $\text{Sn}_x\text{Ge}_{1-x}$ equilibrium lattice constant.

Superlattice Periods	Description of Period	Sn composition	Superlattice Periods	Description of Period	Sn composition
5	20 nm $\text{Sn}_x\text{Ge}_{1-x}$ 50 nm Ge	0.02	1	23 nm $\text{Sn}_x\text{Ge}_{1-x}$	0.03
3	20 nm $\text{Sn}_x\text{Ge}_{1-x}$ 50 nm Ge	0.03	7	10 nm $\text{Sn}_x\text{Ge}_{1-x}$ 47.5 nm Ge	0.02
4	20 nm $\text{Sn}_x\text{Ge}_{1-x}$ 50 nm Ge	0.01	14	50 nm $\text{Sn}_x\text{Ge}_{1-x}$ 21.5 nm Ge	0.02
1	50 nm $\text{Sn}_x\text{Ge}_{1-x}$	0.02	5	14 nm $\text{Sn}_x\text{Ge}_{1-x}$ 50 nm Ge	0.02
1	70 nm $\text{Sn}_x\text{Ge}_{1-x}$	0.02	1	23 nm $\text{Sn}_x\text{Ge}_{1-x}$	0.04
2	35 nm $\text{Sn}_x\text{Ge}_{1-x}$ 50 nm Ge	0.02	1	23 nm $\text{Sn}_x\text{Ge}_{1-x}$	0.05

Table 2.1: Description of $\text{Sn}_x\text{Ge}_{1-x}/\text{Ge}$ superlattice films on Ge(001). All superlattice structures have an approximately 200 nm Ge buffer layer and a 200 nm Ge capping layer.

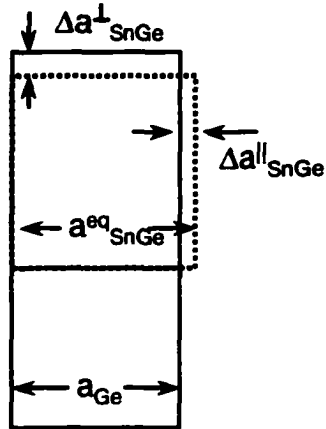


Figure 2.5: Schematic of tetragonal distortion of $\text{Sn}_x\text{Ge}_{1-x}$ unit cell on Ge(001).

High resolution X-ray diffraction (HR-XRD) was employed to measure the tetragonal distortion of the unit cell. As seen from the Bragg diffraction equation (4), if the d_{004} spacing increases, the value of θ should decrease.

$$\frac{\Delta d}{d} = -\cot(\theta)\Delta\theta \quad (4)$$

The experimental results of a ω - 2θ scan around the Ge (004) Bragg reflection are shown in Figure 2.6 for the $\text{Sn}_{0.02}\text{Ge}_{0.98}$ alloy film. The $\text{Sn}_{0.02}\text{Ge}_{0.98}$ alloy peak shifted to smaller values of θ with respect to the Ge peak as expected for this strained film. Comparison of the HR-XRD experimental spectrum with a dynamical simulation generated using the Takagi-Taupin equations¹⁶ confirmed the Sn composition, $x = 0.02$, that was measured in RBS and indicated the absence of strain relaxation at the $\text{Sn}_x\text{Ge}_{1-x}/\text{Ge}$ interface. HR-XRD is also a sensi-

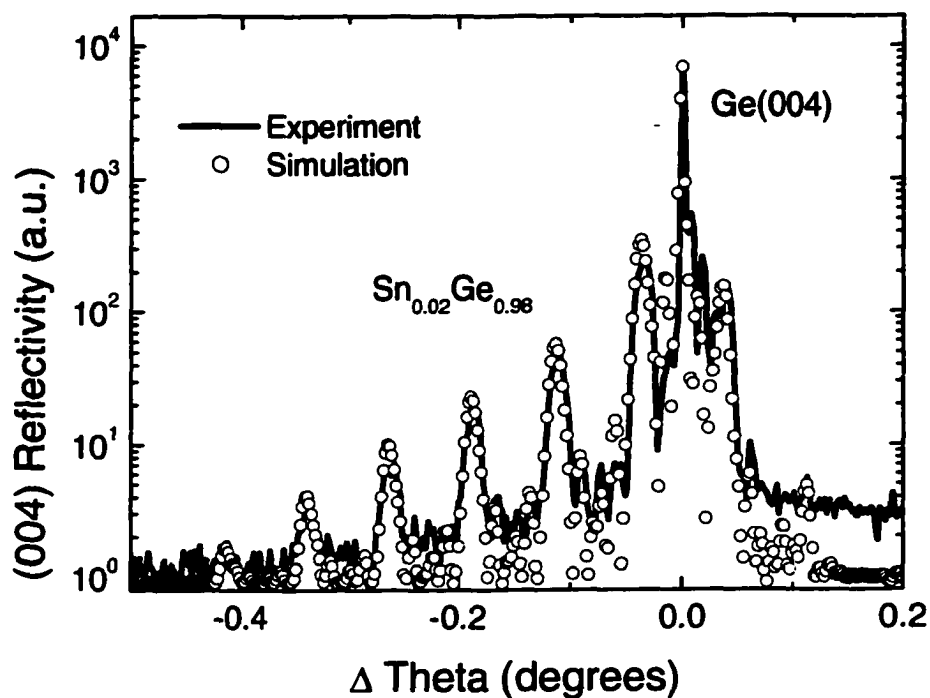


Figure 2.6: HR-XRD ω - 2θ scan around Ge (004) Bragg reflection for the experiment (solid curve) and the simulation (open circles). The $\text{Sn}_{0.02}\text{Ge}_{0.98}$ peak is shifted to smaller values of θ .

tive measurement of the periodicity of the superlattice and the layer thickness. In Figure 2.6, the finite thickness interference fringes indicated the $\text{Sn}_{0.02}\text{Ge}_{0.98}$ film was coherent to the Ge(001) substrate and yielded a value of 15 nm for the $\text{Sn}_x\text{Ge}_{1-x}$ layer thickness and 70 nm for the period thickness. Similar analysis was performed for the $\text{Sn}_x\text{Ge}_{1-x}$ films listed in Table 2.1 to determine coherency to the Ge(001) substrate.

Cross-sectional TEM analysis at 300 keV was also performed on the $\text{Sn}_{0.02}\text{Ge}_{0.98}$ alloy film. Imaging under $\bar{g} = [004]$ 2 beam conditions in bright field,

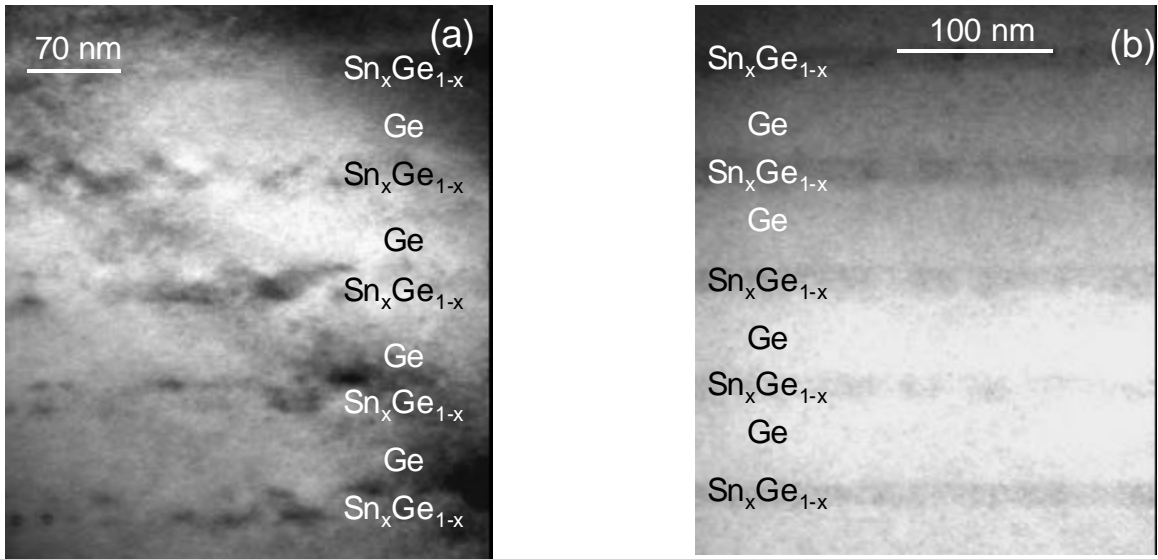


Figure 2.7: TEM of analysis of a 5 period $\text{Sn}_{0.02}\text{Ge}_{0.98}/\text{Ge}$ superlattice. Imaged with (a) 2 beam conditions with $\vec{g} = [004]$ where strain contrast is visible and (b) down the $[110]$ zone axis where the $\text{Sn}_{0.02}\text{Ge}_{0.98}$ films appear uniform in composition.

defects were absent in the image as illustrated in Figure 2.7(a). 2 beam conditions are accomplished by tilting the sample such that the Bragg condition is satisfied for one particular set of diffraction planes and only the corresponding diffracted beam and the transmitted beam contribute to the image. More specifically, the other diffraction planes are only weakly excited and the contrast associated with these beams is negligible in a 2 beam image. When the substrate normal is along $[001]$, the diffracted intensity from the (004) planes, seen in Figure 2.7(a), is sensitive to strain related with threading dislocations. For the diamond cubic lattice, threading dislocations that are associated with film relaxation have burgers vectors of the type $\frac{1}{2} [011]$. Strain contrast, indicative of

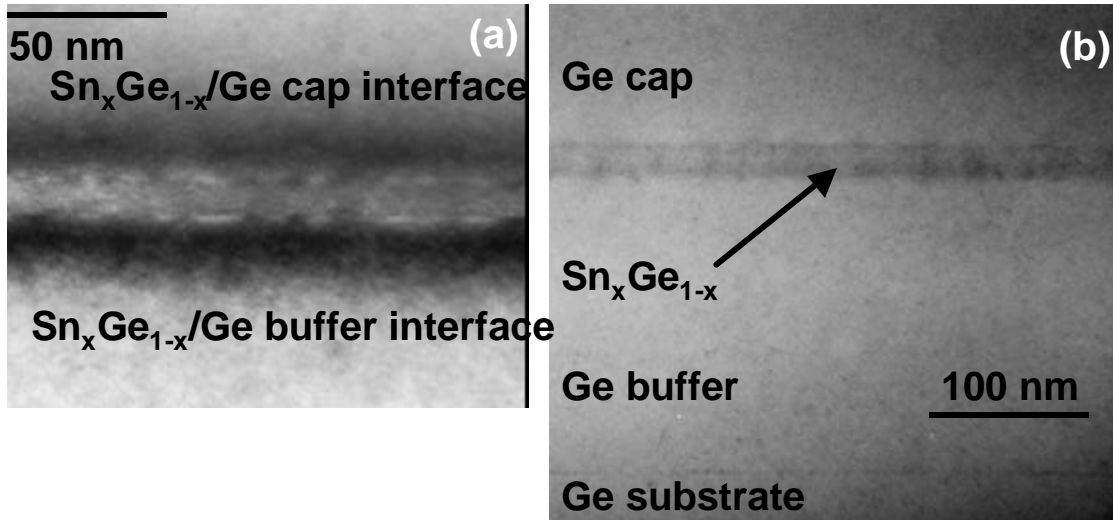


Figure 2.8: Cross-sectional TEM analysis of $\text{Sn}_{0.03}\text{Ge}_{0.97}$ with $t = 23$ nm. Imaged (a) with $\bar{g} = [004]$ 2 beam conditions where strain contrast is observed at the interfaces and (b) down the $[110]$ zone axis indicating uniform Sn composition in the layer.

coherency strain, was evident as non-uniform dark patches at the two $\text{Sn}_x\text{Ge}_{1-x}/\text{Ge}$ interfaces in the $\bar{g} = [004]$ 2 beam image of Figure 2.7(a) but not threading dislocations. Imaging down the $[110]$ zone axis as shown in Figure 2.7(b), the strain contrast was not as prominent and the $\text{Sn}_{0.02}\text{Ge}_{0.98}$ layers in the superlattice appeared uniform in composition. Further TEM analysis was performed on a single layer $\text{Sn}_x\text{Ge}_{1-x}$ film with $x = 0.03$ and $t = 23$ nm with a Ge capping layer. Similarly in the $\bar{g} = [004]$ 2 beam image for this sample, shown in Figure 2.8(a), strain contrast was observable at the $\text{Sn}_x\text{Ge}_{1-x}/\text{Ge}$ interface but not threading dislocations. The film composition was uniform and the interface abrupt when imaging down the $[110]$ zone axis as shown in Figure 2.8(b). High

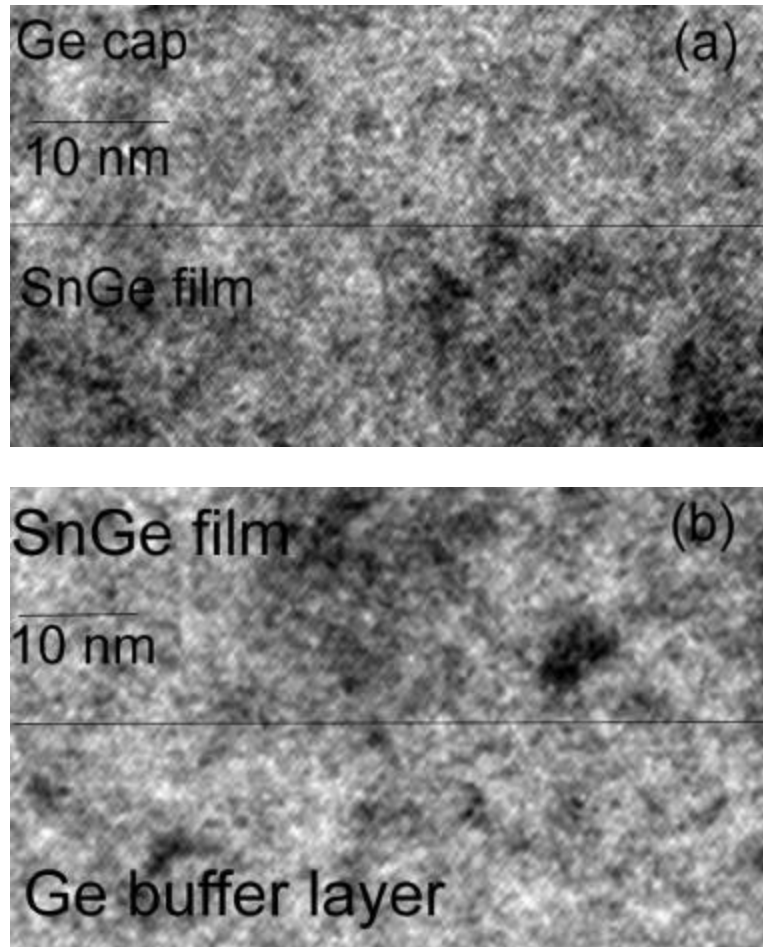


Figure 2.9: HR-TEM image down $[110]$ zone axis of $\text{Sn}_{0.03}\text{Ge}_{0.97}$ (a) at the $\text{Sn}_{0.03}\text{Ge}_{0.97}/\text{Ge}$ cap layer interface and (b) at the $\text{Sn}_{0.03}\text{Ge}_{0.97}/\text{Ge}$ buffer layer interface. The lattice fringes are continuous across both interfaces. The line is drawn to indicate the interface.

resolution images of the interfaces are seen in Figure 2.9. The lattice fringes are continuous at the $\text{Sn}_x\text{Ge}_{1-x}/\text{Ge}$ substrate interface as well as at the $\text{Sn}_x\text{Ge}_{1-x}/\text{Ge}$ capping layer interface. Therefore, the $\text{Sn}_x\text{Ge}_{1-x}$ film is coherent to the Ge substrate.

2.4 $\text{Sn}_x\text{Ge}_{1-x}/\text{Ge}_{1-x}(001)$ epitaxial films

2.4.1 Growth conditions

The second group of films grown were single layer $\text{Sn}_x\text{Ge}_{1-x}$ films on Ge(001) substrates. The growth routine was modified slightly from the method used to grow the superlattice structures (Section 2.2). That is, the substrate temperature was lowered to the $\text{Sn}_x\text{Ge}_{1-x}$ alloy growth temperature of $T = 140 - 160$ °C during Ge buffer layer growth to further minimize surface contamination. As mentioned earlier, Sn surface segregation becomes more problematic at higher Sn compositions, thus the growth temperature was lowered when higher Sn composition alloys were grown. $\text{Sn}_x\text{Ge}_{1-x}$ alloys with $x < 0.06$ were grown at 160 °C and alloys with $0.07 < x < 0.115$ were grown at 150 °C, and the alloy with $x = 0.115$ was grown at 140 °C. The growth rate was lowered to compensate for the lower growth temperature; for samples with $x < 0.06$, $R_G = 0.05$ nm/sec; for $0.07 < x < 0.115$, $R_G = 0.04$ nm/sec; and for $x = 0.115$, $R_G = 0.03$ nm/sec.

2.4.2 *In situ* crystal structure analysis

During MBE growth, the crystal structure was monitored with RHEED. As growth progressed, the RHEED pattern transformed into a bulk crystal dif-

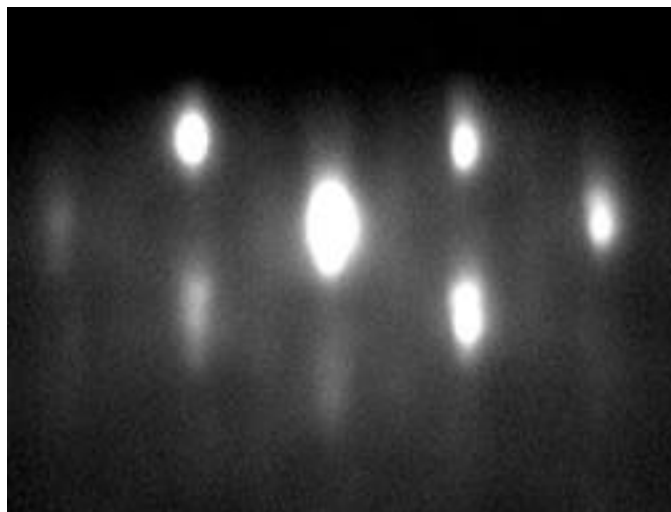


Figure 2.10: RHEED pattern of $\text{Sn}_x\text{Ge}_{1-x}$ alloy on Ge(001) with $t = 16$ nm and $x = 0.06$. The diffraction rods have transformed into spots that is indicative of 3-dimensional growth.

fraction pattern. This transformation was associated with two-dimensional layer by layer growth to three-dimensional growth. The film thickness at which the surface morphology transition from two-dimensional to three-dimensional occurred was dependent on the Sn composition. For example, this film thickness was 16 nm for $x = 0.06$ as indicated by the RHEED pattern in Figure 2.10. Streaking of diffraction spots as well as additional spots seen as satellites around $\{111\}$ were also evident for approximately 30% of the grown films. Streaking of diffraction spots was indicative of surface faceting and the satellite diffraction spots around $\{111\}$ were attributed to $\{111\}$ stacking faults.¹ In summary, the RHEED patterns indicated that the $\text{Sn}_x\text{Ge}_{1-x}$ films were epitaxial and single crystalline with atomically rough surfaces.

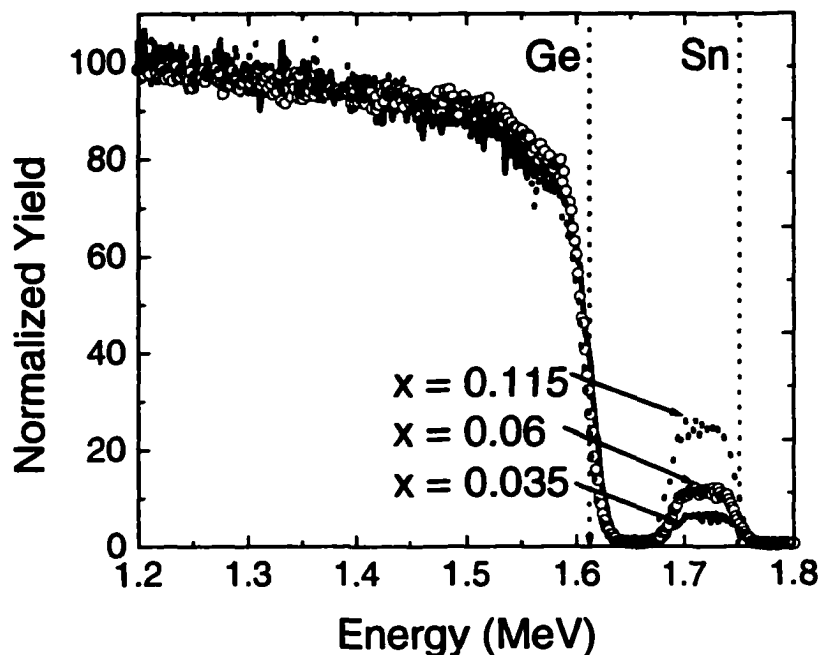


Figure 2.11: RBS spectra of $\text{Sn}_x\text{Ge}_{1-x}/\text{Ge}(001)$ for $x = 0.035, 0.06,$ and 0.115 and $t = 100$ nm. The Sn peaks are uniform in height and thus composition with depth. The leading edge of Sn and Ge are represented as dashed lines.

2.4.3 Post-growth film characterization

The crystal quality and composition were further analyzed with atomic force microscopy (AFM), RBS, HR-XRD, and TEM. AFM images of $500 \text{ nm} \times 500 \text{ nm}$ regions on 100 nm thick $\text{Sn}_x\text{Ge}_{1-x}$ films confirmed the rough surface observed in the RHEED patterns. The root-mean-square roughness was measured as 1.1 nm for samples with $x < 0.06$ and 1.5 nm for $x > 0.06$. In Figure 2.11, representative backscattering spectra taken with 2 MeV He^{++} and the sample tilted 7 degrees to the beam normal are shown for 100 nm thick $\text{Sn}_x\text{Ge}_{1-x}$ alloy films with $x = 0.035, 0.06$ and 0.115 . The constant height of the Sn backscattered peak demonstrated that the films were uniform in composition

with depth and free of Sn surface segregation. The Sn composition varied laterally over a $2\text{ cm} \times 2\text{ cm}$ region on the sample surface by $\pm 5\%$ due to a variation of the Sn flux across the wafer resulting from the fixed position of the Sn effusion cell with respect to the substrate.

A representative HR-XRD ω - 2θ scan around the Ge (004) reflection is shown in Figure 2.12(a) for $x = 0.035, 0.06, \text{ and } 0.115$. Since the unit cell undergoes tetragonal distortion (depicted in Figure 2.5), the lattice constant along the growth direction [001] is larger, giving rise to a negative shift of the (004) Bragg reflection with respect to the Ge (004) Bragg reflection; see equation (4). The $\text{Sn}_x\text{Ge}_{1-x}$ peak shift was in agreement with the expected shift for a coherently strained alloy with the Sn composition measured in RBS. The broadening of the $\text{Sn}_{0.115}\text{Ge}_{0.885}$ peak in Figure 2.12(a) was attributed to diffuse reflection resulting from the rougher surface observed in both RHEED and AFM. The experimental HR-XRD results for the $\text{Sn}_x\text{Ge}_{1-x}$ alloy films were then compared with a dynamical simulation for coherently strained films with $0.035 < x < 0.12$ on Ge(001). Upon comparison with the experimental data, the dynamical simulation¹⁶ confirmed the backscattering composition and the absence of strain relaxation at the $\text{Sn}_x\text{Ge}_{1-x}/\text{Ge}$ interface. The simulation (open circles) and experimental (solid curve) HR-XRD results are shown for $x = 0.06$ in Figure 2.12(b). The finite thickness interference fringes yielded a value of 99 nm for the $\text{Sn}_{0.06}\text{Ge}_{0.94}$ film thickness. The angular displacement ($\Delta\theta_{\text{Ge}}^{004}$) of the

$\text{Sn}_x\text{Ge}_{1-x}$ (004) reflection from the Ge(004) reflection (θ_{Ge}^{004}) experimentally determined the strain along the growth direction, e_{zz} (where d is the interplanar spacing of the reflection):

$$e_{zz}^{\text{exp}} = (e_{\text{xray}}^{(004)} + 1) \frac{d_{\text{Ge}}^{004}}{d_{\text{SnGe}}^{\text{eq}}} - 1 = \left(\frac{\sin \theta_{\text{Ge}}^{004}}{\sin(\theta_{\text{Ge}}^{004} + \Delta\theta^{004})} \right) \frac{d_{\text{Ge}}^{004}}{d_{\text{SnGe}}^{\text{eq}}} - 1 \quad (5)$$

The angular displacement of the $\text{Sn}_x\text{Ge}_{1-x}$ (224) asymmetric reflection with respect to the Ge (224) reflection is a function of both e_{zz} (strain along the growth direction) and e_{xx} (strain in the plane of the film). Since e_{zz} is known independently from the (004) reflection, by solving equation (5), the $\text{Sn}_x\text{Ge}_{1-x}$ (224) asymmetric reflection was used to determine e_{xx} .

$$e_{xx}^{\text{exp}} = \frac{e_{\text{xray}}^{(004)} - e_{\text{xray}}^{(224)} \cos^2 \phi}{\sin^2 \phi} \quad (6)$$

where $e_{\text{xray}}^{(224)} = \frac{\sin \theta_{\text{Ge}}^{(224)}}{\sin(\theta_{\text{Ge}}^{(224)} + \Delta\theta^{(224)})} - 1$ and ϕ is the angle between (004) and (224).

Using the linear relationship between composition and lattice parameter¹² and assuming a coherently strained film, both e_{zz} and e_{xx} were calculated as a function of Sn composition, using equation (8) and equation (7), respectively.¹⁴ Both e_{zz} and e_{xx} calculated in this manner were illustrated as the solid lines in Figure 2.13.

$$e_{xx} = \frac{a_{\text{Ge}} - a^{\text{eq}}_{\text{SnGe}}}{a^{\text{eq}}_{\text{SnGe}}} \quad (7)$$

$$e_{zz} = e_{xx} + \left(\frac{1+\nu}{1-\nu} \right) f \quad (8)$$

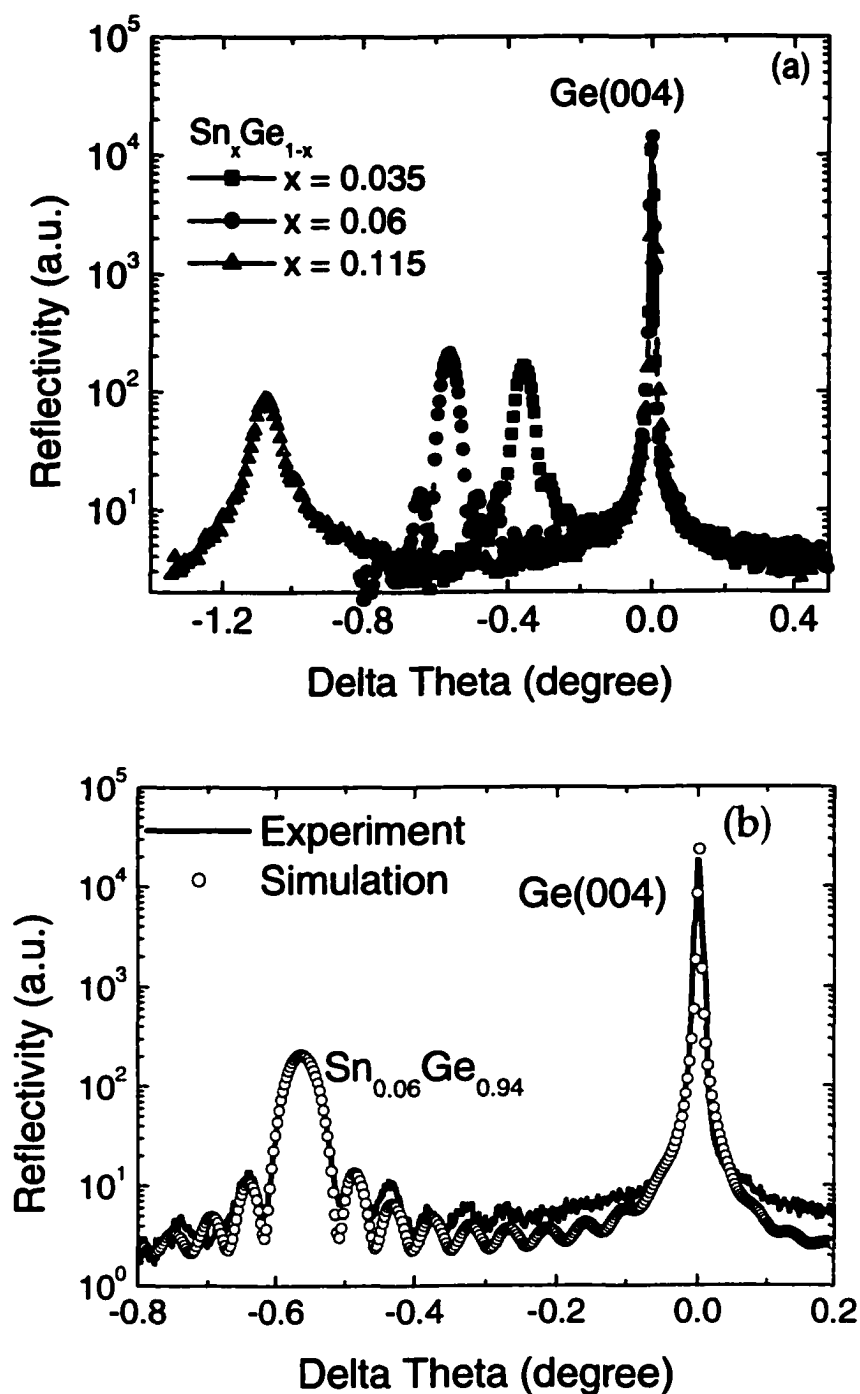


Figure 2.12: Representative HR-XRD ω - 2θ scan of 100 nm $\text{Sn}_x\text{Ge}_{1-x}/\text{Ge}(001)$ films around the Ge(004) reflection. (a) with $x = 0.035, 0.06$ and 0.115 and (b) $\text{Sn}_{0.06}\text{Ge}_{0.94}$ (solid curve) overlaid with dynamical simulation (hollow circles).

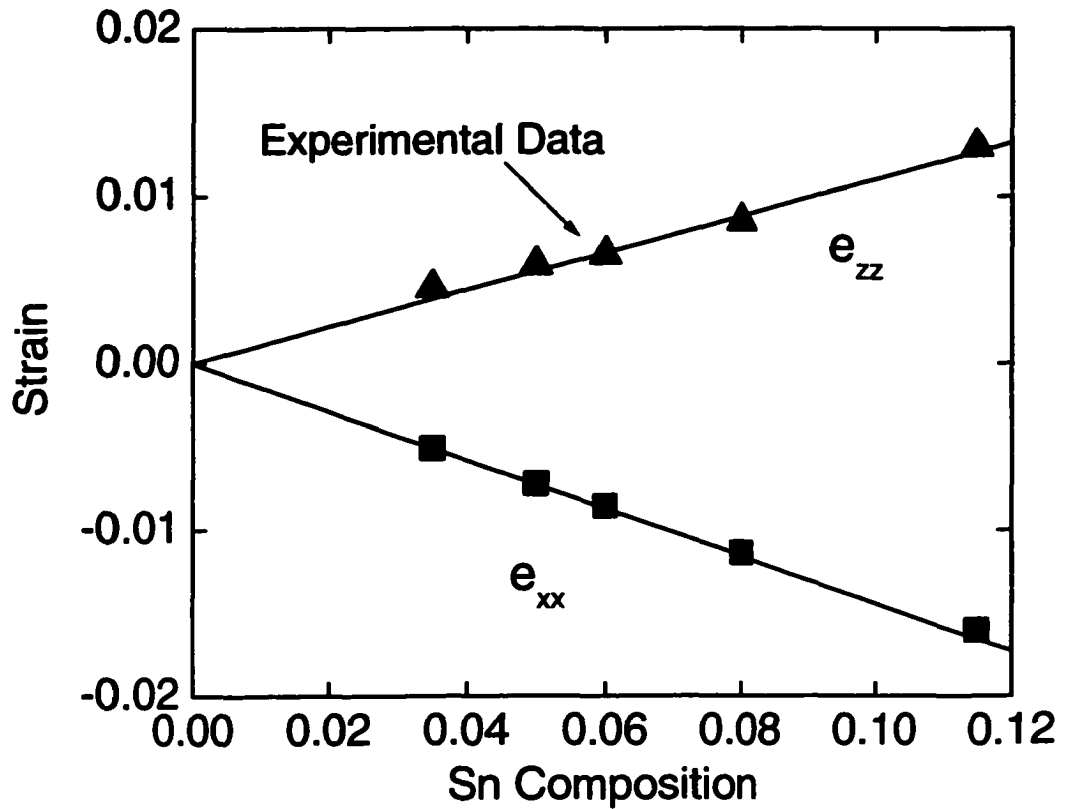


Figure 2.13: Comparison between calculated (solid lines) and experimentally measured strains along the growth direction, e_{zz} (triangles), and in the substrate plane, e_{xx} (squares), for 100 nm coherently-strained $\text{Sn}_x\text{Ge}_{1-x}$ films on Ge(001).

where ν is the Poisson ration and f is the misfit.

$$f = \frac{a^{\text{eq}}_{\text{SnGe}} - a_{\text{Ge}}}{a_{\text{Ge}}} \quad (9)$$

The experimental results for e_{zz} and e_{xx} , represented by triangles and squares in Figure 2.13, respectively, were in agreement with the calculated values using equations (7) and (8) for coherently strained $\text{Sn}_x\text{Ge}_{1-x}$ epitaxial films on Ge(001).

Further evidence for the absence of dislocations was provided in cross-sectional TEM. In Figure 2.14(a), The $\text{Sn}_{0.06}\text{Ge}_{0.94}$ alloy film was imaged under $\vec{g} = [004]$ 2 beam conditions in bright field (diffracted beam blocked by an aperture). The $\text{Sn}_{0.06}\text{Ge}_{0.94}$ epitaxial film did not contain threading dislocations in the region imaged ($0.1 \mu\text{m} \times 1 \mu\text{m}$). Also notable in the (004) bright field image was the presence of the surface undulation measured in AFM. Coherent relaxation of an epitaxial film due to a surface undulation has been predicted theoretically using elastic energy calculations^{17,18} and confirmed experimentally for $\text{Si}_{1-x}\text{Ge}_x$ films in compression.¹⁹ The $\text{Sn}_{0.06}\text{Ge}_{0.94}$ film was also imaged with high-resolution TEM down the [110] zone axis. The lattice fringes at the substrate-film interface are seen to be continuous, hence, the $\text{Sn}_{0.06}\text{Ge}_{0.94}$ film adopts the lattice constant of the Ge substrate. Thus, the high-resolution image of $\text{Sn}_{0.06}\text{Ge}_{0.94}$ shown in Figure 2.14(b) corroborated a coherent interface that was determined from HR-XRD analysis.

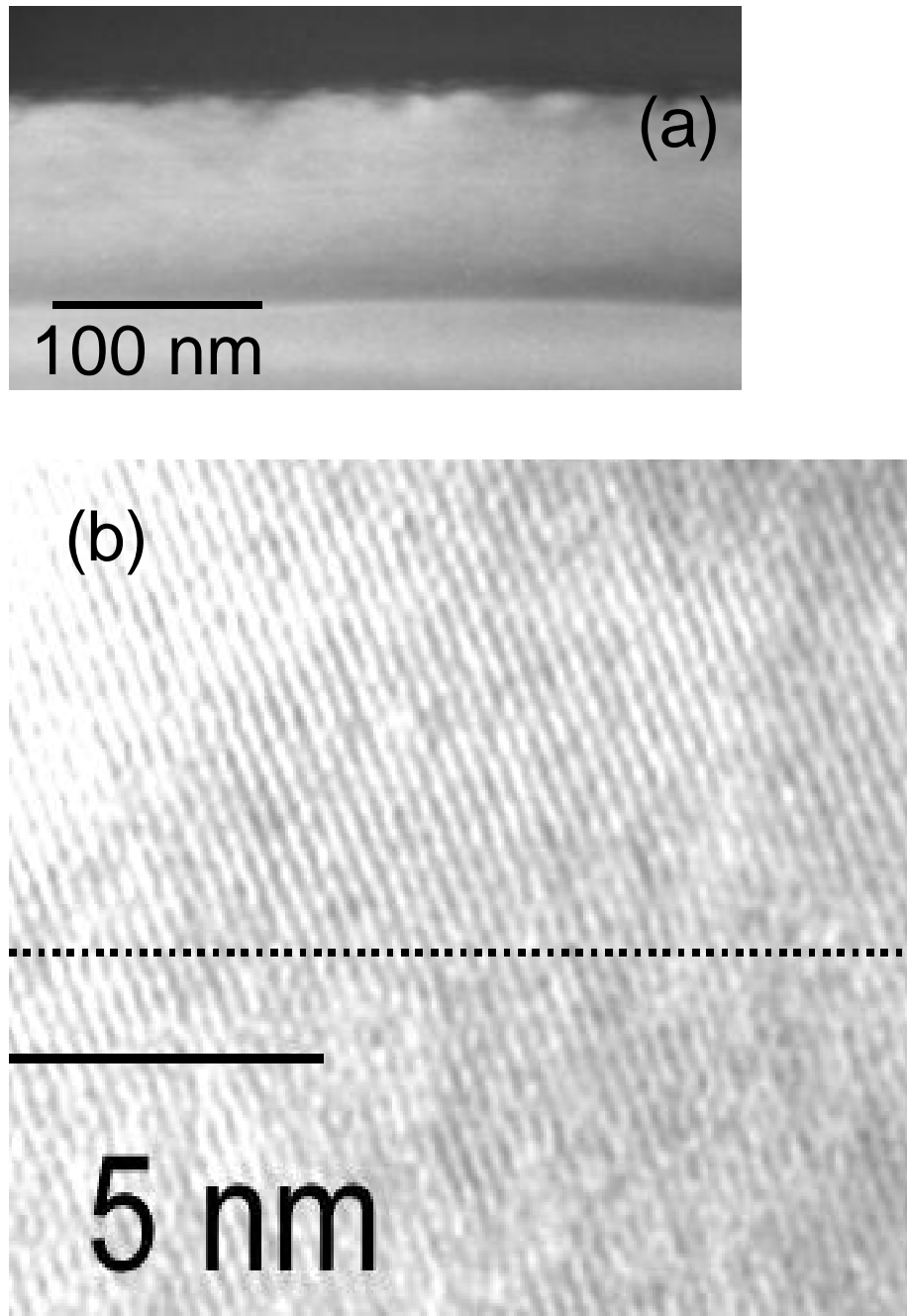


Figure 2.14: $\text{Sn}_{0.06}\text{Ge}_{0.94}/\text{Ge}(004)$ imaged (a) under $\vec{g} = [004]$ 2 beam conditions and (b) along $[110]$ zone axis at high resolution. The $\text{Sn}_{0.06}\text{Ge}_{0.94}/\text{Ge}$ interface (represented as a dashed line) has continuous lattice fringes.

2.5 Thermodynamics of coherency

A series of single layer $\text{Sn}_x\text{Ge}_{1-x}$ films were grown on Ge(001) with $0 < x < 0.12$ and thickness up to 300 nm to investigate the maximum thickness for coherently strained epitaxial films. As mentioned previously, the $\text{Sn}_x\text{Ge}_{1-x}$ lattice undergoes tetragonal distortion. A volume, or thickness, dependent elastic energy is stored in the film as a result of tetragonal distortion and this coherency energy can be relieved by dislocation introduction. The atoms surrounding the dislocation core increase the energy density of the film and this increase is independent of film thickness. Therefore, a critical film thickness exists at thermodynamic equilibrium below which it is energetically unfavorable for dislocation introduction and above which the energy of the system can be reduced by strain-relieving threading dislocations. The critical thickness, h_c , was calculated in equation (10) by summing the total areal energy density of a semi-coherent film and minimizing this energy as a function of dislocation density.¹³

$$h_c = \frac{b}{8\pi f \cos \lambda} \left(\frac{1 - \nu \cos^2 \beta}{1 + \nu} \right) \ln \left(\frac{4h_c}{b} \right) \quad (10)$$

where f is the misfit and b is the burgers vector. Notice that only the edge component, $b \cos \lambda$, of the burgers vector relieves coherency energy. Since the energy density associated with dislocations is dependent on the square of the magnitude of the burgers vector, the shortest burgers vector of the lattice is adopted to minimize energy. For the diamond cubic crystal structure, the

shortest burgers vector is of the type $\frac{1}{2}$ [110]; therefore, λ is taken as 60° in the calculation. The transcendental equation (10) was solved numerically. From HR-XRD measurements, $\text{Sn}_x\text{Ge}_{1-x}$ alloy films with $0.035 < x < 0.115$ and maximum film thickness of 219 nm were determined to be coherently strained on Ge(001).²⁰ These films thickness substantially exceed the critical thickness predicted by equation (10).¹³ For instance, a $\text{Sn}_x\text{Ge}_{1-x}$ alloy film with $x = 0.078$ and film thickness of 155 nm was coherently-strained, whereas the thermodynamic calculation predicted a critical thickness of 9.3 nm. A series of films with $0.035 < x < 0.115$ (closed circles in Figure 2.15) were obtained beyond the predicted thermodynamic critical thickness (solid curve). The experimental results were not surprising due to the low growth temperature. For $\text{Si}_{1-x}\text{Ge}_x$ heterostructures, a kinetic phenomenological model yields stress-temperature diagrams where the amount of strain relaxation is small ($< 10^7$) at low growth temperatures ($T < 0.5 T_{\text{melt}}$).¹⁴ Since the $\text{Sn}_x\text{Ge}_{1-x}$ epitaxial films are Sn dilute alloys grown at temperatures ($T < 160^\circ\text{C}$) much less than $0.5 T_{\text{melt}}$ for Ge, the nucleation rate for misfit dislocations is expected to be low, leading to the observed negligible dislocation density. Another mechanism by which a non-hydrostatically stressed film can coherently relax is by the formation of a surface undulation.^{17,18} For a film in compression, as is $\text{Sn}_x\text{Ge}_{1-x}$ on Ge, the lattice constant at the crest of the surface undulation can relax coherently. The $\text{Sn}_x\text{Ge}_{1-x}$

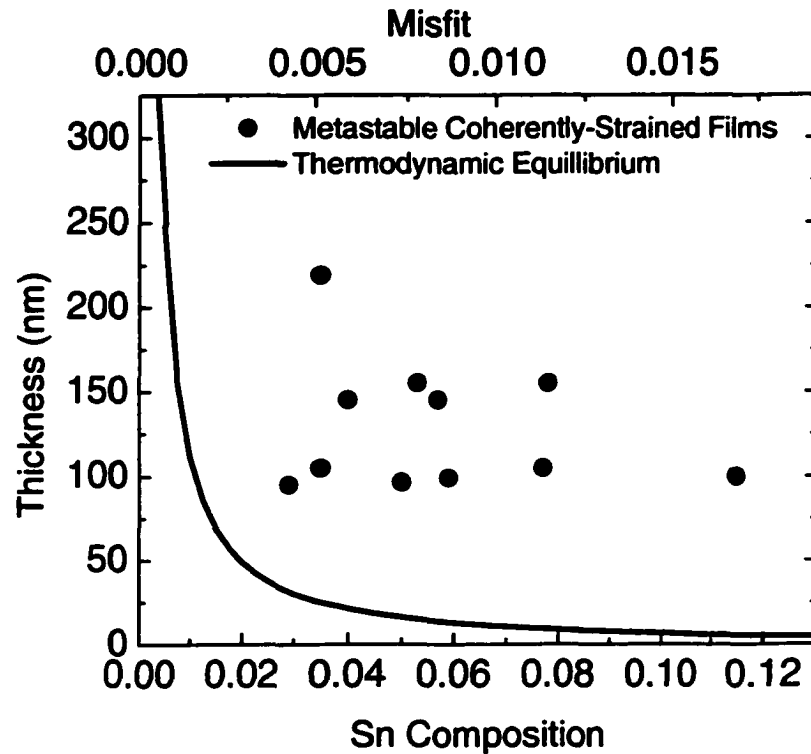


Figure 2.15: Thermodynamic critical thickness, solid curve, compared with experimentally determined thickness of metastable coherently strained $\text{Sn}_x\text{Ge}_{1-x}$ films on Ge(001) substrates (solid circles). The experimental film thickness exceeded the calculated thermodynamic critical thickness.

films did exhibit a surface undulation, evident in both AFM and cross-sectional TEM (seen in Figure 2.14a).

2.6 Conclusions

Coherently strained $\text{Sn}_x\text{Ge}_{1-x}/\text{Ge}$ superlattices and single layer $\text{Sn}_x\text{Ge}_{1-x}$ epitaxial films were grown on Ge(001) substrates. These solid solutions were grown in excess of the thermodynamic solid solubility of Sn in Ge ($x = 0.01$). The growth temperature was optimized, $140^\circ\text{C} < T < 160^\circ\text{C}$, to maximize the

thickness for coherent epitaxial growth and to eliminate Sn surface segregation. RBS measured the Sn composition in the films and confirmed that Sn surface segregation did not occur. Both HR-XRD and cross-section TEM analysis revealed the coherent interface between the $\text{Sn}_x\text{Ge}_{1-x}$ films and Ge(001) substrate. A thermodynamic argument estimating the thermodynamic critical thickness for dislocation introduction was investigated and compared with the experimentally determined thickness for coherent epitaxial growth. The $\text{Sn}_x\text{Ge}_{1-x}$ epitaxial films exceeded the predicted thermodynamic critical thickness. The disagreement between the experimental results and the thermodynamic model had two origins. Film relaxation at the crest of a surface undulation has been documented to relieve coherency energy in the absence of dislocation introduction.^{17,18} Additionally, epitaxial films grown beyond the thermodynamic critical thickness for dislocation introduction are observed for $\text{Si}_x\text{Ge}_{1-x}/\text{Si}(001)$ heterostructures and explained with a kinetic phenomenological model that predicts a low dislocation nucleation rate at low temperatures.

2.7 Bibliography

1. O. Gurdal, D. P. J. R. A. Carlsson, N. Taylor, H. H. Radamson, J. E. Sundgren, and J. E. Greene, *J. Appl. Phys.* **83**, 162 (1998)
2. A. Harwit, P. R. Pukite, J. Angilello, and S. S. Iyer, *Thin Solid Films* **184**, 395 (1990)
3. E. A. Fitzgerald, P. E. Freeland, M. T. Asom, W. P. Lowe, R. A. Macharrie, B. E. Weir, A. R. Kortan, F. A. Thiel, Y. H. Xie, A. M. Sergent, S. L. Cooper, G. A. Thomas, and L. C. Kimmerling, *J. Elec. Mat.* **20**, 489 (1991)
4. G. He and H. A. Atwater, *Nuc. Instrum. Methods B* **106**, 126 (1995)
5. C. D. Thurmond, *J. Phys. Chem* **57**, 827 (1953)
6. C. D. Thurmond, F. A. Trumbore, and M. Kowalchik, *J. Chem. Phys.* **24**, 799 (1956)
7. W. Wegscheider, J. Olajos, U. Menczigar, W. Dondl, and G. Abstreiter, *J. Cryst. Growth* **123**, 75 (1992)
8. G. Abstreiter, J. Olajos, R. Schorer, P. Vogl, and W. Wegscheider, *Semicond. Sci. Tech.* **8**, S6 (1993)
9. D. J. Eaglesham, H. J. Gossmann, M. Cerullo, L. N. Pfeiffer, and K. W. West, *J. Cryst. Growth* **111**, 833 (1991)

10. G. Xue, H. Z. Xiao, M. A. Hassan, J. E. Greene, and H. K. Birnbaum, J. Appl. Phys. **74**, 2512 (1993)
11. G. He and H. A. Atwater, Appl. Phys. Lett. **68**, 664 (1996)
12. G. He and H. A. Atwater, Phys. Rev. Lett. **79**, 1937 (1997)
13. J. W. Matthews and A. E. Blakeslee, J. Cryst. Growth **27**, 118 (1974)
14. J. Y. Tsao, *Material Fundamentals of Molecular Beam Epitaxy* (Academic Press, Inc., 1993).
15. V. P. Kesan, S. S. Iyer, and J. M. Cotte, J. Cryst. Growth **111**, 847 (1991)
16. M. Wormington, C. Panaccione, K. M. Matney, and D. K. Bowen, Philos. Trans. Roy. Soc. (London) A **357**, 2827 (1999)
17. M. A. Grinfel'd, Sov. Phys. Dokl. **290**, 1358 (1986)
18. R. J. Asaro and W. A. Tiller, Met. Trans. **3**, 1789 (1972)
19. Y. H. Xie, G. H. Gilmer, C. Roland, P. J. Silverman, S. K. Buratto, J. Y. Cheng, E. A. Fitzgerald, A. R. Kortan, S. Schuppler, M. A. Marcus, and P. H. Cittrin, Phys. Rev. Lett. **73**, 3006 (1994)
20. R. Ragan and H. A. Atwater, Appl. Phys. Lett. **77**, 3418 (2000)

Chapter 3 Optical Characterization of Coherent, Homogeneous Sn_xGe_{1-x} Alloys

3.1 Introduction

Due to the predictions of a fundamental direct energy bandgap for Sn_xGe_{1-x} binary alloys with compositions in excess of $x = 0.2$ by tight-binding¹ and pseudopotential² bandstructure calculations, the characterization of the Sn_xGe_{1-x} bandstructure became of practical interest for infrared optoelectronic device applications.³⁻⁵ Both Sn and Ge are group IV elements and isoelectronic with Si. The low growth temperature of Sn_xGe_{1-x} alloys allows for deposition of the alloy post integrated circuit processing, which is favorable for the monolithic integration of Sn_xGe_{1-x} infrared detectors with Si ULSI technology. Ge is an indirect energy bandgap semiconductor with eight degenerate conduction band minima or valleys at the L point ($k = 2\pi/a (\frac{1}{2}, \frac{1}{2}, \frac{1}{2})$) in reciprocal space. The local minima of the conduction band at the Brillouin zone center, or the Γ point ($k = (0, 0, 0)$), of Ge sits 130 meV above the L point (0.67 eV). Diamond cubic Sn (or α -Sn) is a semimetal with a conduction band minima at the Γ point sitting

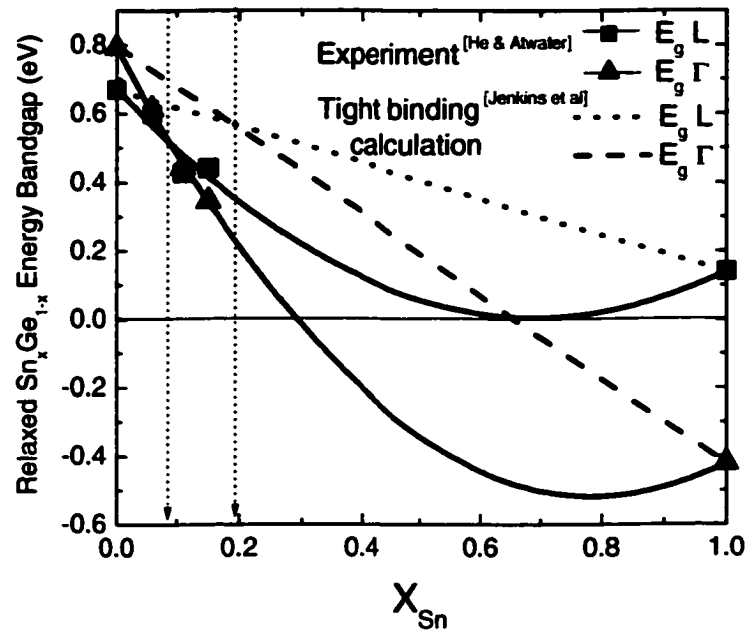


Figure 3.1: Alloy effect on relaxed $\text{Sn}_x\text{Ge}_{1-x}$ bandstructure: experimental measurement (symbols) [He & Atwater, 1997] and tight-binding calculation (dotted and dashed lines) [Jenkins & Dow, 1987].

0.4 eV below the valence band. By alloying Sn and Ge, the conduction band extrema at both the L point and Γ points in k-space were predicted to decrease in energy with increasing Sn composition. The gamma point was predicted to decrease more rapidly. The tight-binding bandstructure calculation predicted that the alloy would undergo an indirect to direct bandgap transition with a continuously tunable direct energy bandgap in the infrared from 0.55 eV to 0 eV for Sn compositions of $x = 0.2$ to 0.6 . The indirect (dotted curve) to direct (dashed curve) energy bandgap transition predicted by the bandstructure calculation is depicted in Figure 3.1. α -Sn has a low electron effective mass, $0.0236 m_0$, thus, the $\text{Sn}_x\text{Ge}_{1-x}$ alloy was also predicted to have a high electron mobility.^{1,2,6,7}

The indirect to direct bandgap transition was measured at a Sn composition of $x = 0.10$ for strain-relieved alloys on Si(001) (Figure 3.1),⁵ much lower than the calculated prediction of $x = 0.2$. The measured direct energy bandgap of strain-relieved $\text{Sn}_x\text{Ge}_{1-x}$ solid solutions varies from 0.35 eV to 0.80 eV as the Sn composition ranges from $x = 0.15$ to $x = 0$, represented in Figure 3.1 as closed triangles.⁵ The discrepancy between the bandstructure calculation and the experimental results has been attributed to a bowing of the bandgap produced by local distortions in the bond lengths and bond angles of the crystal.⁵ By the using the virtual crystal approximation where each atom has the average properties of the alloy, the tight-binding calculation does not take into account electronic perturbations associated with local distortions in the crystal lattice .

Coherency strain may alter the electronic structure further. As mentioned previously, in order to reduce the dislocation density of the alloy layers, $\text{Sn}_x\text{Ge}_{1-x}$ epitaxial films were grown coherently strained on Ge(001). Deformation potential theory as defined by Braden and Schockley,⁸ describes the perturbation of the electronic structure due to dilations of the unit cell. In the case of $\text{Si}_x\text{Ge}_{1-x}/\text{Si}(001)$, coherency strain was expected to reduce the indirect bandgap from 0.94 eV to 0.76 eV as the Ge composition ranged from $0 < x < 0.4$, with a corresponding misfit of 1.7% with respect to Si(001).^{9,10}

In this chapter, the effect of the tetragonal distortion of the unit cell on the $\text{Sn}_x\text{Ge}_{1-x}$ energy bandgap is described. The effects of coherency strain were investigated both theoretically, using deformation potential theory, and

experimentally, by the measurement of the energy bandgap of coherently strained $\text{Sn}_x\text{Ge}_{1-x}/\text{Ge}(001)$ alloys via transmittance in a Fourier transform infrared (FT-IR) spectrometer. The measured energy bandgap as a function of Sn composition for coherently strained $\text{Sn}_x\text{Ge}_{1-x}/\text{Ge}(001)$ alloys was strongly dependent on Sn concentration with a negligible strain contribution. Deformation potential theory agreed with a small strain contribution on the magnitude of the $\text{Sn}_x\text{Ge}_{1-x}/\text{Ge}(001)$ energy bandgap when the strain axis was along [001]. For $\text{Sn}_x\text{Ge}_{1-x}/\text{Ge}(111)$ alloys, the L point was expected to decrease dramatically with strain. When the strain axis was along [111], an indirect to direct bandgap transition was not predicted according to deformation potential theory calculations.

3.2 Photoluminescence of dilute $\text{Sn}_x\text{Ge}_{1-x}/\text{Ge}(001)$ superlattices

It has been proposed that compressive stress could dramatically change the electronic properties of Sn dilute $\text{Sn}_x\text{Ge}_{1-x}$ alloys, $x > 0.02$.¹¹ In section 2.1, the challenges associated with growing $\text{Sn}_x\text{Ge}_{1-x}$ alloys with $x > 0.15$ were described in detail. Thus, it would be beneficial if coherency strain shifted the indirect to direct energy bandgap transition to lower Sn compositions. The Γ point was predicted to decrease more rapidly with strain than the L point.¹¹ The indirect to direct transition was predicted to occur at a Sn composition of $x = 0.02$.¹¹ In

order to probe the extrema points of the bandstructure of Sn dilute coherently strained $\text{Sn}_x\text{Ge}_{1-x}$ alloys, photoluminescence (PL) measurements were performed on $\text{Sn}_x\text{Ge}_{1-x}/\text{Ge}$ superlattice structures with $0.02 < x < 0.04$ and thickness up to 300 nm. (The microstructure was described in section 2.2). A Ge cap layer was grown as the final layer of the superlattice structure to eliminate surface recombination sites on the top $\text{Sn}_x\text{Ge}_{1-x}$ layer.

A 457.9 nm Ar^+ laser with $100 \text{ mW}/\text{mm}^2$ was used for carrier excitation and a grating spectrometer with spectral resolution of 3.2 nm was coupled to an InSb detector to measure PL emission. The maximum emission wavelength detectable with the InSb detector was $5 \mu\text{m}$ or 0.24 eV. The sample temperature was controlled between 12 K and 300 K with a closed circuit He cryostat. PL intensity was not detected from these films. Further characterization was needed to determine whether the film quality or the lack of an indirect to direct bandgap transition was responsible for the absence of a PL signal. A quantitative calculation was necessary to determine the effect of coherency strain on the $\text{Sn}_x\text{Ge}_{1-x}$ bandstructure.¹²

3.3 Deformation potential theory

3.3.1 Background

Deformation potential theory can be used to estimate the strain-induced shifts in energy band extrema for non-polar semiconductors such as Si and Ge.⁸

The concept behind deformation potential theory is the method of effective mass where the motion of electrons is described by assigning an appropriate effective mass to the electron in a gradually varying potential. This method is valid when the change of the gradually varying potential is small compared to the periodic potential over one unit cell.¹³⁻¹⁵ The gradually varying potential associated with coherency strain arises from scattering of acoustic lattice vibrations due to dilations of the unit cell; thus, deformation potential theory is only valid for non-polar semiconductors.

3.3.2 Theoretical calculation for $\text{Sn}_x\text{Ge}_{1-x}/\text{Ge}(001)$ and $\text{Sn}_x\text{Ge}_{1-x}/\text{Ge}(111)$ bandstructure

The tetragonal distortion, in plane compression and out of plane expansion, of the $\text{Sn}_x\text{Ge}_{1-x}$ unit cell is a consequence of coherent registry with the Ge substrate.¹⁶ For a biaxially strained alloy in compression, the resulting stress fields can be mechanically decomposed into a hydrostatic compression and a uniaxial elongation.⁹ The effect of coherency strain at the extrema points of the $\text{Sn}_x\text{Ge}_{1-x}$ bandstructure was examined first by the uniaxial splitting of the valence band, then the uniaxial splitting of the conduction band, and last of all the uniform hydrostatic shift of the extrema.

3.3.2.1 Valence band

The effect of strain on the valence band of $\text{Sn}_x\text{Ge}_{1-x}$ alloys was examined using a Hamiltonian derived from crystal symmetry:¹⁷

$$H_v = H_0^v + D_d^v(e_{xx} + e_{yy} + e_{zz}) + \frac{2}{3}D_u [J_x^2 - \frac{1}{3}J^2] e_{xx} + \text{c.p.} \quad (11)$$

$$+ \frac{2}{3} D_u [\frac{1}{2} (J_y J_z + J_z J_y) e_{yz} + \text{c.p.}]$$

where H_0^v is the Hamiltonian in the absence of strain, D_d^v is the valence band deformation potential constant, $\vec{J} = (J_x, J_y, J_z)$ is the hole angular momentum, D_u (D_u') is the deformation potential constant associated with distortions along [001] ([111]), and c.p. denotes cyclic permutations. The components of the strain tensor, e_{ii} , are different for strain oriented along [001] from those with strain oriented along [111]. Due to the size of the lattice mismatch between $\text{Sn}_x\text{Ge}_{1-x}$ and Ge, the spin-orbit interaction must be included in the Hamiltonian to accurately characterize the energy band deformation. The strain/spin-orbit Hamiltonian is a 6×6 matrix in the (J, M_J) representation, seen in equation (12). As can be seen from the Hamiltonian, no mixing occurs for states with different values of M_J , thus, M_J remains a good quantum number. The energy eigenvalues, equations (13) through (15), obtained by diagonalizing the Hamiltonian, are uniquely represented in the (J, M_J) representation.

$$M_J = \begin{matrix} 3/2 & 1/2 & -1/2 & -3/2 & 1/2 & -1/2 \end{matrix} \quad (12)$$

$$H = H_e + H_{SO} = \begin{bmatrix} \varepsilon & 0 & 0 & 0 & 0 & 0 \\ 0 & -\varepsilon & 0 & 0 & -2\sqrt{\varepsilon} & 0 \\ 0 & 0 & -\varepsilon & 0 & 0 & 2\sqrt{\varepsilon} \\ 0 & 0 & 0 & \varepsilon & 0 & 0 \\ 0 & -2\sqrt{\varepsilon} & 0 & 0 & -\Lambda & 0 \\ 0 & 0 & 2\sqrt{\varepsilon} & 0 & 0 & -\Lambda \end{bmatrix}$$

where the eigenvalues are:

$$\varepsilon(\pm \frac{3}{2}) = \varepsilon(x) \quad (13)$$

$$\varepsilon(\pm \frac{1}{2}) = -\frac{1}{2} [\varepsilon(x) + \Lambda(x)] + \frac{1}{2} [9\varepsilon^2(x) + \Lambda^2(x) - 2\varepsilon(x)\Lambda(x)]^{1/2} \quad (14)$$

$$\varepsilon(\pm \frac{1}{2}) = -\frac{1}{2} [\varepsilon(x) + \Lambda(x)] - \frac{1}{2} [9\varepsilon^2(x) + \Lambda^2(x) - 2\varepsilon(x)\Lambda(x)]^{1/2} \quad (15)$$

where Λ is the spin-orbit splitting, linearly interpolated from pure Sn and Ge and

$$\varepsilon(x) = \frac{2}{3} D_u [e_{zz}(x) - e_{xx}(x)] \varepsilon(x) \quad \text{strain axis along [001]} \quad (16)$$

$$\varepsilon(x) = \frac{1}{3} D_u' e_{xy}(x) \quad \text{strain axis along [111]} \quad (17)$$

Since the deformation potential constants for Sn were unknown, the deformation potential constants of Ge were used to model strain effects on the $\text{Sn}_x\text{Ge}_{1-x}$ alloy bandstructure. This was a reasonable approximation due to the low Sn content in the region of interest, $x < 0.12$. The values of the deformation potential constants used in the valence band calculation were obtained experimentally from piezo-electroreflectance data: $D_u = 3.81 \pm 0.25$ eV and $D_u' = 8.14 \pm 0.5$ eV.¹⁸ In the presence of strain, the 4-fold degeneracy of the valence band was lifted; the

energy of heavy hole valence band, $E_v(\frac{3}{2}, \pm\frac{3}{2})$, was calculated to increase while the energy of light hole, $E_v(\frac{3}{2}, \pm\frac{1}{2})$, valence band was calculated to decrease, as shown in Figure 3.2. Thus, the valence band deformation was expected to give rise to a decrease in E_g as well as a decrease in the density of states at the valence band maxima. The increase in the energy of the heavy hole valence band was expected to be larger when the strain axis was along [001] versus [111].

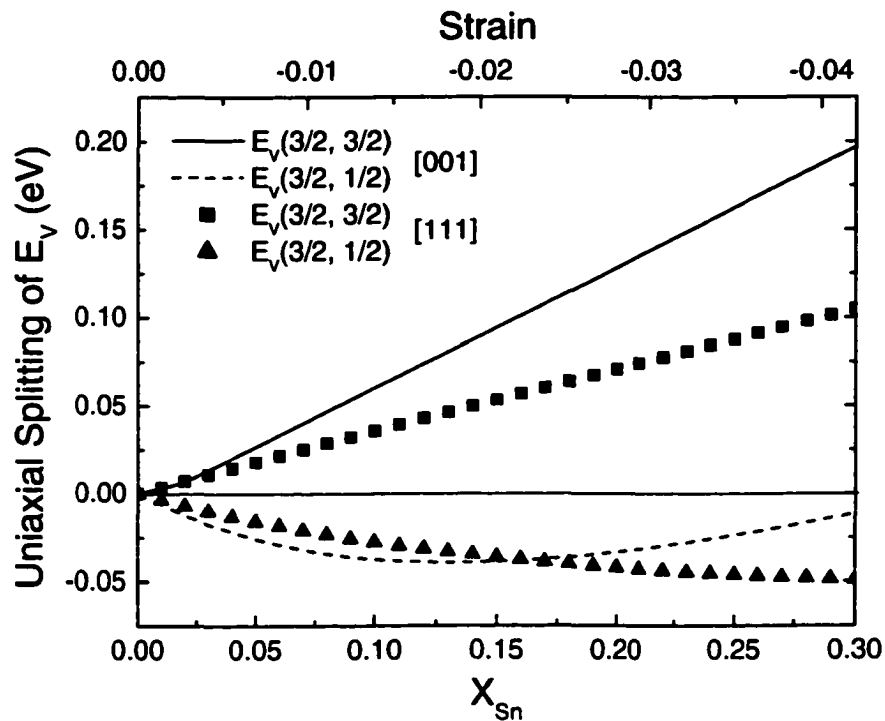


Figure 3.2: Uniaxial deformation of the E_{vhh} and E_{vlh} . The lines represent strain axis along [001] and the symbols along [111].

3.3.2.2 Conduction band

The unperturbed bandstructure of Ge has eight degenerate ellipsoidal constant energy surfaces found in reciprocal space at $k = 2\pi/a (\frac{1}{2}, \frac{1}{2}, \frac{1}{2})$ along

{111} depicted in Figure 3.3. The perturbation resulting from coherency strain on the conduction band was calculated by solving the Boltzmann equation for the three components of the energy dependent relaxation time tensor for the case when electron scattering occurs by acoustic lattice vibrations.¹⁹ These three components are in the directions of the three principle axes of the ellipsoidal constant energy surface. From the relaxation time tensor, macroscopic properties

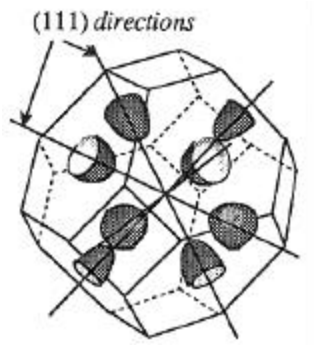


Figure 3.3: Schematic of ellipsoidal constant energy surfaces in Ge.

such as mobility, piezo-resistance, and the deformation potential constants can be calculated. The total conduction band energy shift for a valley in the k^i direction is given by¹⁹

$$\Delta E_c^{(i)} = \left[\Xi_d \bar{1} + \Xi_u \{ \hat{a}_i \otimes \hat{a}_i \} \right] * \bar{e} \quad (18)$$

where Ξ_d, Ξ_u are the dilation and uniaxial deformation potential constants, $\bar{1}$ is the unit tensor, \hat{a}_i is the unit vector in the direction of the conduction band valley, \bar{e} is the strain tensor, \otimes denotes an outer product, and $*$ denotes an inner

product. The mean energy shift of the conduction band extrema was calculated from the following:¹⁹

$$\Delta E_c^{(0)} = \left(\Xi_d + \frac{1}{3} \Xi_u \right) \bar{1} * \bar{e} \quad (19)$$

The values used for the deformation potential constants in the analysis were calculated by fitting cyclotron resonance data of Ge and are $\Xi_u = 17.0 \pm 0.6$ eV and $\Xi_d = -10.88 \pm 0.47$ eV.²⁰ The uniaxial component of the conduction band deformation was then calculated by subtracting equation (19) from equation (18). Due to the symmetry of the eight $\langle 111 \rangle$ conduction band valleys around the [001] direction, the uniaxial splitting of the conduction band is zero. That is, the conduction band valleys shift uniformly. The symmetry is broken when the strain axis is along [111] and the uniaxial splitting is given by

$$\begin{aligned} \Delta E_c^{(i)} - \Delta E_c^{(0)} &= 2\Xi_u e_4 \Rightarrow k^{(i)} = (111), (\bar{1}\bar{1}\bar{1}) \\ \Delta E_c^{(i)} - \Delta E_c^{(0)} &= -\frac{2}{3}\Xi_u e_4 \Rightarrow k^{(i)} = (\bar{1}11), (1\bar{1}\bar{1}), (11\bar{1}), (\bar{1}\bar{1}1), (\bar{1}1\bar{1}), (1\bar{1}1) \end{aligned} \quad (20)$$

The six conduction band valleys off the strain axis significantly decreased in energy at L_6 with strain, 150 meV for $x = 0.10$, according to the deformation potential theory calculation. The variation of the bandgap energy at the L_6 point and Γ_7 point predicted by the theory is shown in Figure 3.4. The conduction band valleys parallel to the strain axis were predicted to increase while the

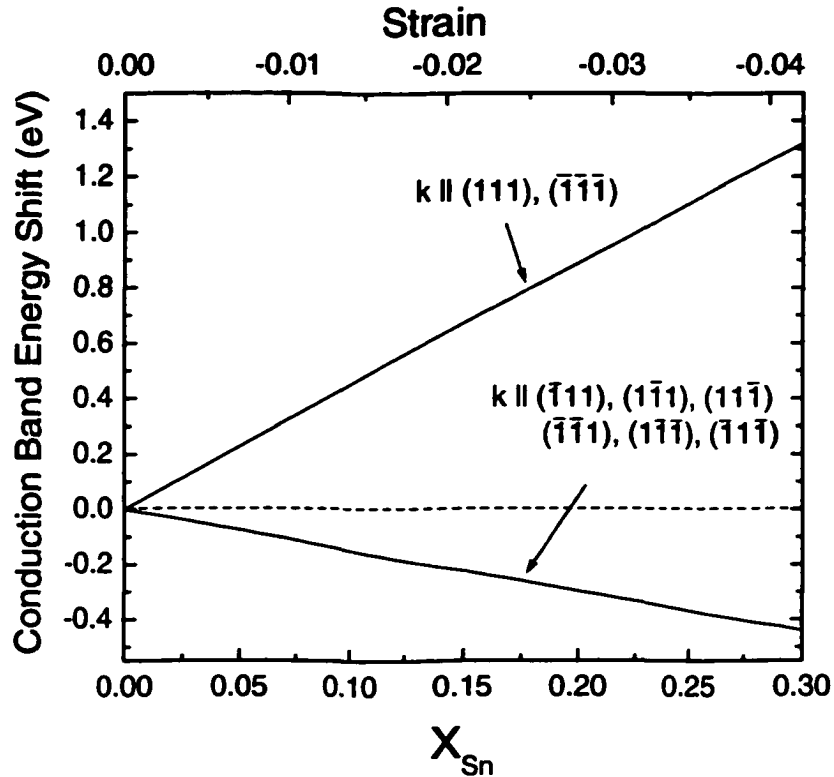


Figure 3.4: Uniaxial splitting of the conduction band at L_6 due to uniaxial strain along $[111]$.

conduction band valleys off the strain axis were predicted to decrease, giving rise to a large splitting.

3.3.2.3 Hydrostatic component

The energy associated with hydrostatic compressions of the Ge unit cell can be understood qualitatively by examining the relationship between energy and atomic spacing for carbon arranged in the diamond lattice illustrated in Figure 3.5.²¹ When the carbon atoms are brought in close proximity, the atomic wavefunctions overlap and the electron wavefunctions become superpositions of atomic states. The energy levels split and form a continuum of states. The

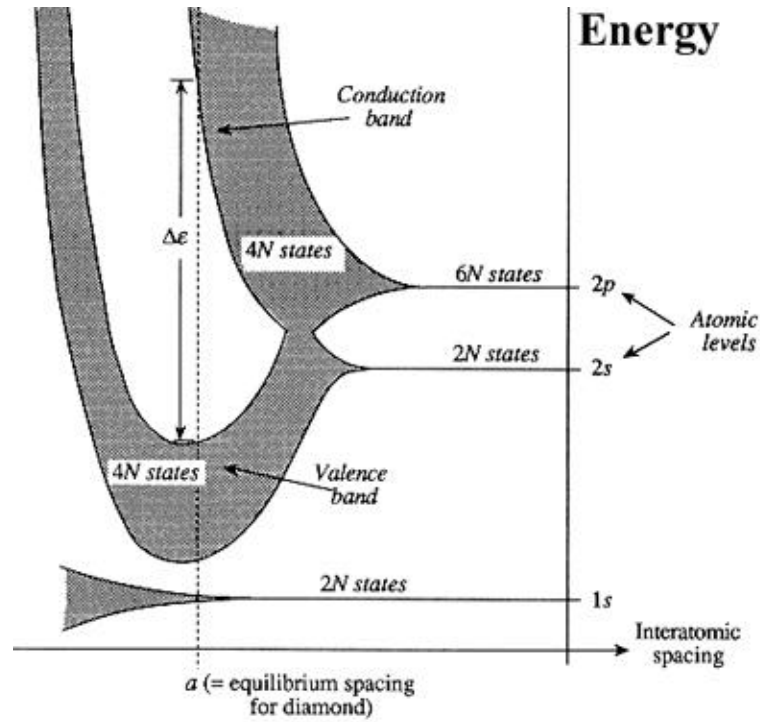


Figure 3.5: Energy levels versus lattice spacing for diamond. [Kimball, 1935]

for the electrons and $\Delta\varepsilon$ is the energy bandgap where allowed states do not exist. As seen in Figure 3.5, the energy bandgap is a function of the equilibrium lattice parameter. If the interatomic spacing or lattice parameter decreases, such as in hydrostatic compression, the energy difference between the conduction band and valence band increases, thus, increasing the energy of the bandgap.

The energy bandgap shift arising from hydrostatic compressions is also calculated from the solution of the Boltzmann equation for the energy dependent relaxation time tensor and is expressed by:¹⁹

$$\Delta E_G^{Hydro} = (\Xi_d + \frac{1}{3}\Xi_u - \mathbf{g})l^*e \quad (21)$$

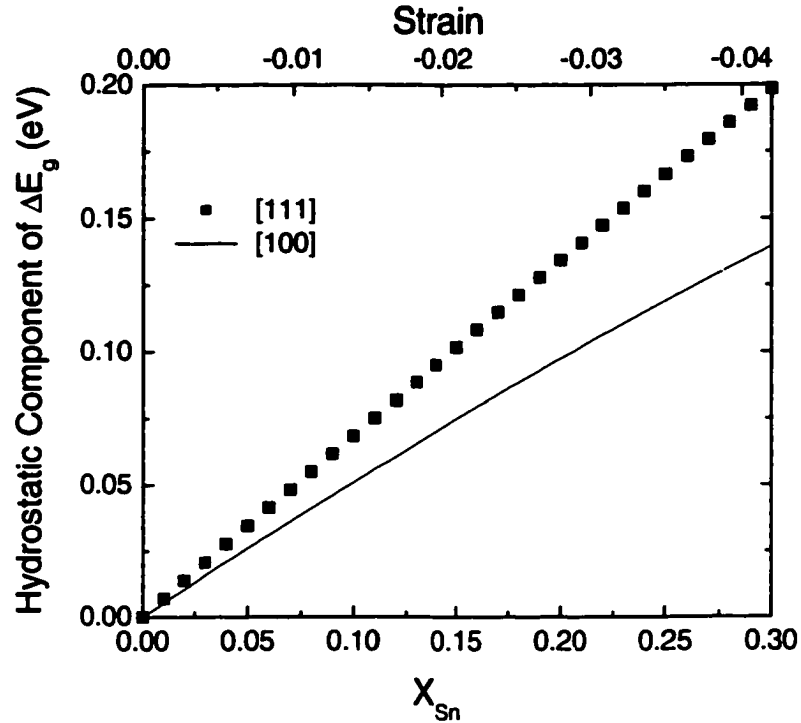


Figure 3.6: Hydrostatic component of ΔE_g represented by squares for strain along [111] and a line for strain along [001].

where γ is the deformation potential constant associated with uniform shifts of the valence band due to dilations. Dilations, $\Delta V/V$, associated with $\text{Sn}_x\text{Ge}_{1-x}$ on Ge are negative since the alloy is in compression. The sum of the three deformation potential constants in equation (21) is also negative for Ge, -2.9 eV;²² thus, hydrostatic pressure increases the $\text{Sn}_x\text{Ge}_{1-x}$ bandgap, as illustrated in Figure 3.6. At a Sn composition of 10%, the hydrostatic component was expected to increase the energy by 50 meV when the strain axis was along [001] and 68 meV when the strain axis was along [111].

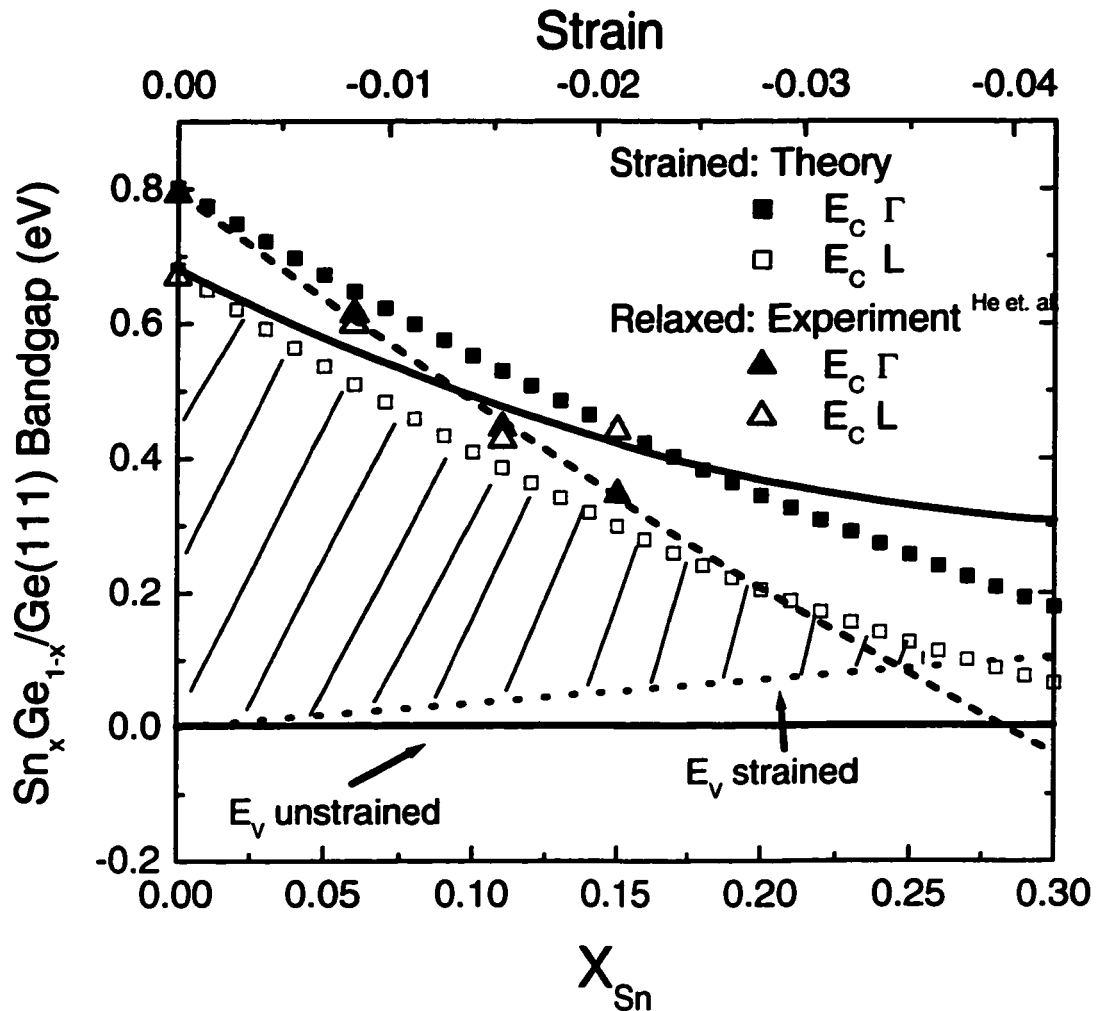


Figure 3.7: Plot of E_C, Γ for strained (closed squares) and relaxed (closed triangles) [He & Atwater, 1997], of E_C, L for strained (open squares) and relaxed (open triangles), and strained $E_{V,hh}$ (dotted) for $\text{Sn}_x\text{Ge}_{1-x}$ on Ge(111). E_g is shaded for the strained alloy.

3.3.3 Summary of DPT predictions for $\text{Sn}_x\text{Ge}_{1-x}$

$/\text{Ge}(001)$ and $\text{Sn}_x\text{Ge}_{1-x}/\text{Ge}(111)$ bandstructure

For epitaxial coherently strained $\text{Sn}_x\text{Ge}_{1-x}$ on Ge(001), the increase in $E_{V,hh}$ decreased the bandgap but the hydrostatic component increased the bandgap by

a comparable amount. Thus, strain was not predicted to dramatically change the magnitude of E_g when the stress axis was along [001]. The bandgap energy was calculated to decrease by 16 meV at a Sn composition of $x = 0.10$. Since Γ_7 and L_6 shifted uniformly with strain, the indirect to direct energy transition should be dominated by the alloy effect and remain near $x = 0.09$, as measured for relaxed $\text{Sn}_x\text{Ge}_{1-x}$ alloys on Si(001).⁵ Alternatively, when the strain axis was along [111], L_6 was calculated to decrease due to the uniaxial splitting of the conduction band (Figure 3.4) while Γ_7 increased due to the hydrostatic component (Figure 3.6). For a Sn composition of $x = 0.10$, L_6 lies 150 meV below Γ_7 . Hence, in the composition range of interest, $x < 0.20$, the effect of strain dominates over the alloy effect and an indirect to direct energy bandgap transition was not predicted for coherent $\text{Sn}_x\text{Ge}_{1-x}$ on Ge(111), as indicated in Figure 3.7.

3.4 Measurement of the $\text{Sn}_x\text{Ge}_{1-x}/\text{Ge}(001)$ energy bandgap

3.4.1 Experiment

The direct energy gap of coherently strained $\text{Sn}_x\text{Ge}_{1-x}$ alloys on Ge(001) substrates with Sn compositions of $0.035 < x < 0.115$ and film thickness of 100 nm was measured. The growth technique and determination of coherency to the Ge(001) substrate was described in detail in Chapter 2 and will not be discussed

here. In order to characterize the effect of strain on the energy gap, infrared transmittance and reflectance measurements were performed using a Nicolet Magna 760 FT-IR spectrometer between 1000-8000 cm^{-1} at 300 K. The spectrometer was continuously purged with dry nitrogen to avoid absorption of the IR signal by the ambient composed partly of CO_2 and H_2O . An aperture was used to limit the incident radiation on the sample to a spot size of 10 mm. A background signal was taken before and after the sample measurement to confirm the stability of the IR signal. The transmitted signal varied by less than 0.5% between the two measurements. The optical transmittance and reflectance was calculated by dividing the measured signal intensity by the through beam intensity.

Based on experimental results for strain-relieved $\text{Sn}_x\text{Ge}_{1-x}$ alloys⁵ combined with deformation potential theory predictions, the lowest composition $\text{Sn}_x\text{Ge}_{1-x}$ alloy that was predicted to exhibit a direct energy bandgap was $x = 0.09$. At this alloy composition, the corresponding bandgap energy is 0.5 eV (2.5 μm). Although PL is a more straightforward measurement of the direct bandgap energy in comparison to absorption, losses in standard optical lenses become problematic at wavelengths greater than 2 μm . Thus, optical absorption via transmittance and reflectance was employed to measure the energy bandgap of coherently strained $\text{Sn}_x\text{Ge}_{1-x}$ alloys. FT-IR spectroscopy is advantageous because all wavelengths are measured simultaneously; thus, good statistics are obtained during a short measurement interval.

Reflectance measurements were taken at a 50 degree angle of incidence and are shown in Figure 3.8(a) for Sn compositions of $x = 0.05$ and 0.08 . The higher reflectance above the bandgap energy was attributed to a monotonic increase in the refractive index with increasing Sn content in agreement with previous reports.⁵ Transmittance measurement were taken at normal incidence and are shown in Figure 3.8(b) for $\text{Sn}_x\text{Ge}_{1-x}$ alloys with $x = 0.035, 0.06$ and $.0.115$. Transmittance decreased near 0.6 eV as the Sn composition in the $\text{Sn}_x\text{Ge}_{1-x}$ alloys increased. The change in transmittance was small because the films were 100 nm thick.

In order to determine the dependence of the energy bandgap on Sn composition, the reflectance and transmittance spectra were simulated between 3000 and 8000 cm^{-1} using a commercial software package.² The simulation calculates the reflectance and transmittance spectra by solving the Maxwell equations at the air-film, film-substrate and substrate-air interfaces. The transmittance and reflectance depend on the film thickness and the dielectric function. The film thickness was measured in RBS and HR-XRD and the dielectric function is the desired output from the simulation. The dielectric function is:

$$\tilde{n} = n - ik \quad (22)$$

² SCI, Optical Thin Film Software

where n is the refractive index and k is the extinction coefficient. From the extinction coefficient, the absorption coefficient can be calculated:

$$\alpha(\omega) = 2\omega k(\omega) \quad (23)$$

The absorption edge can be fit to obtain the value of the energy bandgap. Using the parabolic band approximation, a functional form of the absorption coefficient has a power dependence on the direct energy bandgap of 0.5 and on the indirect energy bandgap of 2. Transitions between bandtails that are associated with disorder in the crystal lattice can be included in the functional of the absorption coefficient by using Urbach's rule.²³

The simulation software required initial input for the dielectric function. The above method was performed backward, that is the change in $\text{Sn}_x\text{Ge}_{1-x}$ bandgap energy predicted by deformation potential theory calculations¹² coupled with previous energy bandgap measurements for strain-relieved alloys⁵ were used to calculate the absorption coefficient from which the extinction coefficient could be calculated. The refractive index of $\text{Sn}_x\text{Ge}_{1-x}$ was used as input for the refractive index in the simulation.⁵ The software iteratively fit the transmittance and reflectance spectra and generated a new value for the dielectric function. The experimental value of the bandgap (Figure 3.9) was then determined by repeating the above method until the root-mean-square error between the simulated and experimental transmittance data was minimized. The results for the indirect and direct energy gap obtained by the above analysis

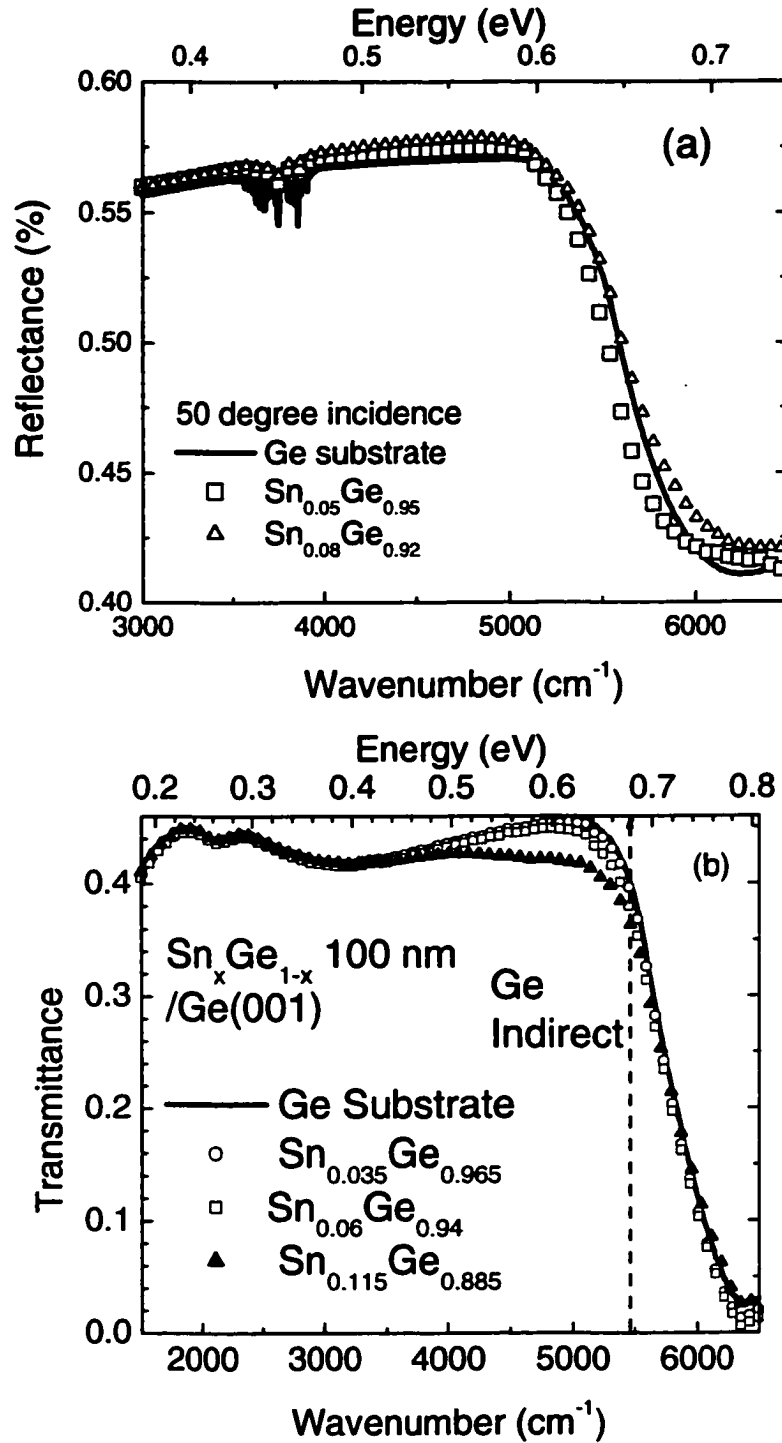


Figure 3.8: FTIR spectra of 100 nm thick $\text{Sn}_x\text{Ge}_{1-x}$ alloys on (a) n-type Ge(001) with $x = 0.05$ and 0.08 in reflectance mode at 50° incidence and (b) on p-type Ge(001) with $x = 0.035$, 0.06 , and 0.115 in transmittance mode at normal incidence.

were plotted in Figure 3.9. By fitting the data with a curve that included a bowing parameter, the indirect to direct bandgap transition occurred near $x = 0.09$, in agreement with deformation potential theory calculations and previous measurements.

3.4.2 Comparison between theory and experiment for $\text{Sn}_x\text{Ge}_{1-x}/\text{Ge}(001)$

Figure 3.10 illustrates the decrease in the direct energy gap with increasing strain. The dotted curve is a fit to the measured energy gap (closed triangles) for unstrained $\text{Sn}_x\text{Ge}_{1-x}$ alloys and the solid curve is the result of the deformation potential theory calculation. The closed triangles represent the measured energy gap for coherently strained $\text{Sn}_x\text{Ge}_{1-x}$ films on Ge(001). At $x = 0.08$, the experimentally measured energy gap is 0.55 eV for coherently strained alloys (solid squares) versus 0.549 eV for the strain-relieved alloys; the energy difference is negligible in comparison to the experimental error in the measurements. The uniaxial splitting of the valence band, ΔE_V , was evident in transmittance measurement in that the density of states was reduced to the heavy hole contribution between E_g, Γ and $E_g, \Gamma + \Delta E_V$ to obtain the best fit to the experimental transmittance spectra for $x > 0.07$. In summary, the direct energy bandgap of $\text{Sn}_x\text{Ge}_{1-x}$ alloys decreased primarily through an increase in Sn concentration for this system. The effect of coherency strain on the $\text{Sn}_x\text{Ge}_{1-x}$ alloy

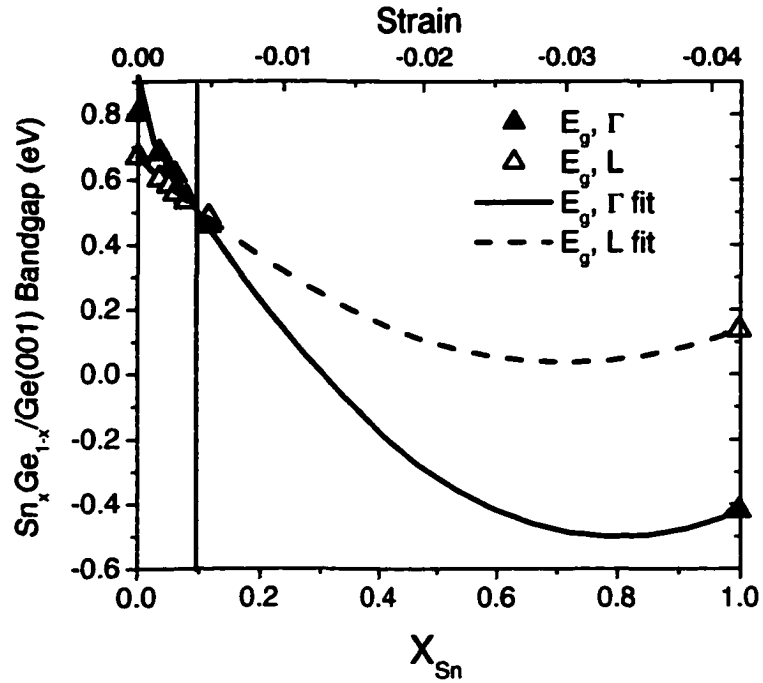


Figure 3.9: Measurement of coherently strained $\text{Sn}_x\text{Ge}_{1-x}/\text{Ge}(001)$ energy bandgap. Closed (open) triangles represent the Γ (L) point.

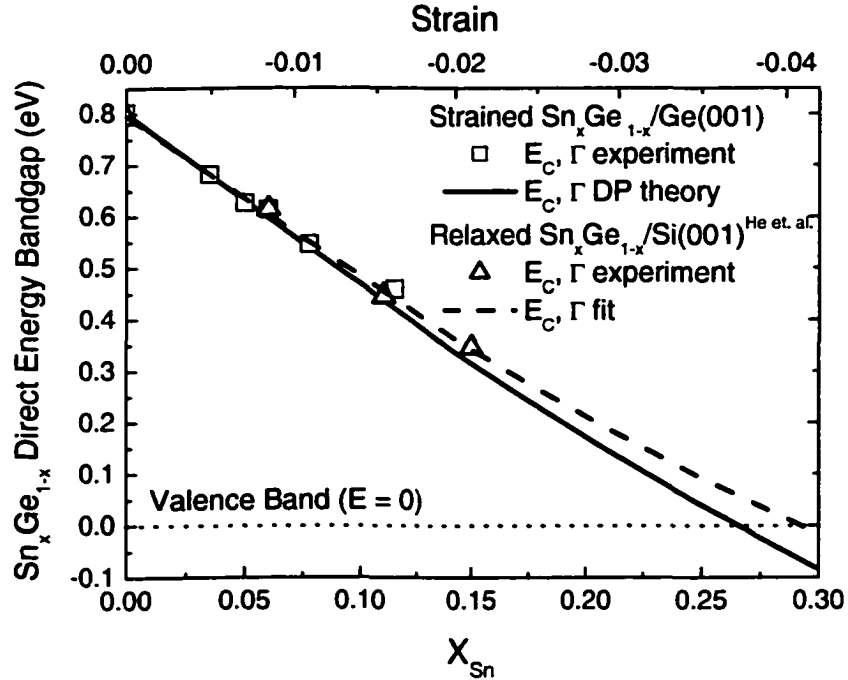


Figure 3.10: Plot of $E_{g, \Gamma}$ for strained (squares) and relaxed [He & Atwater, 1997] (triangles) for $\text{Sn}_x\text{Ge}_{1-x}$ on $\text{Ge}(001)$. The deformation potential theory is represented by a solid line.

bandgap was evident in a reduction in the valence band density of states rather than a reduction of the magnitude of the energy bandgap.

3.5 Conclusion

The experimental relationship between $\text{Sn}_x\text{Ge}_{1-x}/\text{Ge}(001)$ bandgap energy and Sn composition was compared with a deformation potential model that uses an effective mass approximation to determine the perturbation of the electronic structure resulting from coherency strain. For the $\text{Sn}_x\text{Ge}_{1-x}/\text{Ge}(111)$ system, coherency strain was predicted to break the degeneracy of the $\langle 111 \rangle$ conduction band valleys. The energy of the six conduction band valleys oriented off the strain axis decreased dramatically with strain in the calculation while the Γ point increases as a function of coherency strain. Hence $\text{Sn}_x\text{Ge}_{1-x}/\text{Ge}(111)$ was not predicted to undergo an indirect to direct bandgap transition. The deformation potential model predicted that coherency energy had little effect on the overall energy of the $\text{Sn}_x\text{Ge}_{1-x}/\text{Ge}(001)$ bandgap. A reduction in the joint density of states was expected due to the splitting of the degeneracy of the heavy hole and light hole valence bands. For homogeneous, coherently strained $\text{Sn}_x\text{Ge}_{1-x}$ alloys grown on $\text{Ge}(001)$, the measured bandgap energy did not exhibit a measurable change in energy with coherency strain¹⁶ in agreement with deformation potential theory.¹² The decrease in the density of states due to the splitting of the heavy hole and light hole valence band was measurable for alloys with Sn compositions above $x = 0.07$.

3.6 Bibliography

1. D. W. Jenkins and J. D. Dow, *Phys. Rev. B* 36, 7994 (1987)
2. K. A. Mader, A. Baldereschi, and H. von Kanel, *Solid State Comm.* 69, 1123 (1989)
3. A. Harwit, P. R. Pukite, J. Angilello, and S. S. Iyer, *Thin Solid Films* 184, 395 (1990)
4. D. Munzar and N. E. Christensen, *Phys. Rev. B* 49, 11238 (1994)
5. G. He and H. A. Atwater, *Phys. Rev. Lett.* 79, 1937 (1997)
6. B. Bouhafs, F. Benkabou, M. Ferhat, B. Khelifa, J. P. Dufour, and H. Aourag, *Infrared Phys. & Tech.* 36, 967 (1995)
7. H. A. Atwater, G. He, and K. Saipetch, *Mat. Res. Soc. Symp. Proc.* 355, 123 (1995)
8. J. Bardeen and W. Shockley, *Phys. Rev.* 80, 72 (1950)
9. R. People, *Phys. Rev. B* 32, 1405 (1985)
10. Q. M. Ma, K. L. Wang, and J. N. Schulman, *Phys. Rev. B* 47, 1936 (1993)
11. R. A. Soref and L. Friedman, *Superlattices Microstruct.* 14, 189 (1993)
12. R. Ragan, K. S. Min, and H. A. Atwater, *Mat. Sci. Eng. B* 87, 204 (2001)
13. H. M. James, *Phys. Rev.* 76, 1602 (1949)
14. J. C. Slater, *Phys. Rev.* 76, 1592 (1949)
15. S. Peckar, *J. Phys. USSR* 10, 431 (1946)
16. R. Ragan and H. A. Atwater, *Appl. Phys. Lett.* 77, 3418 (2000)
17. H. Hasegawa, *Phys. Rev.* 129, 1029 (1963)
18. F. J. Pollak and M. Cardona, *Phys. Rev.* 172 (1968)
19. C. Herring and E. Vogt, *Phys. Rev.* 101, 944 (1956)
20. N. L. Kang, J. Y. Ryu, and S. D. Choi, *J. Phys. Soc. Jpn.* 67, 2439 (1998)
21. G. E. Kimball, *J. Chem. Phys.* 3, 560 (1935)

22. G. E. Pikus and G. L. Bir, *Sov. Phys. Solid State* **1**, 1502 (1960)
23. A. Iribarren, R. Castro-Rodríguez, V. Sosa, and J. L. Peña, *Phys. Rev. B* **58**, 1907 (1998)

Chapter 4 Non-Lithographic Epitaxial

Sn_xGe_{1-x} Dense Nanowire

Arrays on Ge(001)

4.1 Introduction

4.1.1 Motivation

Self-assembled nanostructures have the advantage of small feature sizes without costly electron beam or extreme UV lithography. A wide variety of methods are employed to fabricate self-assembled structures. DNA templating may be used to pattern gold nanowires and nanospheres,¹ the Langmuir-Blodgett technique can produce self-assembled monolayers of molecules,^{2,3} and various epitaxial growth techniques produce quantum dots and wires. The epitaxial growth techniques are further developed than the former two methods. Epitaxial growth of quantum wires can be achieved along step edges,^{4,5} and via phase-separation during epitaxial growth.⁶ In order for this to be a viable technology, the diameter of the nanowire and the periodicity of the arrays must be controllable. Uniformity of size and spacing of Ge nanocrystals on Si(001) through strain field interactions has already been demonstrated.⁷ We have

studied the $\text{Sn}_x\text{Ge}_{1-x}$ alloy system that undergoes phase-separation during molecular beam epitaxy and forms nanowire arrays oriented along the [001] growth direction. The $\text{Sn}_x\text{Ge}_{1-x}$ alloy system was used as a model system to gain insight into the physical mechanisms driving phase-separation and ordering during dynamic growth. This chapter will be composed of three parts: (1) characterization of the microstructure, (2) statistical analysis of the periodicity of the growth instability and correlation with a physical model, and (3) optical characterization of phase-separated $\text{Sn}_x\text{Ge}_{1-x}/\text{Ge}(001)$ alloy films.

4.1.2 Microstructure analysis

Sn segregates via surface diffusion to the crest of a surface undulation during growth and forms Sn-enriched $\text{Sn}_x\text{Ge}_{1-x}$ rods oriented along [001]. Z-contrast imaging⁸ with scanning transmission electron microscopy (STEM) in planar view was employed to demonstrate Sn phase-separation across the film surface. Transmission electron microscopy (TEM) analysis of 0.1 to 1 μm thick $\text{Sn}_x\text{Ge}_{1-x}/\text{Ge}(001)$ epitaxial films with $0 < x < 0.07$ demonstrated that phase-separation of Sn along the [001] growth direction occurred once a critical film thickness was exceeded. The absence of compositional non-uniformities in the thinner $\text{Sn}_x\text{Ge}_{1-x}$ alloy films was in agreement with the concept of a kinetic critical thickness.⁹ The measured period of phase-separation in TEM was 65 nm and the size of the Sn-rich rods was 23 nm for a film thickness of 1 μm and a Sn

composition of 3%. The period of the phase-separation was observed to be a function of Sn composition.

4.1.3 Statistical analysis and comparison with theoretical models

A height modulation on the surface, corresponding to the phase-separation, or growth instability, was measured in atomic force microscopy (AFM) for a variety of samples with varying misfit strain and Sn composition. The Fourier height correlation function of the AFM topological images yielded a value for the fastest growing wavelength of the growth instability. The experimentally determined fastest growing wavelength was compared with a thermodynamic and kinetic model to investigate the origins of the growth instability. Both models correctly predicted the experimentally observed decrease of the instability wavelength with composition and strain. The thermodynamic model was off by approximately an order of magnitude in its prediction of the period of the instability. The kinetic model and the experimentally measured instability wavelength agreed within a maximum deviation between experiment and theory of 30%. The greater accuracy of the kinetic model was attributed to the relevant couplings of the surface dynamics with compositional and misfit stresses during growth of the binary alloy.

4.1.4 Optical characterization

The optical properties of phase-separated $\text{Sn}_x\text{Ge}_{1-x}$ films, with $x = 0.05, 0.07, 0.085$, were characterized with Fourier transform infrared (FT-IR) spectroscopy. The direct energy bandgap of phase-separated $\text{Sn}_x\text{Ge}_{1-x}$ alloys films decreased with respect to homogeneous alloy films with the same average Sn composition. The decrease in the direct energy bandgap for phase-separated $\text{Sn}_x\text{Ge}_{1-x}$ films was attributed to local Sn-rich regions having a lower bandgap energy. Previous measurements of the $\text{Sn}_x\text{Ge}_{1-x}$ bandgap as a function of alloy composition has demonstrated that the direct energy bandgap decreases with increasing Sn composition.^{10,11} Due to challenges associated with Sn incorporation into the Ge lattice, the phase-separation can be exploited to obtain a direct energy bandgap material with a lower average Sn composition than homogeneous $\text{Sn}_x\text{Ge}_{1-x}$ films and thereby, a lower misfit with respect to the Ge(001) substrate.

4.2 $\text{Sn}_x\text{Ge}_{1-x}$ microstructure

The microstructure of the $\text{Sn}_x\text{Ge}_{1-x}$ films was characterized with Rutherford backscattering spectroscopy (RBS), Raman spectroscopy, TEM, STEM, and AFM. RBS measured the average Sn composition in the film. In Raman spectroscopy, the vibrational energy levels of the optical phonons were measured and evidence of Sn clustering in thicker alloy films was observed.

TEM characterized the crystal structure and STEM analysis in planar view revealed the phase-separation of Sn in a rod like morphology.

4.2.1 Rutherford backscattering spectroscopy

RBS probed the average composition of the $\text{Sn}_x\text{Ge}_{1-x}$ alloy films and indicated the absence of Sn surface segregation during growth. The back-scattered signal was measured with the samples tilted 7° to the incident 2 MeV He^{++} beam to avoid channeling. The spot size of the He^{++} beam was on the order of 1 mm while the phase-separated regions were on a much smaller length scale, on the order of 10 nm. Thus the average Sn composition in the $\text{Sn}_x\text{Ge}_{1-x}$ alloy film was determined from RBS.

4.2.2 Raman spectroscopy

The vibrational energy levels in the crystal were measured via Raman spectroscopy. The Raman shift was measured from the backscattered radiation of an incident 514.5 nm Ar^+ ion laser, at normal incidence to the film, horizontal polarization and at room temperature. The Stokes shifted peak (ω_s) measured the phonon energy ($\hbar\omega_o$):

$$\hbar\omega_s = \hbar\omega_i - \hbar\omega_o \quad (24)$$

where $\hbar\omega_i$ is the incident energy of the Ar^+ ion laser. The phonon energy measures the energy of the vibrational states and, thus, can be an indication of Sn clustering in the alloy.

The first-order Raman peak, $\nu_{\text{LTO}}(\Gamma_{25'})$, for Ge measured the zone-center ($\vec{k} = 0$), triply degenerate, optical phonons and was found near 300 cm^{-1} , shown in Figure 4-1(a). Biaxial strain is known to split the degeneracy of the optical phonons into a doublet (ω_d) and a singlet state (ω_s).¹² The shift of the $\nu_{\text{LTO}}(\Gamma_{25'})$ phonon energy with respect to the Ge bulk $\nu_{\text{LTO}}(\Gamma_{25'})$ peak due to biaxial strain is given by

$$\Delta\omega_d = -3\omega_0\gamma_0\varepsilon_{xx} + \frac{q}{2\omega_0}(\varepsilon_{zz} - \varepsilon_{xx}) \quad (25)$$

$$\Delta\omega_s = -3\omega_0\gamma_0\varepsilon_{xx} + \frac{p}{2\omega_0}(\varepsilon_{zz} - \varepsilon_{xx}) \quad (26)$$

where γ_0 is the Grüneisen parameter (0.893) associated with hydrostatic pressure and p ($-4.7 \times 10^{27} \text{ s}^{-2}$) and q ($-6.2 \times 10^{27} \text{ s}^{-2}$) are parameters associated with uniaxial stress. The $\nu_{\text{LTO}}(\Gamma_{25'})$ peak for thin, homogeneous $\text{Sn}_x\text{Ge}_{1-x}$ films shifted to lower energy with increasing Sn composition, as seen in Figure 4-1(a). The experimentally measured shift of the $\nu_{\text{LTO}}(\Gamma_{25'})$ peak with respect to the Ge $\nu_{\text{LTO}}(\Gamma_{25'})$ peak was approximately four times larger than the value calculated for $\Delta\omega_d$ using equation (25). The values of all the parameters used in the calculation of $\Delta\omega_d$ corresponded to pure Ge. Alloying can also shift the Raman peak due to a softening of the elastic constants. The elastic compliance constants are lower for

Sn than Ge.¹³ The $\nu_{\text{LTO}}(\Gamma_{25'})$ peak for thick $\text{Sn}_x\text{Ge}_{1-x}$ films is seen in Figure 4-1(b). Comparing the Raman spectra of the thin, homogeneous films with the thick films, the shift of the $\nu_{\text{LTO}}(\Gamma_{25'})$ peak with respect to bulk Ge is higher for thicker films with the same average Sn composition. The increase in the peak shift with increasing film thickness may be attributed to an increase in strain on a local scale due to compositional fluctuations as well as to an alloy effect. Sn atoms have a larger atomic radii in comparison to Ge, thus clustering of Sn will distort and strain the crystal lattice.

Further evidence for clustering of Sn atoms in the thick films was seen as an increase in intensity of the Sn $\nu_{\text{LTO}}(\Gamma_{25})$ peak that is found in bulk α -Sn near 200 cm^{-1} . The Raman spectra for thin films and thick films are shown in Figure 4-2(a) and Figure 4-2(b), respectively. For thin $\text{Sn}_x\text{Ge}_{1-x}$ films, the Ge $\omega_{2\text{TA}}(x)$ peak that is found near 160 cm^{-1} decayed and a new peak was formed near 190 cm^{-1} as the Sn composition in the film increased. The peak near 190 cm^{-1} was attributed to a strain shifted $\nu_{\text{LTO}}(\Gamma_{25})$ peak for Sn. The thick films exhibited the same behavior as the thin films. Yet, upon comparison of Figure 4-2(a) and Figure 4-2(b), the relative intensity of the $\nu_{\text{LTO}}(\Gamma_{25})$ peak for Sn with respect to the Ge $\omega_{2\text{TA}}(x)$ peak was much higher in the thick versus thin $\text{Sn}_x\text{Ge}_{1-x}$ films. The increased intensity of the Sn $\nu_{\text{LTO}}(\Gamma_{25})$ peak with film thickness at a fixed average Sn composition indicated that phase-separation occurred when the film thickness exceeded a critical value.

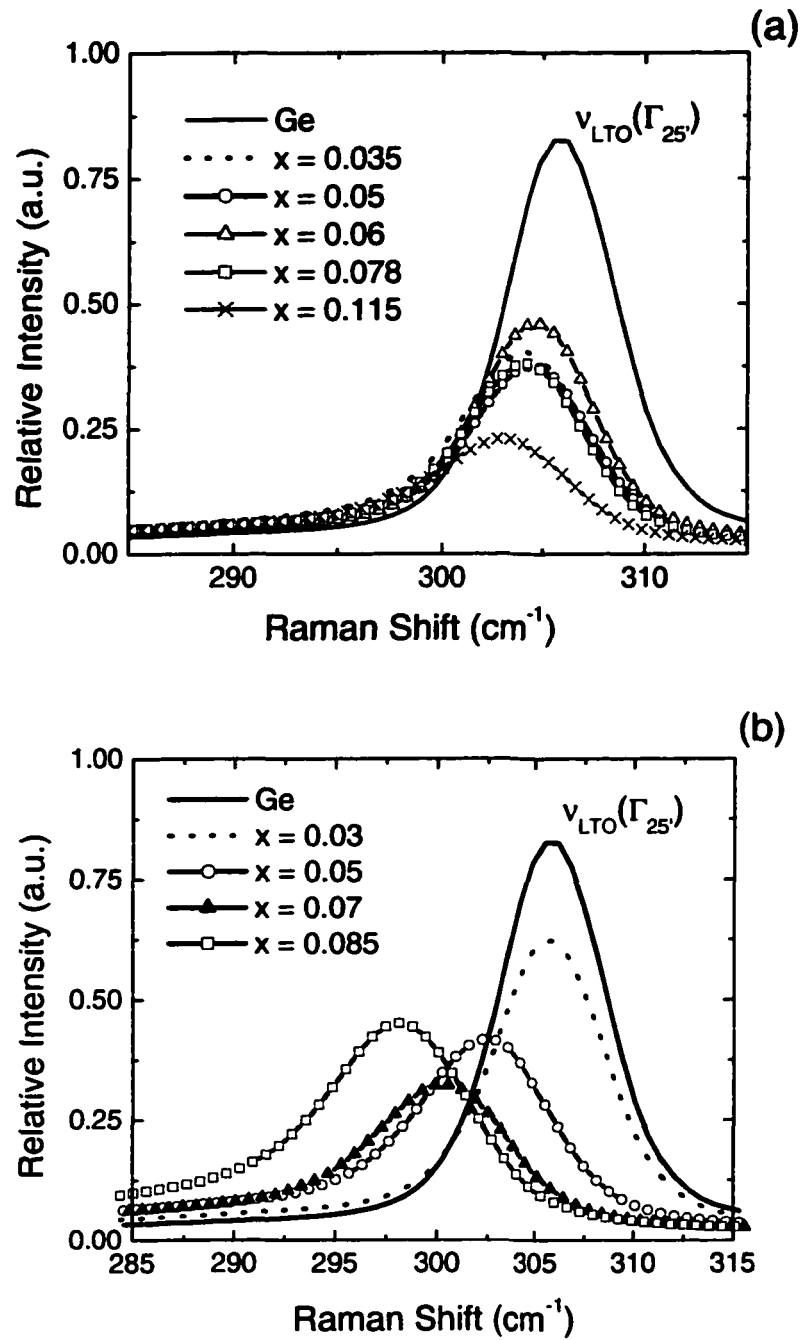


Figure 4-1: Raman shift of zone center optical phonons for (a) 100 nm thick $\text{Sn}_x\text{Ge}_{1-x}$ alloys and (b) 1 μm thick $\text{Sn}_x\text{Ge}_{1-x}$ alloys.

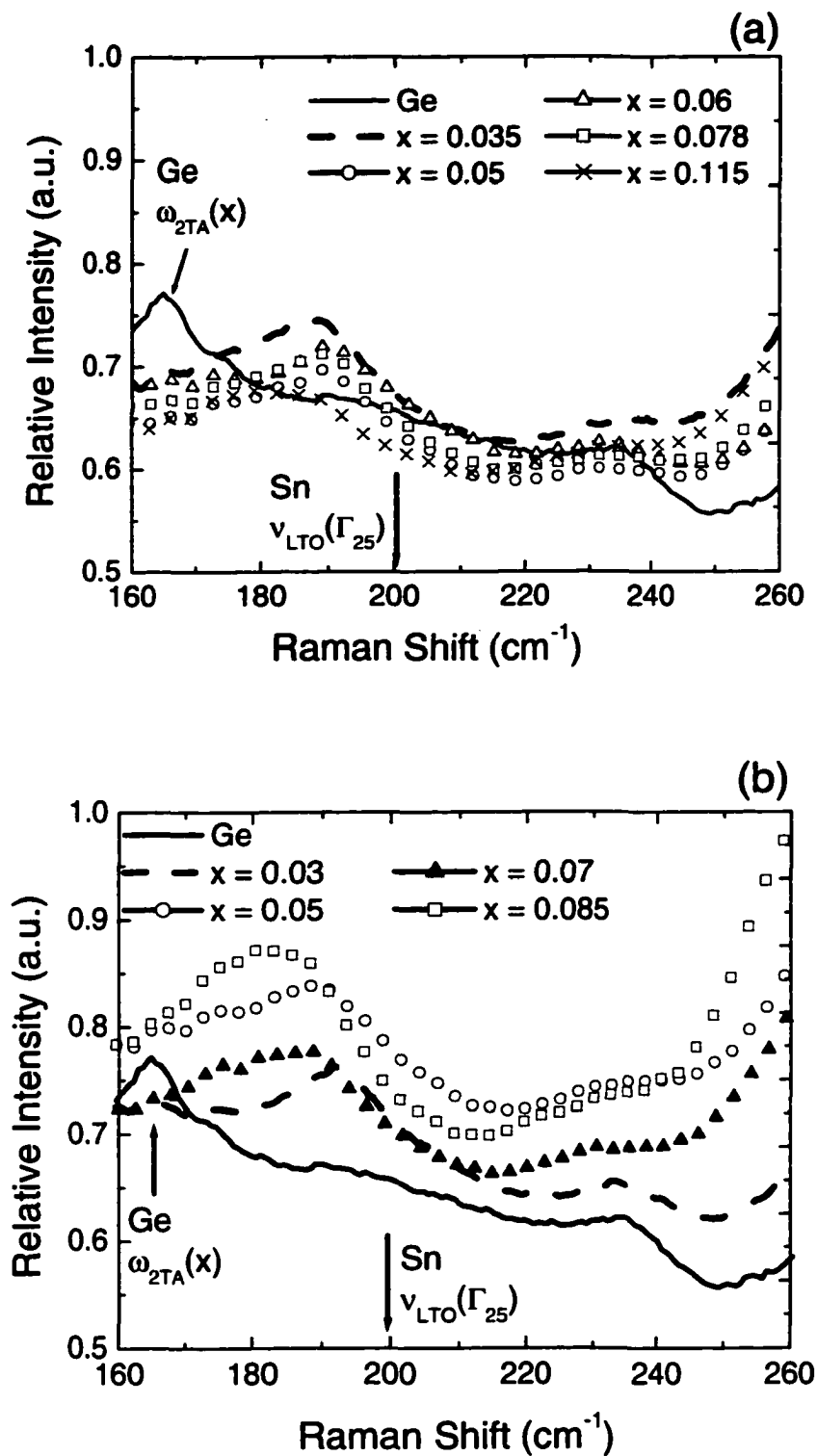


Figure 4-2: Raman spectra of Ge $\omega_{2TA}(x)$ and Sn $\nu_{LTO}(\Gamma_{25})$ peaks for (a) 100 nm thick $\text{Sn}_x\text{Ge}_{1-x}$ alloys and (b) 1 μm thick $\text{Sn}_x\text{Ge}_{1-x}$ alloys.

4.2.3 Transmission electron microscopy analysis

$\text{Sn}_x\text{Ge}_{1-x}/\text{Ge}(001)$ films with Sn composition of $0 < x < 0.07$ and film thickness between 0.1 and 1 μm were examined in TEM. Previously, homogeneous 100 nm thick $\text{Sn}_x\text{Ge}_{1-x}$ films with Sn compositions between $0 < x < 0.115$ were grown coherently on Ge(001) substrates.¹⁰ A significant change in morphology occurred when the $\text{Sn}_x\text{Ge}_{1-x}$ film thickness increased. A cross-sectional TEM image down the [110] zone axis of a 1 μm thick $\text{Sn}_{0.03}\text{Ge}_{0.97}$ ³ film is seen in Figure 4-3(a). The $\text{Sn}_x\text{Ge}_{1-x}$ film has dark and light bands along the [001] growth direction. A cross-section orthogonal to [110] was prepared and similarly imaged down the $[\bar{1}\bar{1}0]$ zone axis, shown in Figure 4-3(b). The contrast observed down the $[\bar{1}\bar{1}0]$ zone axis had approximately the same periodicity as that observed down the [110] zone axis. The schematic depicted in Figure 4-4 portrays the assumption that the contrast in the images down the [110] and $[\bar{1}\bar{1}0]$ zone axes can be interpreted as Sn-rich rods growing along [001]. Although, further substantiation of the claim of Sn phase-separation is still necessary because contrast observed in TEM is a function of both composition and strain.

In order to determine if the contrast was due to grain boundaries, diffraction patterns were taken down the [001] and [110] zone axes, seen in

³ From here on when using this convention ($\text{Sn}_x\text{Ge}_{1-x}$), x will denote the average film composition.

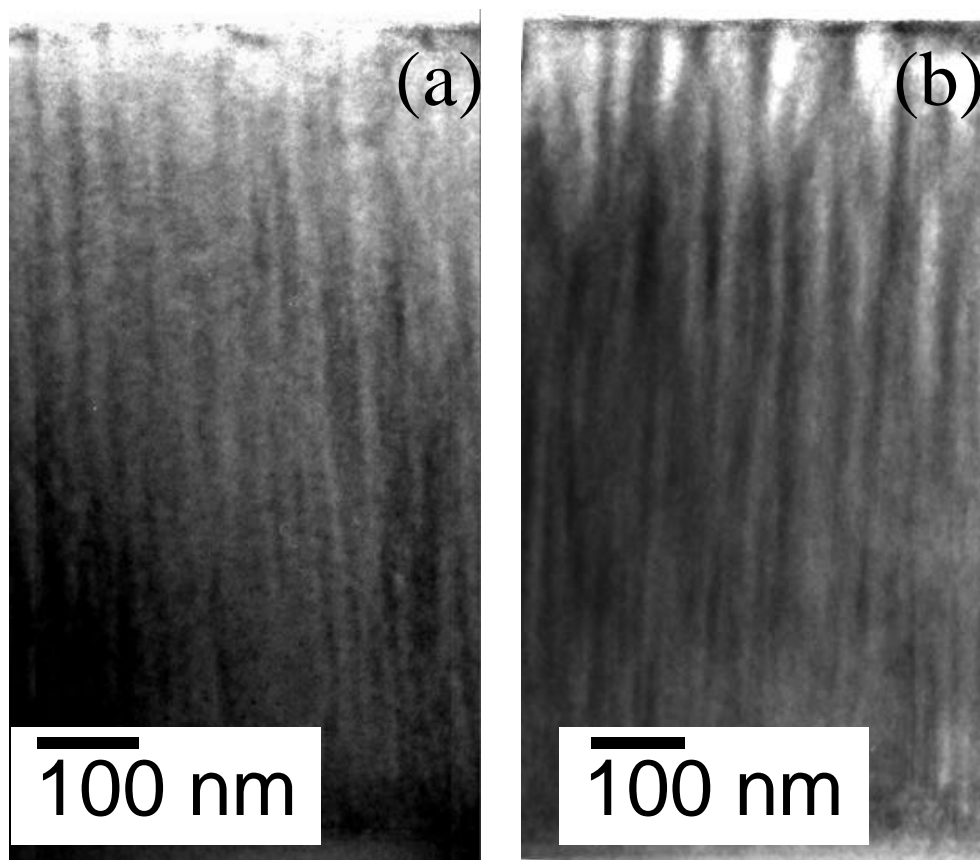


Figure 4-3: Cross-sectional TEM images of $\text{Sn}_x\text{Ge}_{1-x}$ alloy with an average Sn composition of 0.03 imaged down the (a) $[110]$ zone axis and (b) $[\bar{1}10]$ zone axis.

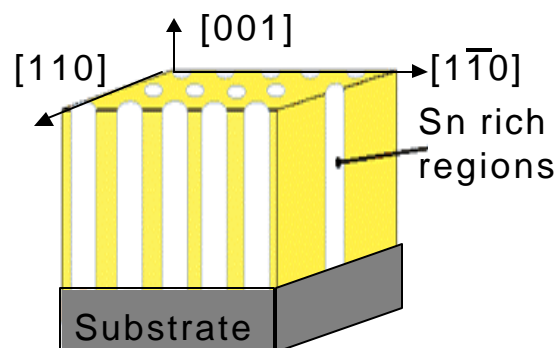


Figure 4-4: Schematic representing Sn-enrichment of $\text{Sn}_x\text{Ge}_{1-x}$ rods along $[001]$.

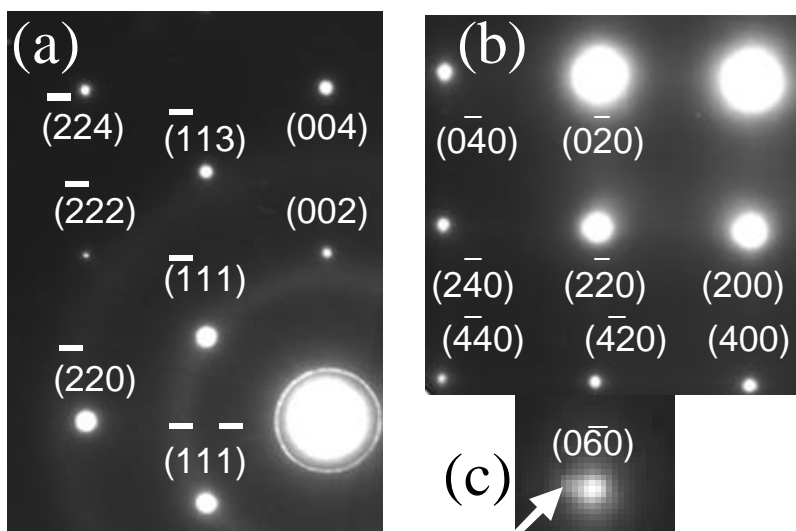


Figure 4-5: $\text{Sn}_{0.03}\text{Ge}_{0.97}$ diffraction patterns taken along the (a) $[110]$ and (b) $[001]$ zone axes. In (c) the $(0\bar{6}0)$ reflection is enlarged. Arrow points to additional diffraction spot on the left.

Figure 4-5. The diffraction patterns of the $\text{Sn}_{0.03}\text{Ge}_{0.97}$ film were characteristic of a single crystal. Hence the contrast observed was not due to grain boundaries.⁴

Upon further examination of the $[001]$ diffraction pattern, an additional diffraction spot was observed to the left of the $(0\bar{6}0)$ diffraction spot along the $[0\bar{1}0]$ direction, seen in Figure 4-5(c). If phase-separation of Sn and Ge is occurring, elastic distortion of the matrix resulting from clustering of the larger Sn atoms can give rise to a displacement or streaking of the diffraction spot parallel to the distortion.¹⁴ If the distortion is small, the primary diffraction spot

⁴ The polycrystalline ring seen in the $[110]$ diffraction pattern for the $\langle 111 \rangle$ reflections, Figure 4-5(a), is a sample preparation artifact originating from ion milling during the thinning process. In the $[001]$ diffraction pattern for the same sample, a polycrystalline ring is not observed.

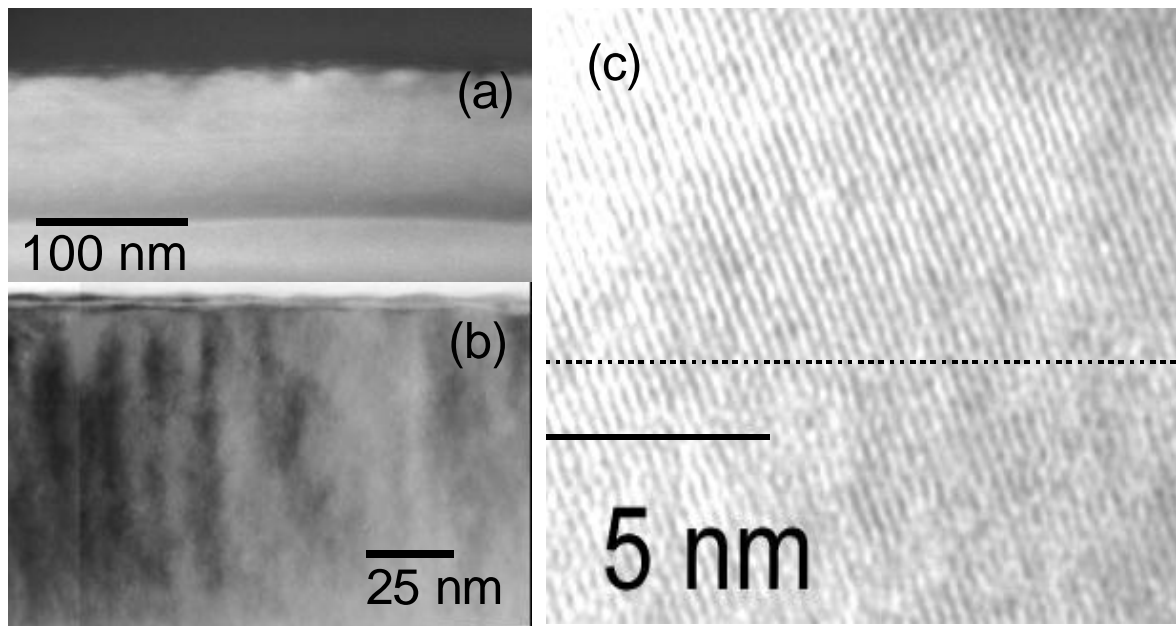


Figure 4-6: $\text{Sn}_{0.06}\text{Ge}_{0.94}/\text{Ge}(001)$ TEM images under 2 beam conditions with (a) $\bar{g} = (004)$ and (b) $\bar{g} = [\bar{1}\bar{1}1]$. (c) HR-TEM image where the dashed line represents the interface.

and the spot due to the crystal distortion are distinguishable only at large values in reciprocal space. Therefore the streaking of the $(0\bar{6}0)$ diffraction spot indicated that Sn may be segregating along (010) planes.

In order to determine if the contrast observed in the TEM images was associated with defects, a 100 nm coherently strained $\text{Sn}_{0.06}\text{Ge}_{0.94}$ film was analyzed under different 2 beam conditions. When $\bar{g} = [004]$, shown in Figure 4-6(a), the thin film exhibited contrast near surface undulations but bands of contrast were not seen parallel to $[001]$. When $\bar{g} = [\bar{1}\bar{1}1]$, faint contrast in the shape of rods along the growth direction was observed, seen in Figure 4-6(b),

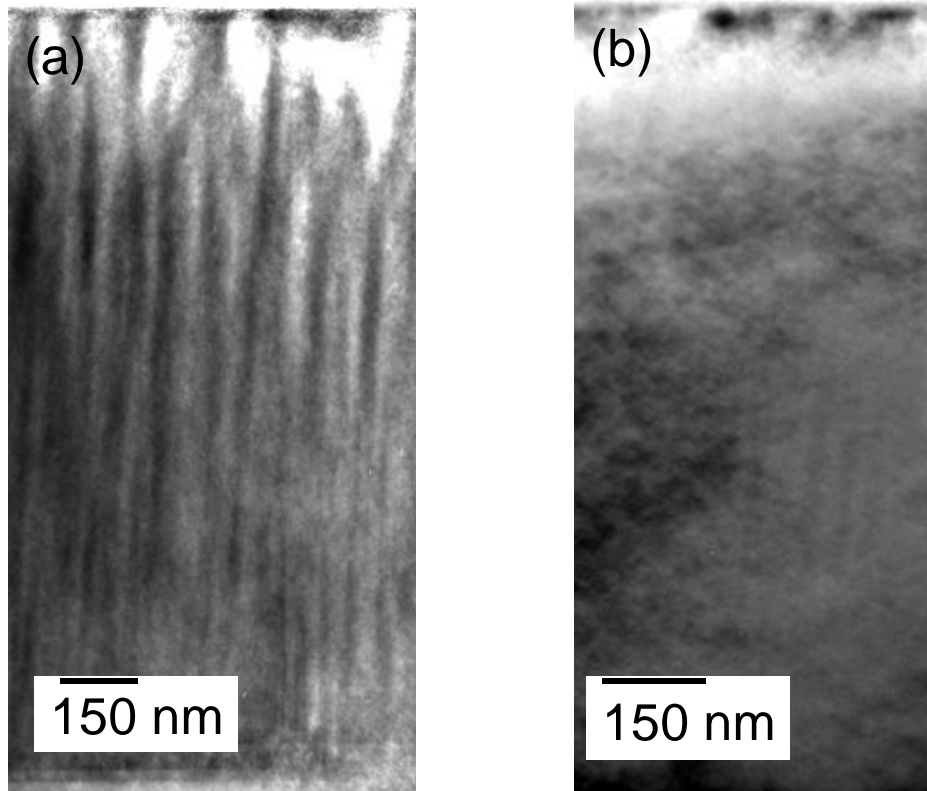


Figure 4-7: TEM images of 1 μm thick $\text{Sn}_{0.03}\text{Ge}_{0.97}$ film imaged under 2 beam conditions (a) $\vec{g} = [2\bar{2}0]$ and (b) $\vec{g} = [004]$.

for this $\text{Sn}_{0.06}\text{Ge}_{0.94}$ film. A high resolution TEM image of the $\text{Sn}_{0.06}\text{Ge}_{0.94}$ film taken along the $[110]$ zone axis had continuous lattice fringes at the film-substrate interface, Figure 4-6(c). Thus the contrast observed when $\vec{g} = [111]$ was not attributable to defects. The strain observed in the $\vec{g} = [\bar{1}\bar{1}1]$ 2 beam image has been identified as a possible driving force for phase-separation.^{15,16}

The $\text{Sn}_{0.03}\text{Ge}_{0.97}$ film was imaged under various 2 beam conditions to probe the strain state of the film. Imaging under 2 beam conditions enhances the strain

contrast associated with the set of crystallographic planes excited⁵ by the incident beam. TEM images of the Sn_{0.03}Ge_{0.97} film imaged under $\bar{g} = [004]$ and $\bar{g} = [\bar{2}20]$ 2 beam conditions are shown in Figure 4-7(b) and Figure 4-7(a), respectively. When imaged under $\bar{g} = [004]$ 2 beam conditions, the dark bands were still visible but much less contrast was observed in comparison to the $\bar{g} = [\bar{2}20]$ image. The reduction in contrast can be understood by analyzing the kinematical equation for the diffracted intensity, $|\Psi_g|^2$, under 2 beam conditions.¹⁷

$$|\Psi_g|^2 = \frac{\Psi_0}{\zeta_g} \int_{-\frac{t}{2}}^{\frac{t}{2}} e^{2\pi i(sz - \bar{g} \cdot \delta\vec{r})} dz \quad (27)$$

where $\delta\vec{r}$ is the distortion of the lattice, ζ_g is the extinction distance and Ψ_0 is the incident intensity. The strain contrast arises from the $\bar{g} \cdot \delta\vec{r}$ term in the exponential of equation (27). If Sn segregates along (100) and (010) planes, the larger Sn atoms can coherently distort the lattice and $\delta\vec{r} = [100]$ and $[010]$. Then contrast should be dominated by composition when $\bar{g} = [004]$ because $\delta\vec{r}$ and \bar{g} are orthogonal. Similar contrast is seen in GP zones in the Cu-Al system where Cu precipitates segregate along $\{001\}$. The Cu precipitates are most visible in TEM when the diffracted beam is parallel with the lattice distortion.

⁵ That is, the Bragg condition is satisfied for these planes.

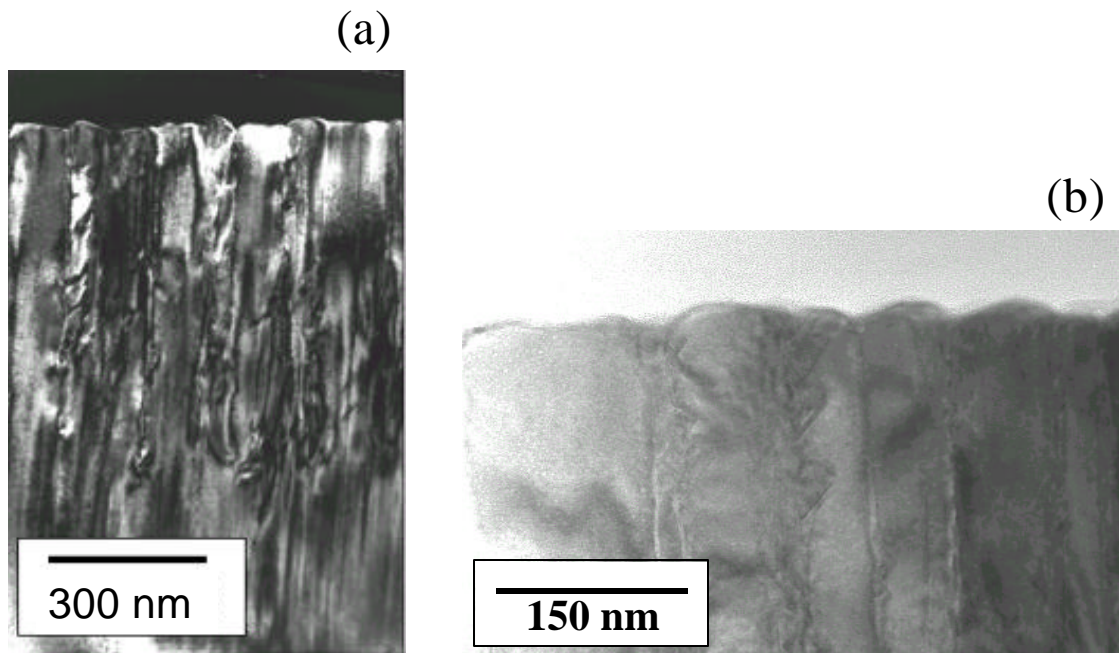


Figure 4-8: Cross-sectional TEM images of 1 μm thick $\text{Sn}_{0.07}\text{Ge}_{0.93}/\text{Ge}$ (100) with (a) $\bar{g} = [2\bar{2}0]$ and (b) $\bar{g} = [004]$.

Additionally, the period of the contrast was observed to decrease with increasing Sn composition. The period was measured as 65 nm and the dark regions were measured as 23 nm in diameter for the $\text{Sn}_{0.03}\text{Ge}_{0.97}$ film in the image taken under $\bar{g} = [2\bar{2}0]$ 2 beam conditions, seen in Figure 4-7(a). As the average Sn composition was increased to $x = 0.07$, the period of the contrast decreased to 30 nm as seen in the $\bar{g} = [2\bar{2}0]$ image of Figure 4-8(a). In this image, dislocations and stacking faults were present in addition to deep cusps at the surface. In Figure 4-8(b), the cusps are more visible. The formation of deep cusp-like morphologies during growth has been associated with chemical potential gradients along the surface.¹⁸

4.2.4 Scanning transmission electron microscopy

In general, the contrast seen in conventional TEM mode is a convolution of strain and composition. Using scanning transmission electron microscopy (STEM) with an annular detector to include wide angle scattered electrons ($\alpha > 80$ mrad) and to exclude the transmitted and diffracted beams, the contrast is then due to composition.⁸ The diffracted intensity is attenuated at large angles; therefore, the intensity observed at large angles is primarily composed of elastically scattered electrons. The elastic cross-section depends on the atomic number, yielding composition or Z-contrast. The atomic number of Sn is 50 and that of Ge is 32; thus, measurable Z-contrast was expected.

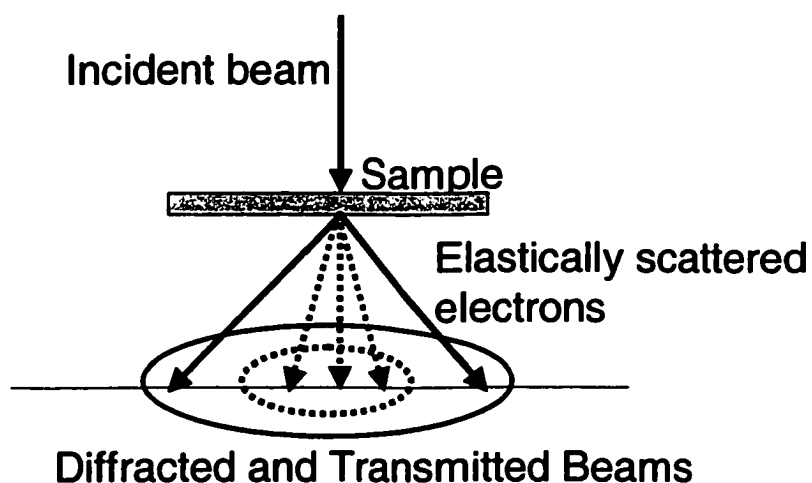


Figure 4-9: Schematic of STEM experiment with annular detector to image elastically scattered electrons and to exclude diffracted and transmitted beams.

The spot size of the electron beam in scanning mode was 5 nm. When the $\text{Sn}_x\text{Ge}_{1-x}$ samples were prepared in cross-section it was not possible to see composition contrast with the annular detector. The Sn-rich rods were on the order of 20 nm in diameter and the specimen thickness was approximately 100 nm.⁶ Thus, electrons penetrating the 100 nm thick specimen sampled Sn-rich and Ge-rich regions, yielding the average composition of the sample. Before showing the STEM results for the thick films, the homogeneity of a 100 nm thick $\text{Sn}_{0.06}\text{Ge}_{0.94}$ film prepared in planar view using STEM with the annular detector is demonstrated in Figure 4-10. Although variations in contrast were observable, the variations were not periodic and were on a different length scale than observed in the TEM cross-section, Figure 4-6. The difference in contrast in the planar view image of this film was attributed to thickness variations across the thinned specimen. Thus, the STEM image demonstrated the compositional uniformity of the 100 nm thick $\text{Sn}_{0.06}\text{Ge}_{0.97}$ film. The results of the STEM analysis were quite different for a 1 μm thick $\text{Sn}_{0.03}\text{Ge}_{0.97}$ film. In planar view, Figure 4-11(a), the bright field⁷ STEM image of this film consisted of dark circular regions with the same 65 nm periodicity observed in cross-sectional TEM.

⁶ 100 nm refers to the thickness of the sample after thinning for imaging in TEM, not the original sample thickness.

⁷ Bright field imaging in this context refers to the transmitted and diffracted beams contributing to the image.

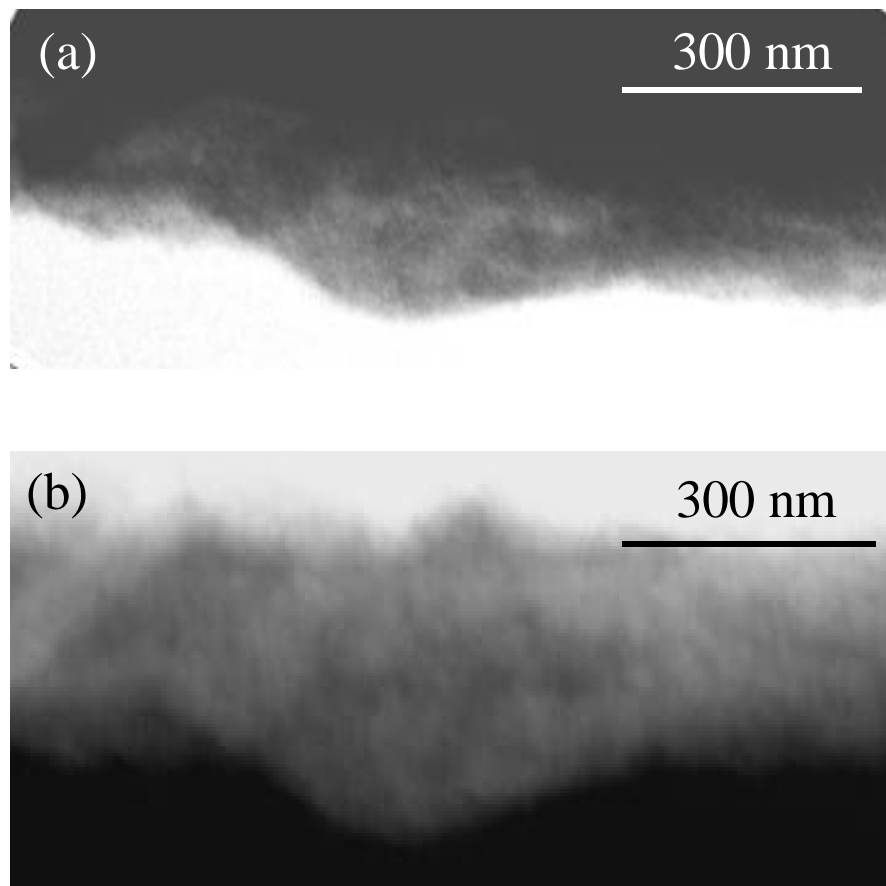


Figure 4-10: STEM analysis of 100 nm thick $\text{Sn}_{0.06}\text{Ge}_{0.94}$ film: (a) Bright field image includes diffracted and transmitted beams and (b) dark field image includes only elastically scattered electrons.

Using the annular detector, Figure 4-11(b), the Sn-rich rods appeared as bright ellipses producing a complementary image to that taken under diffracting conditions, Figure 4-11(a). As expected from the increased elastic cross-section, the Sn-rich rods appeared brighter than Ge due to the higher atomic number of

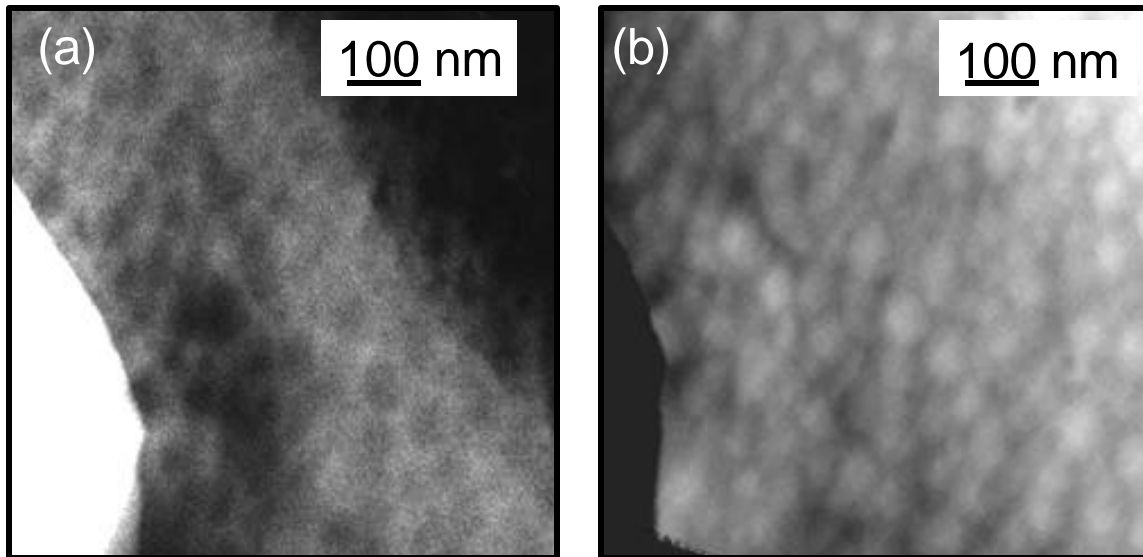


Figure 4-11: STEM images of 1 μm thick $\text{Sn}_{0.03}\text{Ge}_{0.97}$ (a) bright field image with transmitted and diffracted beams and (b) dark field image that includes only elastically scattered electrons.

Sn versus Ge. Thus, Sn is phase separating into rods along the [001] growth direction in the thick $\text{Sn}_x\text{Ge}_{1-x}$ films.

4.3 Theoretical models of growth instabilities versus experiment

A surface undulation observed in AFM was correlated with the phase-separation observed in TEM. AFM measured the periodicity of the surface undulation and Fourier transforms of the AFM images determined the fastest growing wavelength of the growth instability. In order to gain insight into the

origins of phase-separation occurring during growth of the $\text{Sn}_x\text{Ge}_{1-x}$ binary alloy, both a thermodynamic and a kinetic model were compared to the experimentally measured period of the surface undulation, referred to as the growth instability wavelength.

In the thermodynamic model,¹⁵ the free energy difference between a compositionally non-uniform film with an undulated surface (the modulated state) and a homogeneous, planar film (the reference state) was calculated. A characteristic minimum wavelength was defined at the stability boundary where the free enthalpy change between the reference and modulated state was zero. The characteristic wavelength predicted by the thermodynamic model¹⁵ was compared to the experimentally measured fastest growing wavelength as determined from the autocorrelation function of the AFM images. The fastest growing wavelength will be larger than the critical wavelength calculated in the thermodynamic model; yet, the two should scale proportionally. The experimental wavelength exhibited the trends predicted by the thermodynamic model. Yet the absolute value predicted by the thermodynamic model was much larger differing from the experimental value by up to an order of magnitude.

A kinetic model using linear stability analysis predicted a value for the fastest growing wavelength of the growth instability.^{16,19} In this kinetic model, compositional non-uniformities and surface undulations are stress driven as in the thermodynamic model. Unlike the thermodynamic model, mass transport mechanisms, such as surface diffusion and the incoming flux of the beam are

incorporated. These mass transport mechanisms are relevant to molecular beam epitaxial growth. The analysis predicted a value for the fastest growing wavelength that was in better agreement with the values measured experimentally than the thermodynamic model.

4.3.1 Description of the experiment

By varying the effective lattice parameter of the substrate, the dependence of the growth instability on strain and composition was decoupled. The substrate lattice parameter was tuned by MBE growth of thick partially relaxed $\text{Si}_y\text{Ge}_{1-y}$ buffer layers²⁰ on Ge(001) substrates with varying Si composition. The $\text{Sn}_x\text{Ge}_{1-x}$ and $\text{Si}_y\text{Ge}_{1-y}$ films were grown at a fixed growth rate, 0.05 nm/sec, and 0.15 nm/sec, respectively. The details of the $\text{Sn}_x\text{Ge}_{1-x}$ growth were described in detail in Chapter 2. The Si composition of the virtual substrate was varied to obtain a series of films with a constant Sn composition but differing values of misfit with respect to the virtual $\text{Si}_y\text{Ge}_{1-y}$ substrates (Figure 4-12). The misfit was varied from 0 to 1%. Alternatively, in order to probe the effect of composition on the growth instability, $\text{Sn}_x\text{Ge}_{1-x}$ films with the misfit engineered to remain constant were grown in the composition range of $0 < x < 0.035$ for a misfit of approximately 0.5% and in the composition range of $0 < x < 0.07$ for a misfit of approximately 1%. Both the Sn composition in the $\text{Sn}_x\text{Ge}_{1-x}$ films and the Si composition in the $\text{Si}_y\text{Ge}_{1-y}$ buffer layers were varied in order to obtain a series of $\text{Sn}_x\text{Ge}_{1-x}$ films with the same misfit but differing Sn compositions.

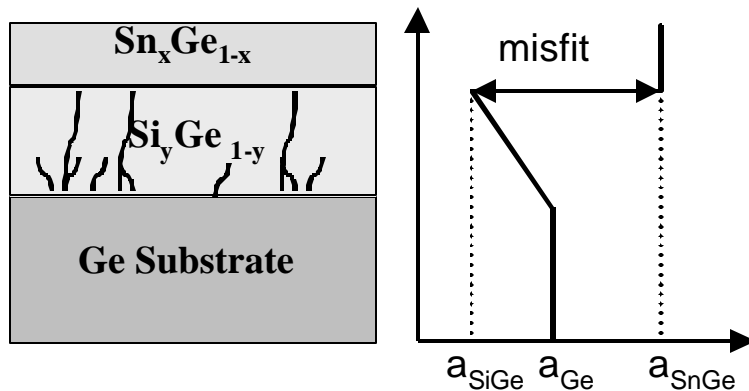


Figure 4-12: Schematic demonstrating how the misfit is tuned independent of Sn composition in the $\text{Sn}_x\text{Ge}_{1-x}$ alloy film by changing the Si composition in the $\text{Si}_y\text{Ge}_{1-y}$ virtual substrate.

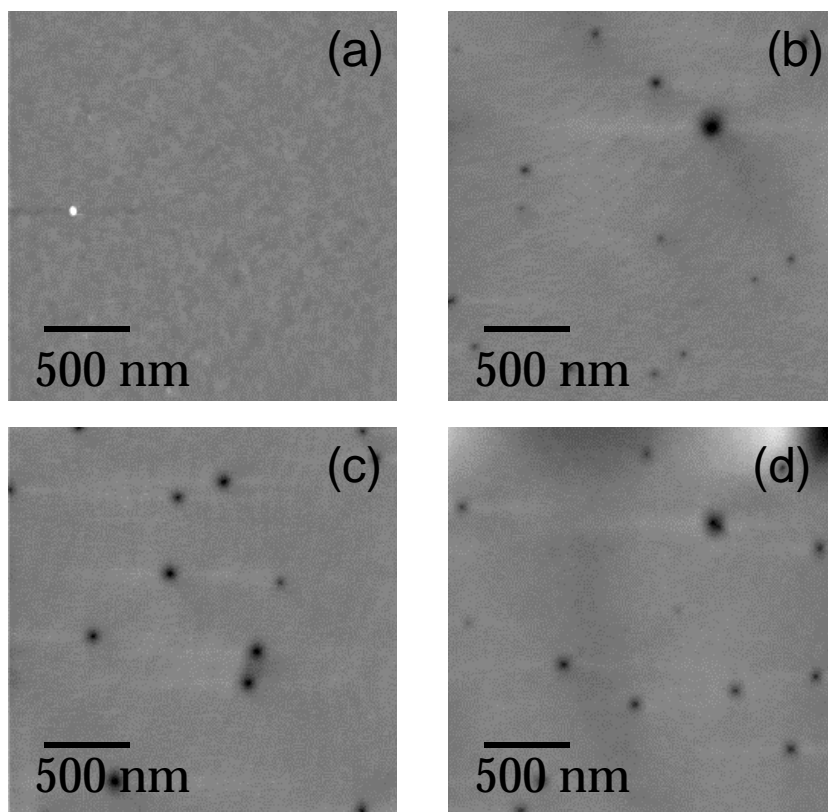


Figure 4-13: AFM images of $\text{Si}_y\text{Ge}_{1-y}$ virtual substrates with Si composition (a) 0 (b) 0.035 (c) 0.06 and (d) 0.15.

The $\text{Si}_y\text{Ge}_{1-y}$ layers were grown at 600 °C with a grading rate of 10%/μm to minimize the dislocation density.²¹ Prior to $\text{Sn}_x\text{Ge}_{1-x}$ growth, the sample was cooled to 160 °C to eliminate Sn surface segregation. Threading dislocations were evident in the $\text{Si}_y\text{Ge}_{1-y}$ films in cross-sectional TEM, Figure 4-15, and AFM, Figure 4-13. The intersection of a threading dislocation with the surface was observed in AFM as a pit. In Figure 4-13, the threading dislocation pit density was imaged as a function of Si content in the $\text{Si}_y\text{Ge}_{1-y}$ virtual substrate for Si compositions between $0 < y < 0.15$. A slight increase in dislocation density with increasing Si composition was observed. X-ray analysis of the $\text{Si}_y\text{Ge}_{1-y}$ virtual substrates indicated that the low Si content alloys, less than 5%, were fully relaxed and the higher Si content alloys were partially relaxed with respect to the Ge(001) substrate. X-ray reciprocal space maps are shown in Figure 4-14 for (004) and (224) reflections of the $\text{Sn}_{0.018}\text{Ge}_{0.982}/\text{Si}_{0.06}\text{Ge}_{0.94}/\text{Ge}(001)$ sample. In (a), the (004) reflection indicated that the $\text{Si}_{0.06}\text{Ge}_{0.94}$ layer was in tension and the $\text{Sn}_{0.018}\text{Ge}_{0.982}$ layer was in compression with respect to the Ge substrate. In (b), the (224) reflection yielded information regarding the state of relaxation of the epitaxial films. The lines are guides to the eye. A $\text{Si}_{0.06}\text{Ge}_{0.94}$ peak falling on the vertical dashed line through the substrate peak represents the fully strained case (each structure has the same in-plane lattice parameter). The intersection of the solid diagonal line and the solid vertical line represents the axis along which the $\text{Si}_{0.06}\text{Ge}_{0.94}$ peak would fall if the layers were fully relaxed. The experimentally observed map showed that the $\text{Si}_{0.06}\text{Ge}_{0.94}$ layer exhibited some relaxation (about

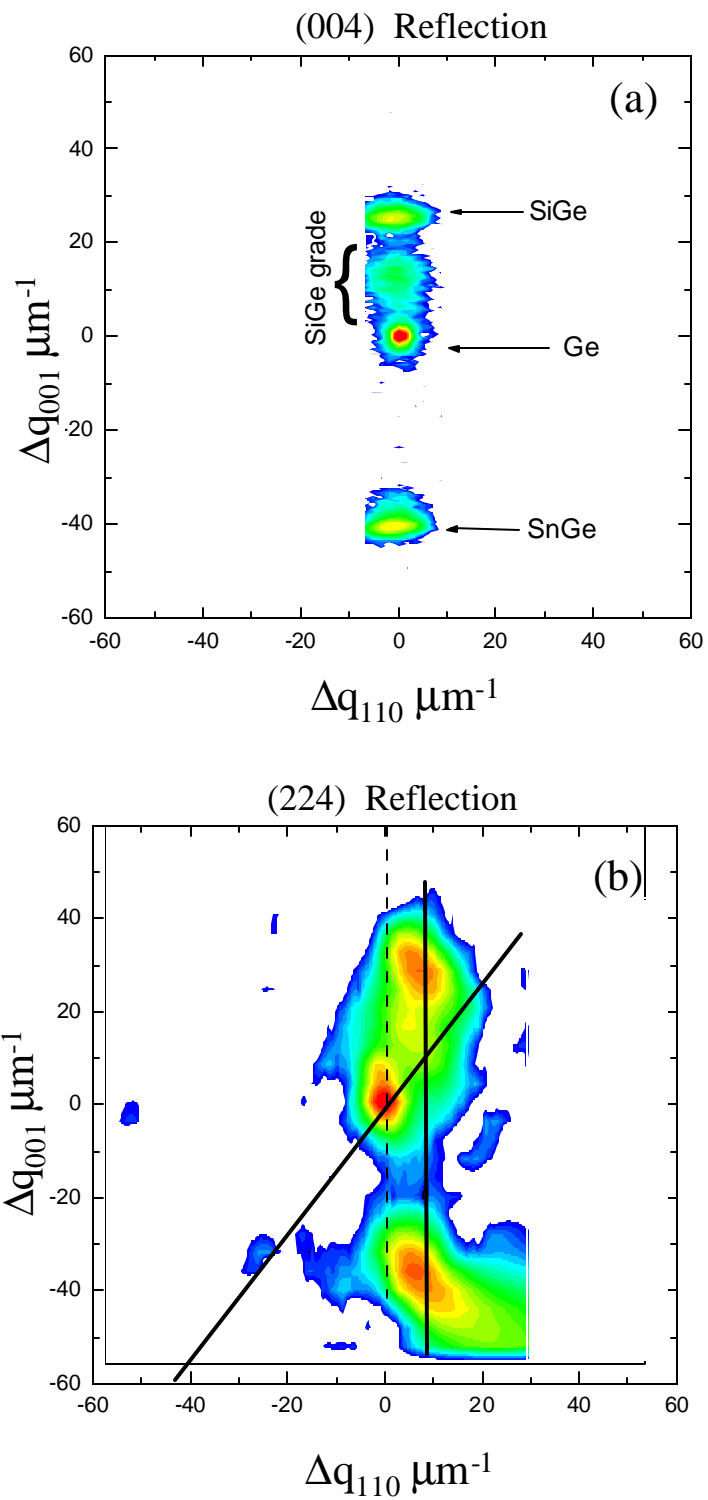


Figure 4-14: Reciprocal X-ray space maps for (a) (004) and (b) (224) reflections of the $\text{Sn}_{0.018}\text{Ge}_{0.982}/\text{Si}_{0.06}\text{Ge}_{0.94}/\text{Ge}(001)$ sample.

25%) with respect to the Ge substrate. In addition, the solid vertical line that passed through the $\text{Si}_{0.06}\text{Ge}_{0.94}$ peak also passed through the $\text{Sn}_{0.018}\text{Ge}_{0.982}$ layer. Hence, the $\text{Sn}_{0.018}\text{Ge}_{0.982}$ layer was pseudomorphic to the $\text{Si}_{0.06}\text{Ge}_{0.94}$ layer

By growing $\text{Sn}_x\text{Ge}_{1-x}$ films on substrates with an increased dislocation density in comparison to the Ge(001) substrates, it was necessary to see if defects dominated the morphology of the films. The period of the growth instability for $\text{Sn}_x\text{Ge}_{1-x}/\text{Ge}(001)$ with $x = 0.03$ and $x = 0.07$ was measured in TEM as 65 nm and 30 nm, respectively. In the planar view AFM images of Figure 4-13, the average spacing between the threading dislocations in the $\text{Si}_y\text{Ge}_{1-y}$ films was approximately 500 nm, much larger than the growth instability wavelengths measured in cross-section TEM. The spacing between threading dislocations was measured as 490 nm in cross-section TEM for $\text{Sn}_{0.018}\text{Ge}_{0.982}/\text{Si}_{0.06}\text{Ge}_{0.94}/\text{Ge}(001)$. The instability wavelength was measured to be 84 nm, Figure 4-15. Thus, the microstructure was not dominated by defects. The final compositions of the $\text{Si}_y\text{Ge}_{1-y}$ virtual substrate and the average composition of the $\text{Sn}_x\text{Ge}_{1-x}$ layers were measured by RBS.

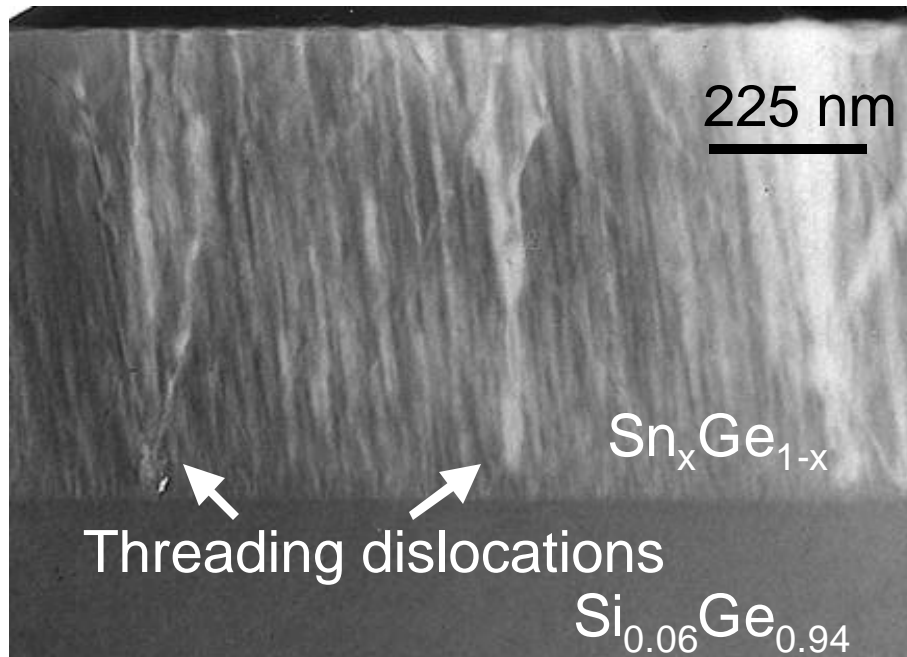


Figure 4-15: TEM image of $\text{Sn}_{0.018}\text{Ge}_{0.982}/\text{Si}_{0.06}\text{Ge}_{0.94}/\text{Ge}(001)$ with $\bar{g} = [2\bar{2}0]$.

4.3.2 Experimental determination of instability wavelength

The period of the surface undulation and the periodicity of the phase-separation observed in TEM were correlated. The surface undulation was measured by AFM and had feature heights measured to be on the order of 2 nm. The observed period of the cusps on the film surface of a 1 μm thick $\text{Sn}_{0.07}\text{Ge}_{0.93}$ film was approximately 150 nm in both AFM, Figure 4-16(a), and TEM, Figure 4-16(b). The shorter wavelength of the growth instability between the cusps was also evident in both imaging techniques and was measured as 30 nm. In the

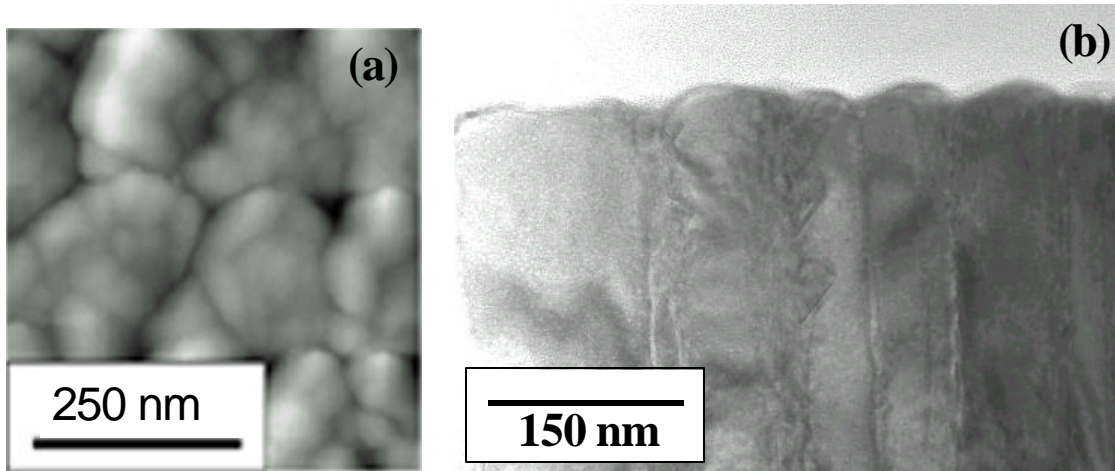


Figure 4-16: Correlation between the measured value of the instability wavelength using (a) AFM surface morphology and (b) TEM cross-section of a 1 μm thick $\text{Sn}_{0.07}\text{Ge}_{0.93}/\text{Ge}$ (001) film. AFM

image with $\text{Ge}/\text{Si}_y\text{Ge}_{1-y}/\text{Ge}(001)$ and a misfit of 0.5%, the surface undulation had facets along [010] and [100], as seen in Figure 4-17(a). Hence, AFM analysis also confirmed that the ordering of the growth instability was oriented along the elastically soft $\langle 100 \rangle$ directions in the plane of the film with the TEM analysis .

The dependence of the instability wavelength on Sn composition and strain was estimated from the AFM images. A $\text{Ge}/\text{Si}_y\text{Ge}_{1-y}/\text{Ge}(001)$ with a misfit of 0.5% is seen in Figure 4-17(a). The $\text{Sn}_x\text{Ge}_{1-x}/\text{Ge}(001)$ film with $x = 0.018$ and misfit of 0.5% is seen in Figure 4-17(b). By comparing the two figures, the increased Sn composition at fixed misfit decreased the instability wavelength. The effect of strain independent of Sn composition can be seen by comparing two $\text{Sn}_x\text{Ge}_{1-x}/\text{Ge}(001)$ films with the same Sn composition ($x = 0.018$) but different values of misfit. The AFM images of the $\text{Sn}_{0.018}\text{Ge}_{0.982}$ with a misfit of 0.26% and with a misfit of 0.5% are shown in Figure 4-18(a) and Figure 4-18(b), respectively.

The instability wavelength decreased with increasing misfit . By comparing the two sets of images, that with constant strain versus that with constant composition, the instability wavelength was more sensitive to composition than strain.

The instability wavelength was determined with greater precision by calculating the autocorrelation function of the 2-dimensional AFM images. The autocorrelation function, $G(k_x, k_y)$, was calculated from the surface topography by

$$G(k_x, k_y) = |\mathfrak{F}(F(x, y))|^2 \quad (28)$$

where $F(x, y)$ is the signal of the AFM topographical image and k_i is the wave vector in the i direction and \mathfrak{F} denotes a Fourier transform. In order to improve statistics of the autocorrelation function, the directional dependence of the wave vector was discarded.

$$G(k) = \sum_{k=\sqrt{k_x^2+k_y^2}} G(k_x, k_y) \quad (29)$$

Plots of the autocorrelation functions, $G(k)$, versus wave vector yielded a quantitative value for the fastest growing wave vector of the instability. The wave vector (k) of the instability was related to the wavelength (λ) by the following relationship:

$$k = 2\pi/\lambda \quad (30)$$

A typical spectrum of $G(k)$ versus k displayed for a Ge/Ge_{0.24}Si_{0.76} film with a misfit of 0.98% had a maxima corresponding to a wavelength of 170 nm. The AFM image from this same Ge/Ge_{0.24}Si_{0.76} film is shown in Figure 4-20. Visual inspection of the AFM image yielded a wavelength on the order of 200 nm and confirmed that the wavelength determined from the autocorrelation function accurately characterized the growth instability.⁸ Statistical noise in the data blurs the peak of $G(k)$. The experimental error involved in determining the fastest growing instability wave vector is shown in Figure 4-21. The maximum and minimum value of the wavelength corresponds to the error in determining the peak of $G(k)$.

The autocorrelation yields more physical information than the fastest growing wavelength. A surface that undergoes random deposition in the absence of atomic motion roughens equally at all wavelengths; thus, the autocorrelation function of a stochastic surface is constant versus wave vector. Lateral smoothing mechanisms oppose the growth of a stochastic surface and the

⁸ In addition, images of periodic structures of known periodicity fabricated by lithographic means were analyzed by the MATLAB routine to check the accuracy of the program in determining periodicity.

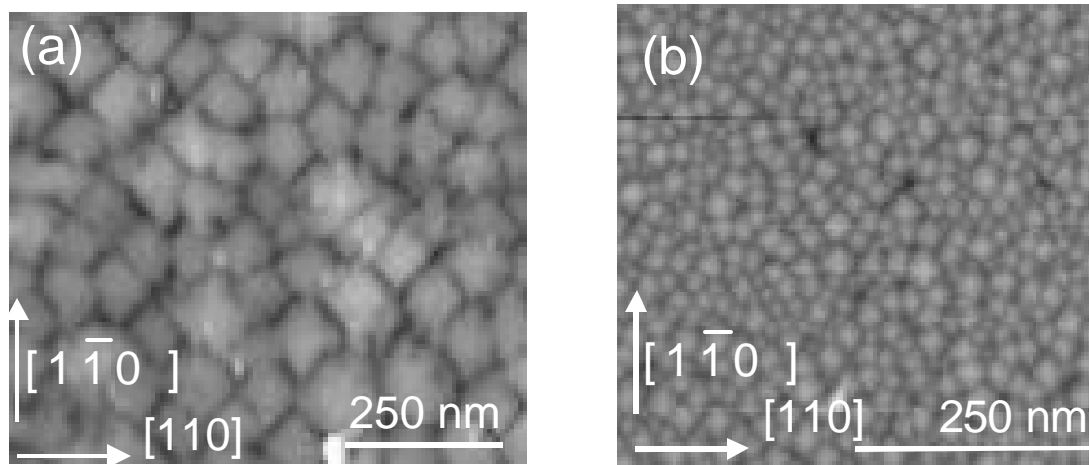


Figure 4-17: Planar view AFM images with $\epsilon = 0.5\%$ of (a) Ge/SiGe (b) $\text{Sn}_{0.018}\text{Ge}_{0.982}/\text{Ge}$.

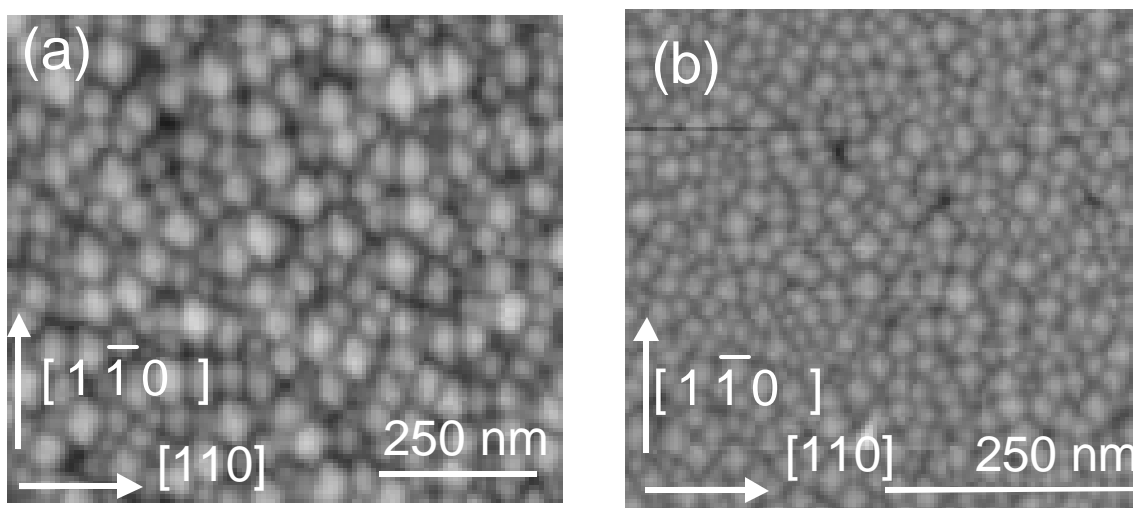


Figure 4-18: Planar view AFM images of $\text{Sn}_x\text{Ge}_{1-x}/\text{Ge}$ with $x = 0.018$ and (a) $\epsilon = 0.26\%$ (b) $\epsilon = 0.5\%$.

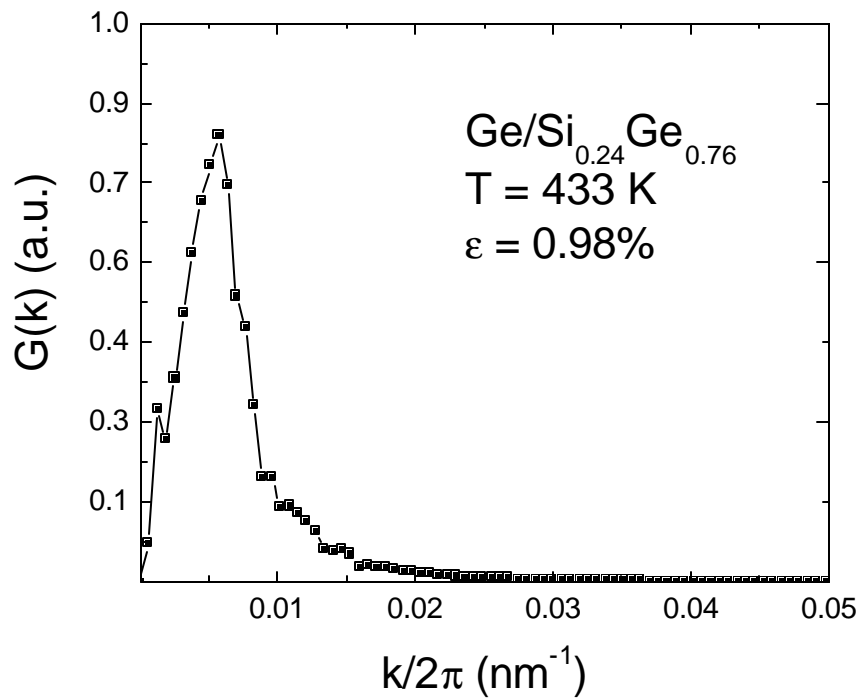


Figure 4-19: Autocorrelation function versus wave vector for Ge/Si_{0.24}Ge_{0.76} with $\varepsilon = 0.98\%$.

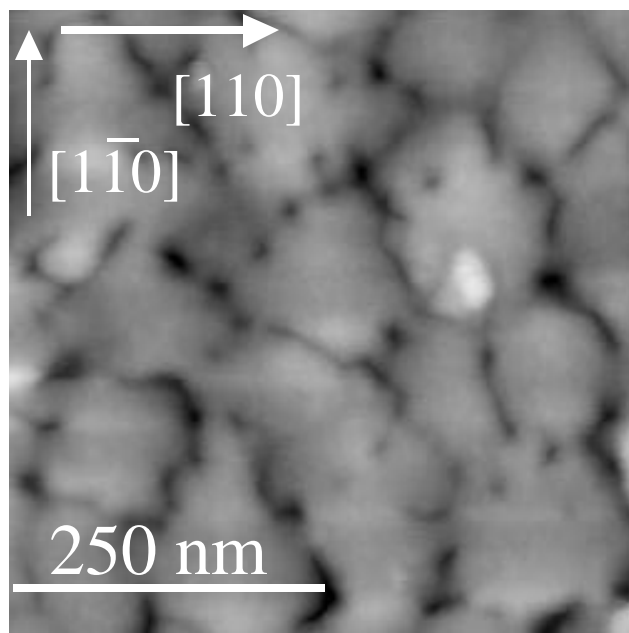


Figure 4-20: AFM image of Ge/Si_{0.24}Ge_{0.76} film with $\varepsilon = 0.98\%$.

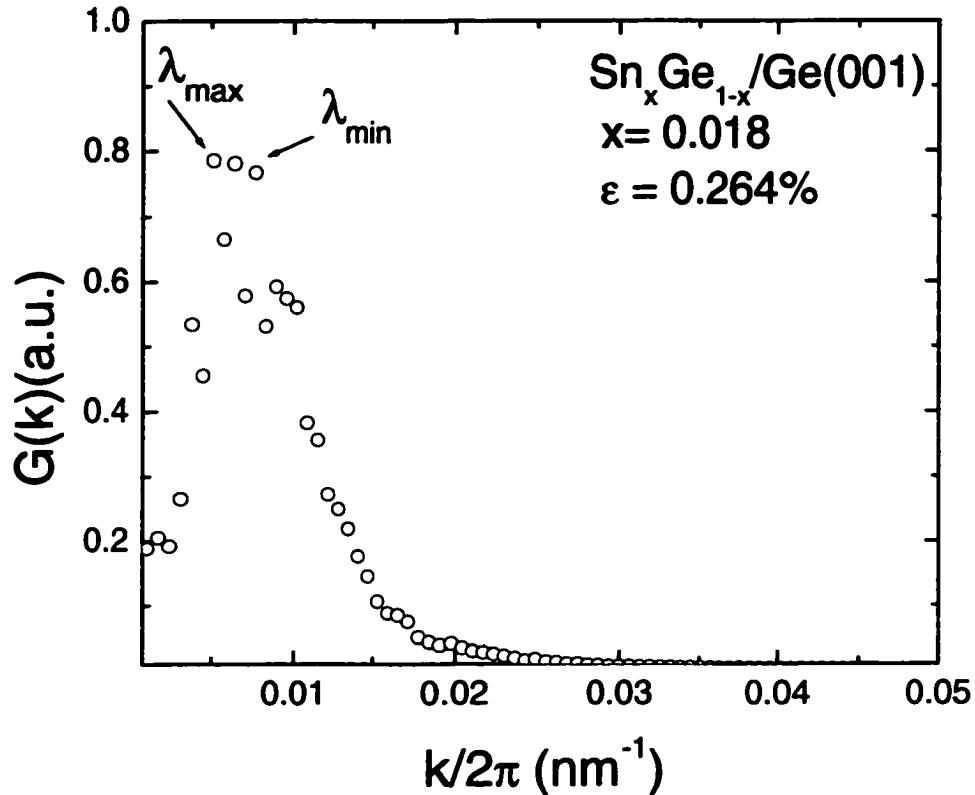


Figure 4-21: Autocorrelation versus instability wave vector for $\text{Sn}_{0.018}\text{Ge}_{0.982}/\text{Ge}(001)$ with $\varepsilon = 0.264\%$. The error in determining the peak value is represented as λ_{\max} and λ_{\min} , referring to the minimum and maximum value of k at the peak, respectively.

slope of the log-log plot of the autocorrelation function versus wave vector is the signature of the physical mechanism dominating surface smoothing.²² The dependence of $G(k)$ on the wave vector can be written as

$$G(k) \propto \frac{1}{k^n} \quad (31)$$

In Figure 4-22, the decay of the peak value of the autocorrelation function is seen for the $\text{Sn}_{0.018}\text{Ge}_{0.982}/\text{Ge}(001)$ alloy as well as a stochastic surface. A value of $n = 2$ is often attributed to evaporation-recondensation, $n = 3$: bulk diffusion,

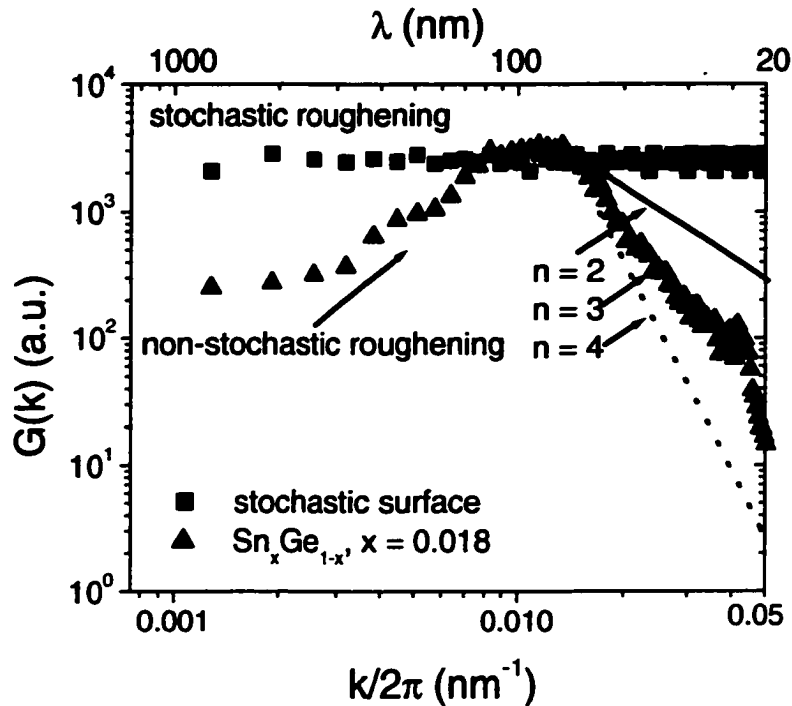


Figure 4-22: Autocorrelation function versus wavevector for a stochastic surface (squares) and $\text{Sn}_{0.018}\text{Ge}_{0.982}/\text{Ge}(001)$ alloy (triangles). The decay of the peak value scales as k^{-n} . The solid line represents a decay of $n = 2$ and the dashed line of $n = 4$.

and $n = 4$: surface diffusion.²² In order to determine the effect of low growth temperature on the surface morphology, a strain free Ge/Ge(001) homoepitaxial film was grown at the $\text{Sn}_x\text{Ge}_{1-x}$ growth temperature, 433 K. The autocorrelation function for unstrained Ge at $T = 433$ K did not have a maxima and the decay of the signal was proportional to k^{-2} , seen in Figure 4-23. Alternatively, the strained Ge and $\text{Sn}_x\text{Ge}_{1-x}$ films at $T = 433$ K and 623 K scale approximately as k^{-3} as seen in Figure 4-22. Thus, a physically different phenomenon was smoothing the strained epitaxial films versus the unstrained Ge film during growth. A slope of

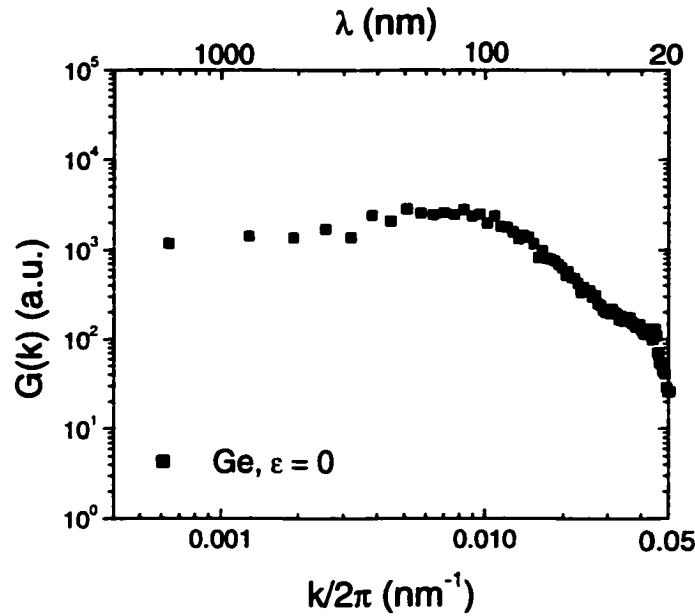


Figure 4-23: Autocorrelation function versus wave vector for unstrained Ge film grown at $T = 160\text{ }^{\circ}\text{C}$.

k^{-3} is often attributed to bulk diffusion; but the $\text{Sn}_x\text{Ge}_{1-x}$ alloys were grown at sufficiently low substrate temperatures such that bulk diffusion was negligible. The insignificant rate of bulk diffusion was confirmed by the absence of Sn surface segregation.

Since the smoothing mechanism of the phase-separated films was not associated with bulk diffusion, another mechanism must be identified. A kinetic rate equation can be written for surface growth:²³

$$\frac{\partial G(k, t)}{\partial t} \propto -k^n G(|k|, t) + \eta(k, t) \quad (32)$$

where $\eta(k, t)$ is the reciprocal space term for stochastic roughening and $G(|k|, t)$ is the radial average of the autocorrelation function. In the kinetic model,⁹ the amplification rate of the growth instability has a term that couples surface

diffusion and strain exhibiting a k^3 dependence. Hence, the decay of $G(k)$ has the signature of a dynamic growth instability.

4.3.3 Thermodynamic model

4.3.3.1 Description

Asaro, Tiller²⁴ and Grinfeld²⁵ using elastic energy calculations, determined that a planar thin film subject to non-hydrostatic stress, such as biaxial strain, relieves coherency energy by forming an undulated surface. A film in biaxial compression, as is $\text{Sn}_x\text{Ge}_{1-x}$ on Ge(001), can relax at the crest of the surface undulation where the lattice constant is larger; thus, relieving coherency energy without dislocation introduction (Figure 4-24). The strain field introduced by the surface undulation, or morphological instability, introduces a driving force for segregation of the larger Sn atom to the crests of the undulation with one mass transport mechanism being surface diffusion during growth. The increase in surface energy associated with a rough surface is a stabilizing mechanism for the surface and gives a lower bound for the instability wavelength. The morphological instability wave vector (k_c^m), an upper bound for the instability wave vector, scales with the square of the misfit (ϵ).

$$k_c^m = \frac{8CE\epsilon^2}{\Gamma} \quad (33)$$

where C is related to the Poisson ratio: $1+\nu/4(1-\nu)$, E is Young's Modulus, and Γ is the surface tension. This elastic energy argument does not include the effect of compositional stresses that were determined to be important experimentally. A thermodynamic model¹⁵ was investigated that arbitrarily couples the morphological instability with compositional fluctuations. This model includes critical parameters of the system: coherent relaxation of the epitaxial film, changes in surface energy due to the surface undulation, and chemical mixing terms. The regular solution model was employed to capture the changes in the enthalpy and entropy of the system associated with clustering of Sn atoms. Although kinetic barriers may inhibit the evolution of the instability, the thermodynamic model addressed whether the energy of the system was lowered by transforming from a homogeneous, planar film (reference state) to a phase-separated film with an undulated surface (modulated state). If not energetically favorable, the instability should not occur regardless of kinetic factors.

Since coherent relaxation occurs near the crest of a surface undulation, the lattice parameter varies across the surface. The variation of the lattice parameter due to coupling of phase-separation with a surface undulation is

$$a(x, z) = a_0[1 + \varepsilon + \varepsilon_c g(kz)e^{kz} \sin kx] \quad (34)$$

where a_0 is the lattice parameter of the substrate, ε is the average misfit, ε_c is the additional misfit associated with phase-separation and $g(kz)$ accounts for variations in the composition of the alloy layer along the growth direction.

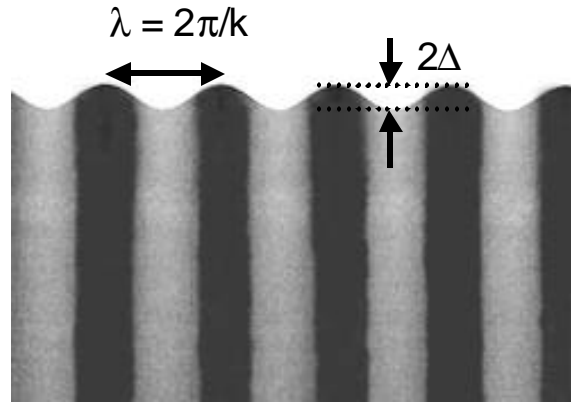


Figure 4-24: Schematic representing phase-separation of Sn to regions of positive curvature on the surface with a characteristic period of λ and Δ represents the height of the surface undulation.

The change in the areal free enthalpy between the reference and the modulated state is

$$dH(\Delta, e_c) = \quad (35)$$

$$(-2CEke^2 + \Gamma \frac{k^2}{4})\Delta^2 - 4CEJ_1 e \Delta e_c + \frac{1}{2k} \left(\frac{R}{h^2} \frac{[T - T_c^c(x)]}{2x(1-x)} J_2 - 4CEJ_1^2 \right) e_c^2$$

where Δ corresponds to the height of the surface undulation (Figure 4-24), R is the gas constant, $\eta = (1/a)(da/dx)$ is the solute expansion coefficient and

$$J_n = \int_{-\infty}^0 [g(u)]^n e^{2u} du \quad \text{where } n = 1, 2. \quad (36)$$

By setting $\delta H = 0$ a critical wave vector was obtained in equation (37) that defines the stability boundary.

$$k_c' = \left[1 - \frac{CEh^2}{R(T - T_c^c)} \right]^{-1} k_c^m \quad (37)$$

where the coherent spinodal temperature is

$$T_c^c = \left[1 - \frac{E}{1-\nu} \frac{\eta^2}{\Omega} \right] 2x(1-x) \frac{\Omega}{R} \quad (38)$$

where Ω is the chemical mixing term.

4.3.3.2 Comparison with experiment

Equation (37) was used to calculate the value of the instability wave vector predicted by the thermodynamic model. The elastic constants were linearly interpolated using values for pure Sn and Ge.¹³ The misfit was calculated assuming the virtual crystal approximation for $\text{Si}_y\text{Ge}_{1-y}$ and $\text{Sn}_x\text{Ge}_{1-x}$. The chemical mixing term, Ω , in equation (38), was calculated by fitting the solidus in the Sn-Ge phase diagram with the Gibbs function and a value of 27 KJ/mol was used in the calculation.²⁶ The surface energy, 0.77 J/m², used corresponded a Ge(001) 2×1 reconstructed surface.^{27,28} It is important to note that there are no free parameters in the calculation. Insertion of these values in equation (37) generated a value for the critical wave vector. Theoretically, the wave vector increased with increasing misfit and Sn composition and decreased with increasing temperature. This trend was in agreement with the experimentally observed decrease in wavelength in the AFM images (Figure 4-17 and Figure 4-18) with increasing strain and composition.

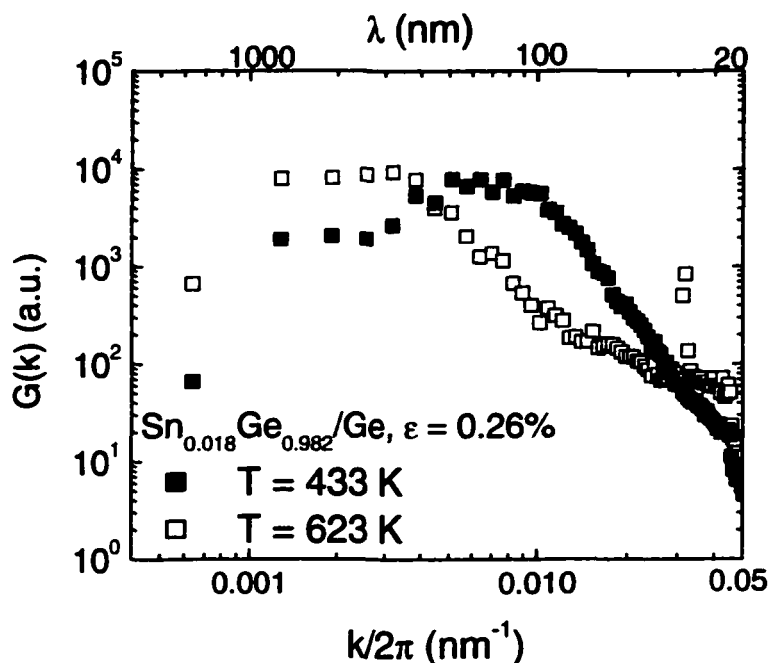


Figure 4-25: Autocorrelation function, $G(k)$ versus wave vector for $\text{Sn}_x\text{Ge}_{1-x}/\text{Ge}(001)$ with misfit of 0.26% and $T = 433$ K (closed squares) and $T = 623$ K (open squares).

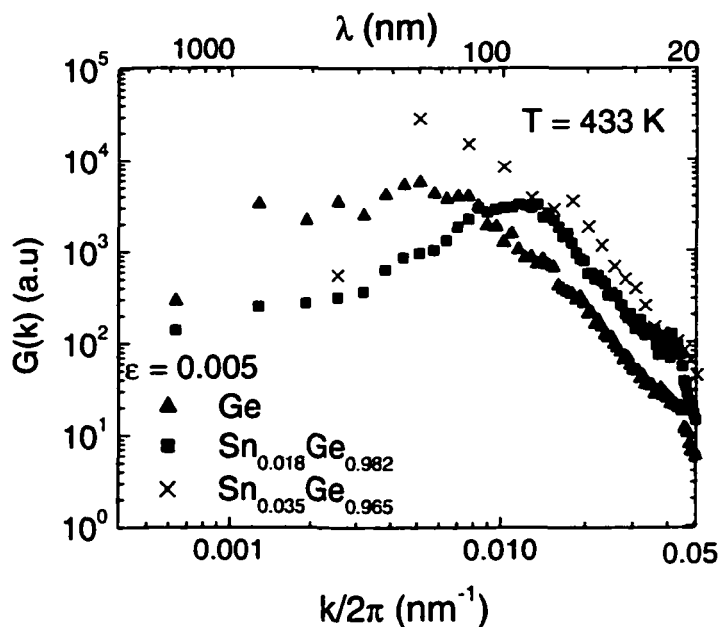


Figure 4-26: Autocorrelation function, $G(k)$ versus wave vector for Ge/SiGe and $\text{Sn}_x\text{Ge}_{1-x}/\text{SiGe}$ with $x = 0.018$ and 0.035 . The misfit of the three films is 0.5%.

In Figure 4-25, the effect of growth temperature on the instability wavelength is shown. The $\text{Sn}_x\text{Ge}_{1-x}$ growth temperature was varied between 160 and 350 °C.⁹ The maxima of $G(k)$ shifted to higher values of the wave vector with the decreased temperature, exhibited by a shift to the right in the log-log plot. The decrease in the instability wave vector with increasing temperature was in agreement with the thermodynamic model. In Figure 4-26, the Sn composition was varied from $0 < x < 0.035$ at nearly constant strain (0.5%) and temperature, 160 °C. Increasing the Sn composition at constant strain increased the wave vector as expected from the thermodynamic model.

In Table 4.1, the experimentally measured values and thermodynamic model predictions of the instability wavelength were tabulated to show the dependence on Sn composition. The maximum and minimum values of the wavelength represent the experimental error in determining the peak of the autocorrelation function. In Table 4.2, the variation of the instability wavelength with varying strain and constant Sn composition is displayed. The general trend of the data was a decrease in the instability wavelength with increasing Sn composition and strain. Although, the trends of the thermodynamic model were followed, the agreement between theory and experiment was poor. The magnitude of wave vector predicted by the thermodynamic model differed from

⁹ The growth rate for the high temperature film, 350 °C, was increased slightly from 0.05 to 0.08 nm/sec to inhibit Sn surface segregation.

the experimentally measured wave vector by an order of magnitude for misfit less than 0.6%. The agreement between theory and experiment was better at higher values of the misfit, > 0.6%, where the experimental and predicted values differed by approximately a factor of two.

Sn comp.	Si comp.	Misfit (%)	λ : peak value(nm)	λ : max. value(nm)	λ : min. value(nm)	Thermo. Model
0	0.11	.445	224	262	196	683
0.015	0.06	.463	108	131	93	494
0.015	0.065	.484	95	98	79	452
0.018	.05	.467	98	112	93	459
0	0.13	.527	196	224	174	487
0.015	0.08	.544	157	196	131	358
0.018	0.06	.507	98	121	75	389
0.035	0	.514	75	157	56	266
0.016	0.15	.845	71	79	65	146
0.020	0.13	.822	98	131	79	142
0	0.24	.977	170	192	163	142
0.022	0.15	.933	78	98	65	106
0.015	0.22	1.12	75	87	65	86
0.070	0	1.03	30	33	29	10

Table 4.1: Experimentally determined values of instability wavelength versus the values predicted by the thermodynamic model. Double lines distinguish between sets of data with constant strain and varying Sn composition. The maximum and minimum values of λ represent the error in determining the peak value.

Sn comp.	Si comp.	Misfit (%)	λ : peak value(nm)	λ : max. value(nm)	λ : min. value(nm)	Thermo. Model
0.015	0.06	.463	108	131	93	494
0.015	0.065	.484	95	98	79	452
0.015	0.22	1.112	75	87	65	86
0.017	0	.25	314	392	262	1793
0.018	0	.264	157	196	131	1435
0.018	0.05	.467	98	112	87	459
0.018	0.06	.507	93	121	75	389
0.016	0.15	.845	71	157	112	146
0.02	0.08	.618	139	174	131	252
0.02	0.13	.822	98	131	79	142
0.022	0.15	.933	78	98	65	106
0	0.11	.445	224	262	196	683
0	0.13	.527	185	196	174	487
0	0.24	.977	170	192	156	142

Table 4.2: Experimentally determined values of instability wavelength versus the values predicted by the thermodynamic model. Double lines distinguish between sets of data with constant Sn composition and varying strain. The maximum and minimum values of λ represent the error in determining the peak value.

The very limited success of the thermodynamic model was partly ascribed to the low growth temperature, the surface diffusion of atoms on the surface may be limited such that thermodynamic equilibrium is not achieved. This thermodynamic model assumes an arbitrary coupling between the composition and surface morphology. The lack of agreement between experiment and the thermodynamic model may also be attributed to this arbitrary coupling that does not include the physically relevant couplings of composition and strain during dynamic growth.

4.3.4 Kinetic model

4.3.4.1 Description

Since the phase-separation of Sn into $\text{Sn}_x\text{Ge}_{1-x}$ wires oriented along the growth direction was associated with growth, the instability was compared with a kinetic model¹⁶ that incorporates mass transport mechanisms relevant during molecular epitaxy. This kinetic theory modeled growth of a binary alloy, A_xB_{1-x} . As in the thermodynamic model, lattice misfit with respect to the substrate and local composition fluctuations produced strain fields in the alloy film and were driving forces associated with the growth instability. In addition, the mass transport mechanisms, surface diffusion and deposition, were factors in the development of the growth instability. The surface was subject to a condition of local equilibrium at the film-vapor interface. Therefore, this model applies to

conditions of low growth rates and, thus, is applicable for the growth rate of $\text{Sn}_x\text{Ge}_{1-x}$ alloys. (The growth rate was 0.05 nm/sec.) The surface composition was determined in terms of stress and curvature non-uniformities. Using linear stability analysis, a perturbation of the height and composition of the surface is introduced. If the amplification rate of the growth instability has real positive solutions, then the system is unstable.

Following the above analysis, the details of the calculations for the amplification rate of the growth instability are outlined below. The growth front of the alloy film was subject to a condition of local equilibrium of the film-vapor interface denoted by Σ . The composition at the surface, Q_n , was determined to be the average film composition, x , and may be different from the local composition, C^f , at a point on the surface and the equilibrium vapor composition, C^v . The surface velocity, v , was defined by a rate equation:

$$\rho_o(C^v - C^f)\vec{v} \cdot \vec{n} = \bar{V}_\Sigma \cdot \vec{J}^\Sigma + (x - C^v)Q_n \quad (39)$$

where ρ_o is the molar density of the lattice sites in the film, \vec{n} is the unit normal pointing from the film to the vapor, J^Σ is the flux of A atoms on the surface:

$$\vec{J}^\Sigma = -(\Gamma_o D^\Sigma / G_m') \bar{V}_\Sigma M_{AB} \quad (40)$$

where Γ_o is the surface density of lattice sites on Σ , G_m is the molar Gibbs free energy of the film, M_{AB} is the chemical potential at the surface and G_m'' is

$$\dot{G}_m = \left(\frac{\partial^2 G_m}{\partial C^f{}^2} \right)_{C^f=x} \quad (41)$$

The Gibbs-Thomson relationship was used to incorporate the thermodynamics of a stressed solid.²⁹

$$C^f = - \frac{V_o(\kappa\Gamma + \tilde{\xi} - \Delta\bar{C}\eta\tilde{T}_{kk})}{\dot{G}_m(\Delta\bar{C} + \psi)} \quad (42)$$

The surface gradient of the chemical potential is

$$\bar{\nabla}_\Sigma M_{AB} = \frac{V_o}{\Delta\bar{C} + \psi} \bar{\nabla}_\Sigma(\kappa\Gamma + \tilde{\xi} + \psi\eta\tilde{T}_{kk}) \quad (43)$$

where κ is the mean curvature of the surface, $\tilde{\xi}$ is the elastic strain energy density, V_o is the molar volume, $\Delta\bar{C} = C^v - C^f$, T_{kk} is the trace of the stress, and $\psi = V_o\eta\tilde{T}_{kk} / \dot{G}_m$. From equation (43), the presence of compositional stresses was seen to affect the value of the chemical potential. In order to determine the stress state of the film, the equation relating stress and strain was

$$T = C[E - (\epsilon + \eta\tilde{C}^f)1] \quad (44)$$

where T , C , E are the elastic stress, stiffness, and strain tensors, respectively, and 1 is the unit tensor. Mechanical equilibrium at the surface required that the surface is stress free such that the normal component of the stress tensor is zero. All perturbations decay far from the surface, that is, bulk diffusion in the film

was assumed to be negligible. The stability of the interface was determined by linearizing all quantities about the planar state. Normal mode solutions of the form $\exp(\sigma t + i \vec{k} \cdot \vec{x})$ resulted where σ is the amplification rate of the perturbation. If $\text{Re}(\sigma) < 0$, then the system was stable; if $\text{Re}(\sigma) > 0$, then the system was unstable. If $\text{Im}(\sigma) \neq 0$, then an oscillatory instability was present. Solving for the elastic field, assuming mechanical equilibrium in the infinitesimal strain approximation, and using equation (39) and equation (42), the amplification rate was calculated as

$$\begin{aligned} \sigma^2 - \sigma \left\{ D^{\Sigma^*} k^3 \left(\varepsilon^{*2} - \frac{k\Gamma}{\chi} \right) + kV \left[(\varepsilon^* + \eta^*)^2 - \frac{k\Gamma}{\chi} - 1 \right] \right\} \\ - kV \left\{ D^{\Sigma^*} k^3 \left[\varepsilon^{*2} + (\eta^{*2} - 1) \frac{k\Gamma}{\chi} \right] + kV \left(\varepsilon^{*2} - \varepsilon^* \eta^* + \frac{k\Gamma}{\chi} \right) \right\} = 0 \end{aligned} \quad (45)$$

where D^{Σ^*} is a scaled surface diffusivity, ε^* is a scaled misfit, η^* is a called scaled solute expansion coefficient, and V is the film growth rate. These terms are all defined in the following equations:

$$D^{\Sigma^*} = V_0 \Gamma_0 D^{\Sigma} (G_m^* + 2V_0 \eta^2 E / (1-\nu)) \frac{(1-x)x}{RT} \quad (46)$$

$$\varepsilon^* = \left[\frac{2(1+\nu)E}{\chi(1-\nu)} \right]^{\frac{1}{2}} \varepsilon \quad (47)$$

$$\eta^* = \left[\frac{2(1+\nu)E}{\chi(1-\nu)} \right]^{\frac{1}{2}} \eta(x) \quad (48)$$

$$\chi = (G_m^* + 2V_0 \eta^2 E / (1-\nu)) \Delta \bar{C}^2 / V_0 \quad (49)$$

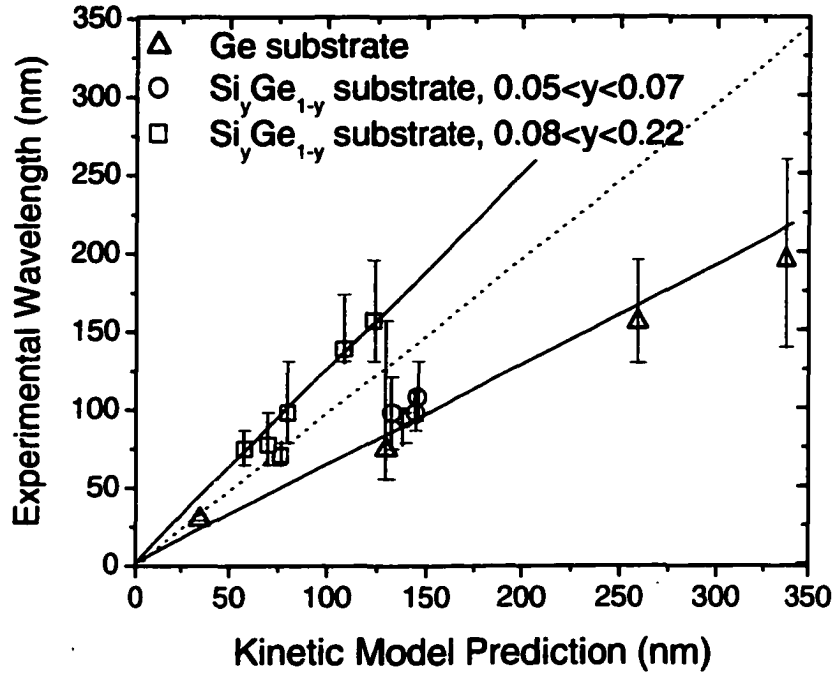


Figure 4-27: Experimental value for fastest growing instability wavelength versus value predicted by kinetic model. The line is a guide to the eye.

4.3.4.2 Comparison to experiment

Equation (22) was solved numerically for the $\text{Sn}_x\text{Ge}_{1-x}$ alloy system to calculate the value of the fastest growing instability wavelength predicted by the kinetic model and compare this to the measured experimental results. The elastic constants were assumed independent of composition. The value of the surface diffusivity and surface energy used in the calculation were $D = 8.45 \times 10^{-6} (\text{cm}^2/\text{sec}) \exp(-0.83/kT)^{30}$ and $\Gamma = 1.927 \text{ J/m}^2$,²⁸ respectively, and corresponded to pure Ge. The value of the instability wavelength predicted by the kinetic model was more sensitive to strain than composition. Experimentally, the composition

had a greater impact on the instability wavelength. The diffusional fluxes of the Sn and Ge atoms at the surface were coupled. This assumption of coupling may have limited the contribution of increased Sn composition on the instability wavelength. Figure 4-27 compares the experimental value of the fastest growing wavelength versus the kinetic model prediction. The line represents a one to one correlation and was included as a guide to the eye. The experimental data followed two different trends; one trend was followed for Si compositions less than 0.07 and another for Si compositions greater than 0.07 in the virtual substrate. The different trends can be attributed to the partial relaxation of the SiGe virtual substrates. The theoretical calculations were performed for fully relaxed SiGe substrates. Although the error bars do not cross the line for the fully relaxed substrates, the percentage by which the data and theory differ was consistent for these samples. The agreement between the theory and experiment was reasonable when considering the uncertainties in many of the parameters in equation (22). The mechanisms incorporated in the kinetic model, that is surface diffusion and incoming flux of the beam, appeared to influence the growth instability. For control of the instability wavelength, the corresponding controllable parameters during growth are temperature and growth rate.

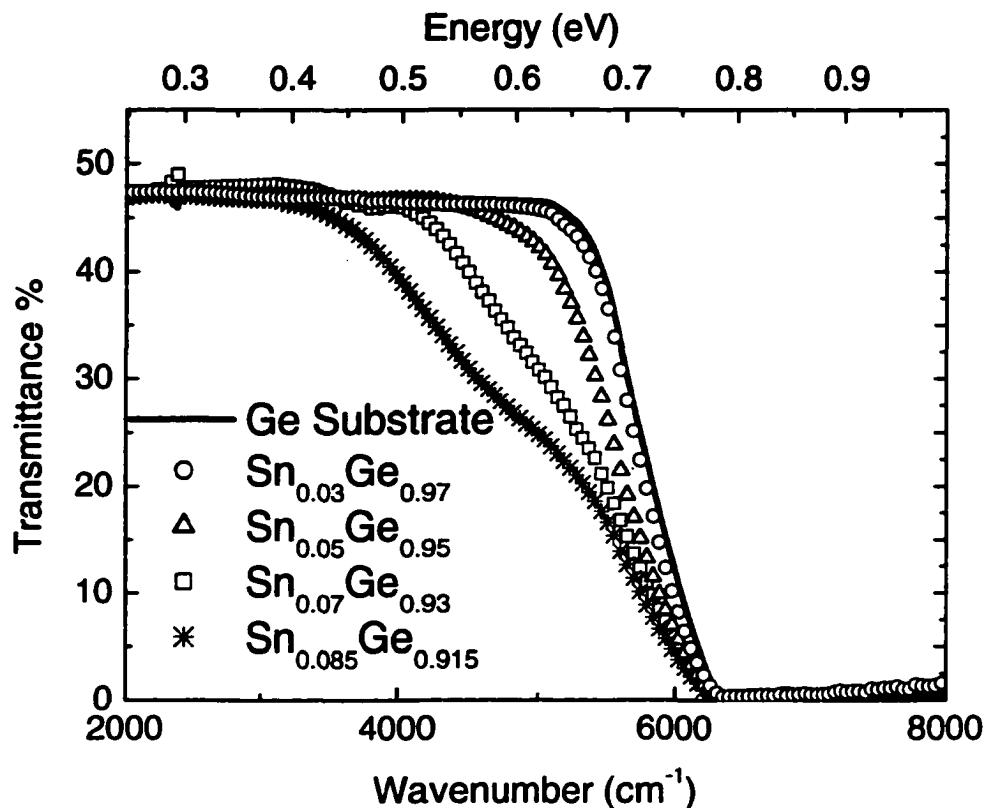


Figure 4-28: Transmittance versus wavenumber for $\text{Sn}_x\text{Ge}_{1-x}$ with average Sn composition between $0 < x < 0.085$ and film thickness of $1 \mu\text{m}$.

4.4 Optical characterization

The transmittance spectra of $1 \mu\text{m}$ thick phase-separated $\text{Sn}_x\text{Ge}_{1-x}/\text{Ge}(001)$ films with Sn compositions of $0.05 < x < 0.085$ was measured via FT-IR spectroscopy. Previous measurements of the energy bandgap demonstrated that the direct energy bandgap decreases as a function of increasing Sn composition.^{10,11} Therefore Sn-rich regions in the phase-separated films were expected to absorb at lower energy. By modeling the absorption edge, the phase-

separated $\text{Sn}_x\text{Ge}_{1-x}$ films were determined to have a lower direct energy bandgap than homogeneous films with the same average Sn composition.

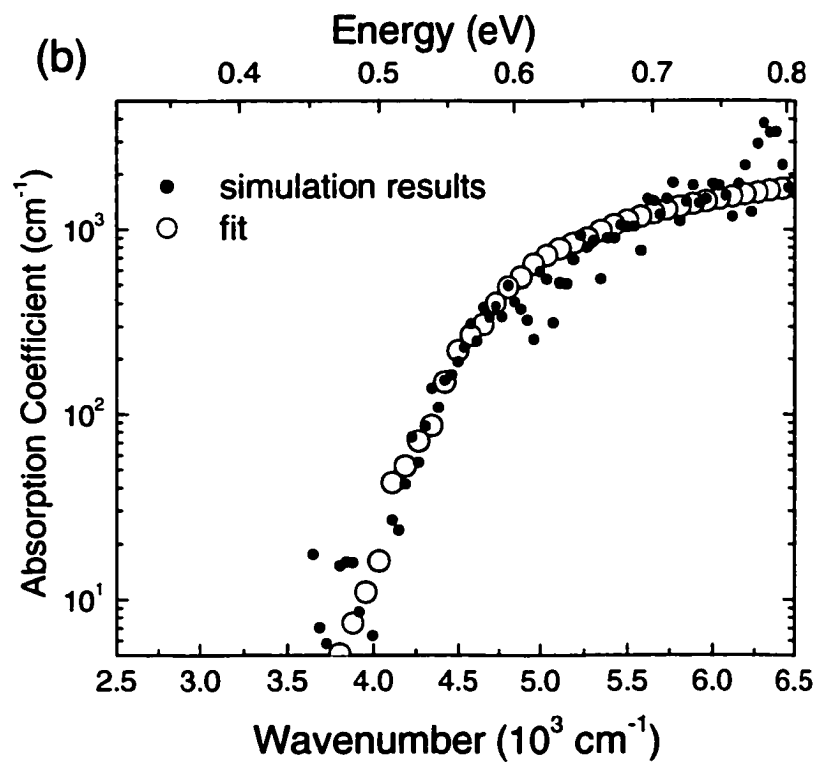
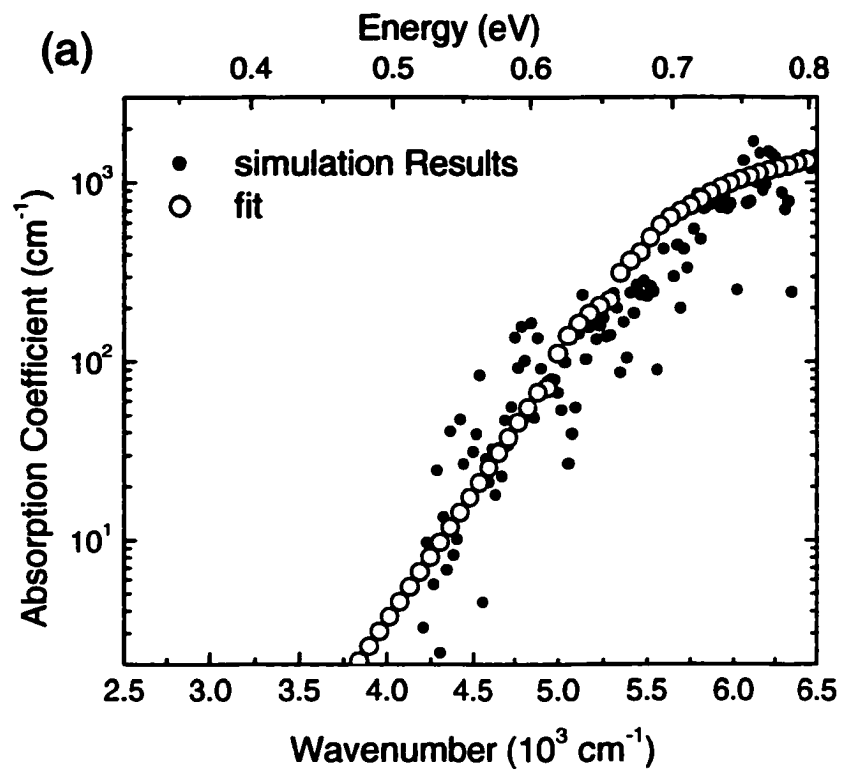
FT-IR transmittance measurements were performed at 1000 to 8000 cm^{-1} on the phase-separated $\text{Sn}_x\text{Ge}_{1-x}$ alloys. The sample compartment was purged with dry nitrogen to reduce absorption of the IR signal by the ambient. An aperture was inserted to reduce the beam size incident on the sample to 5 mm. The transmittance spectra that is shown in Figure 4-28 for $\text{Sn}_x\text{Ge}_{1-x}$ alloys films with Sn compositions $0 < x < 0.085$ showed a shift to lower energies for the onset of absorption with increasing Sn composition.

Using a commercial software package,¹⁰ the transmittance curve was simulated between 3000 and 8000 cm^{-1} to obtain a value for the dielectric function. The dielectric function for homogeneous alloys with the same Sn composition was used as input to the simulation for the first iteration. The extinction coefficient was iteratively fit to minimize the root-mean-square-error between the simulated transmittance curve and the experimental transmittance spectrum. Once the best fit was obtained, the simulation yielded a relationship between the extinction coefficient (k) and wavenumber. This dispersion relationship was used to calculate the absorption coefficient (α):

$$\alpha(\omega) = 2\omega k(\omega) \quad (50)$$

¹⁰ SCI, Optical Thin Film Software

where ω is the frequency in wavenumbers. The absorption coefficient generated by minimizing the root-mean-square-error between the simulation and the experimental transmittance spectra is shown as closed symbols in Figure 4-29 for Sn compositions $x = 0.05$ (a), 0.07 (b), and 0.085 (c). Under a parabolic band approximation, the absorption edge has a power dependence on the direct energy bandgap of 0.5, and on the indirect energy bandgap of 2. The absorption coefficient generated from the simulation was fit with this functional form of the absorption coefficient using the parabolic band approximation. An Urbach tail was included in the functional form to take into account defect states in the energy bandgap due to disorder in the lattice. The functional form of the absorption coefficient (open circles) is also shown in Figure 4-29. The absorption coefficient was $2 \times 10^3 \text{ cm}^{-1}$ near the bandgap energy. The fit of the absorption coefficient was insensitive to the indirect energy gap but very sensitive to direct energy gap contributions and the Urbach tail. In order to fit the absorption coefficient, multiple direct energy bandgap contributions were necessary. If the Sn composition is a smoothly varying function across the surface due to phase-separation, local regions of different Sn compositions will each absorb at a different bandgap energy. The spot size of the incident beam was 5 mm and hence the beam sampled Sn-rich and Ge-rich regions simultaneously. The minimum value of the energy bandgap determined in this manner is shown in Figure 4-30 along with the energy bandgap for homogeneous $\text{Sn}_x\text{Ge}_{1-x}$ alloy films.¹⁰ The phase-separated films exhibited a lower direct energy bandgap in



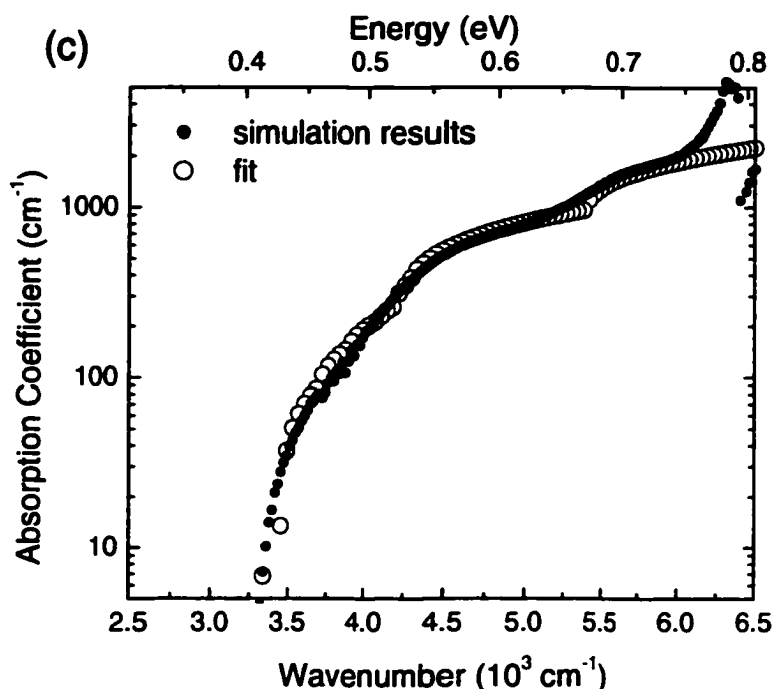


Figure 4-29: Absorption coefficient generated by simulation (closed symbols) and fit of the absorption edge (open circles) using the power law dependence on the bandgap energy and an Urbach tail for $x =$ (a) 0.05, (b) 0.07, and (c) 0.085.

comparison to homogeneous alloy films having the same average Sn composition.

The energy bandgap was found to decrease with increasing Sn composition as in previous work.^{10,11} The energy bandgap decreased for the thicker phase-separated films in comparison to homogeneous films with the same average Sn composition. The absorption edge exhibited a sharp increase that is characteristic of a direct bandgap for the $\text{Sn}_{0.07}\text{Ge}_{0.93}$ alloy, whereas

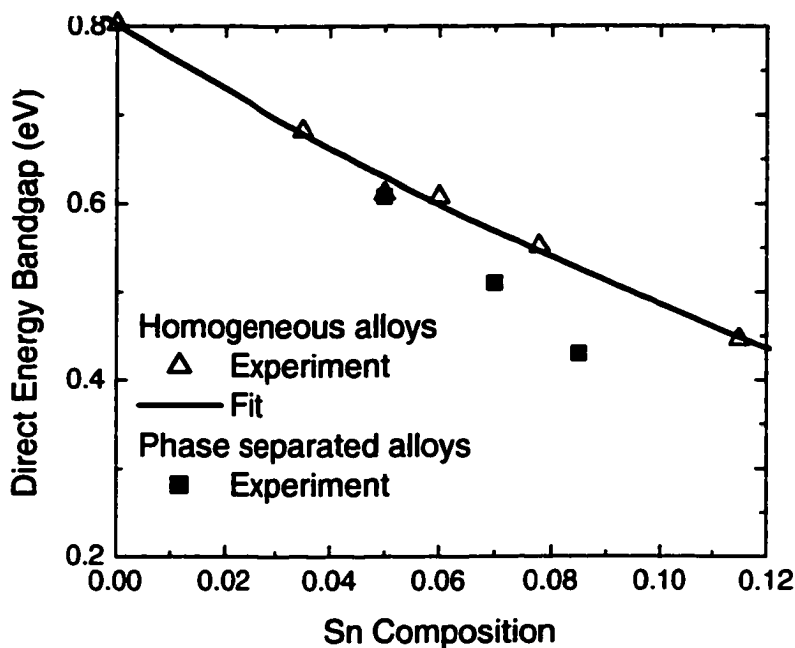


Figure 4-30: Bandgap energy versus Sn composition for homogeneous $\text{Sn}_x\text{Ge}_{1-x}$ alloys (triangles) and phase-separated $\text{Sn}_x\text{Ge}_{1-x}$ alloys (squares).

homogeneous $\text{Sn}_x\text{Ge}_{1-x}$ alloys exhibit a direct energy bandgap near a Sn composition of $x = 0.09$.

4.5 Conclusion

We have grown 1 μm thick $\text{Sn}_x\text{Ge}_{1-x}/\text{Ge}(001)$ epitaxial films with $0 < x < 0.07$ that evolved during growth into a dense array of Sn-enriched $\text{Sn}_x\text{Ge}_{1-x}$ nanowires oriented along [001]. In cross-sectional TEM, the growth instability was not observed in 100 nm thick films but strain in these films was identified as a driving force for the instability. The measured period of the phase-separation in TEM was dependent on the Sn composition. The period of

the phase-separation was measured in cross-section TEM as 65 nm and the size of the Sn-rich rods was 23 nm for a Sn composition of $x = 0.03$. STEM analysis in planar view revealed composition contrast with a rod-like morphology of the $\text{Sn}_x\text{Ge}_{1-x}$ nanowires. Both TEM and AFM analysis indicated that ordering of the Sn-enriched rods occurred along $\{100\}$ in the plane of the film.

The phase-separation observed in STEM was correlated with a surface undulation that was measured in AFM. The autocorrelation function of the AFM images was calculated to experimentally measure the fastest growing wavelength of the growth instability. The experimental value was compared to a thermodynamic and kinetic model. While the thermodynamic model was sufficient to predict the trends associated with the growth instability, the instability wavelengths predicted by the model were much larger than the experimentally determined values. An arbitrary coupling between the Sn composition and the surface undulation is assumed by the model. Thus, the model does not include physically relevant couplings between surface dynamics and compositional non-uniformities. The kinetic model yielded a value for the instability wavelength having much better correlation with the experiment. The value of the instability wavelength predicted by the kinetic model was more sensitive to strain versus composition. Experimentally, the composition had a greater impact on the instability wavelength. One reason was the partial relaxation of the SiGe virtual substrates. Another reason for the discrepancy is that the kinetic model couples the diffusivity of Sn and Ge on the surface. This

coupling may limit the effect of varying Sn composition in the model. In addition the surface energy of the film may change with Sn composition, an effect that is also not incorporated in the model. Yet, the value predicted by the kinetic model for the instability wavelength was in reasonable agreement with the experimentally measured growth instability wavelength. Hence surface diffusion and deposition are two physical processes affecting phase-separation during dynamic growth.

Optical transmittance measurements were performed on thick phase-separated $\text{Sn}_x\text{Ge}_{1-x}$ films with Sn composition between $0.05 < x < 0.085$. The energy bandgap was found to decrease with increasing Sn composition as in previous work.^{10,11} Unique to this work, we have determined that the energy bandgap decreased for the thicker phase-separated films and the absorption edge exhibited a sharp increase that is characteristic of a direct energy bandgap for the $\text{Sn}_{0.07}\text{Ge}_{0.93}$ alloy film, whereas homogeneous $\text{Sn}_x\text{Ge}_{1-x}$ alloys exhibit a direct energy bandgap near a Sn composition of $x = 0.09$.

4.6 Bibliography

1. J. K. N. Mbindyo, B. D. Reiss, B. R. Martin, C. D. Keating, M. J. Natan, and T. E. Mallouk, *Adv. Mat.* 13, 249 (2001)
2. C. D. Bain and G. M. Whitesides, *Angew. Chem.* 101, 522 (1989)
3. A. Ulman, *Introduction to Thin Organic Films: From Langmuir-Blodgett to Self-Assembly* (Academic Press, Boston, 1991)
4. H. Sunamura, N. Usami, Y. Shiraki, and S. Fukatsu, *Appl. Phys. Lett.* 68, 1847 (1996)
5. J. Viernow, D. Y. Petrovykh, F. K. Men, A. Kirakosian, J.-L. Lin, and F. J. Himpsel, *Appl. Phys. Lett.* 74, 2125 (1999)
6. R. D. Twesten, D. M. Follstaedt, S. R. Lee, E. D. Jones, J. L. Reno, J. Mirecki Millunchick, A. G. Norman, S. P. Ahrenkiel, and M. A., *Phys. Rev. B* 60, 13619 (1991)
7. F. Liu, A. H. Li, and M. G. Lagally, *Phys. Rev. Lett.* 87, 6103 (2001)
8. S. J. Pennycook, S. D. Berger, and R. J. Culbertson, *J. Microscopy* 144, 229 (1986)
9. J. E. Guyer, S. A. Barnett, and P. W. Voorhees, *J. Cryst. Growth* 217, 1 (2000)
10. R. Ragan and H. A. Atwater, *Appl. Phys. Lett.* 77, 3418 (2000)
11. G. He and H. A. Atwater, *Phys. Rev. Lett.* 79, 1937 (1997)
12. E. Anastassakis, A. Pinczuk, E. Burstein, F. H. Pollak, and M. Cardona, *Solid State Comm.* 88, 1053 (1970)
13. E. A. Fitzgerald, P. E. Freeland, M. T. Asom, W. P. Lowe, R. A. Macharrie, B. E. Weir, A. R. Kortan, F. A. Thiel, Y. H. Xie, A. M. Sergent, S. L. Cooper, G. A. Thomas, and L. C. Kimmerling, *J. Elec. Mat.* 20, 489 (1991)

14. P. Hirsch, A. Howie, R. Nicholson, D. W. Pashley, and M. J. Whelan, *Electron Microscopy of Thin Crystals* (Robert E. Krieger Publishing Co., Malabar, 1977).
15. F. Glas, *Phys. Rev. B* 55, 11277 (1997)
16. J. E. Guyer and P. W. Voorhees, *J. Cryst. Growth* 187, 150 (1998)
17. B. J. Fultz and J. Howe, *Transmission Electron Microscopy and Diffractometry of Materials* (Springer, Pasadena, 2000).
18. D. E. Jesson, S. J. Pennycook, J. M. Baribeau, and D. C. Houghton, *Phys. Rev. Lett.* 71, 1744 (1993)
19. J. E. Guyer and P. W. Voorhees, *Phys. Rev. B* 54, 11710 (1996)
20. Y. H. Xie, G. H. Gilmer, C. Roland, P. J. Silverman, S. K. Buratto, J. Y. Cheng, E. A. Fitzgerald, A. R. Kortan, S. Schuppler, M. A. Marcus, and P. H. Cittrin, *Phys. Rev. Lett.* 73, 3006 (1994)
21. E. A. Fitzgerald, *Appl. Phys. Lett.* 59, 811 (1991)
22. W. M. Tong and R. S. Williams, *Ann. Rev. Phys. Chem.* 45, 401 (1994)
23. C. Herring, *J. Appl. Phys.* 21, 301 (1950)
24. R. J. Asaro and W. A. Tiller, *Met. Trans.* 3, 1789 (1972)
25. M. A. Grinfel'd, *Sov. Phys. Dokl.* 290, 1358 (1986)
26. N. Choly, senior thesis (California Institute of Technology, Pasadena, 1999).
27. E. Kasper, in *EMIS Datareviews Series* (INSPEC, London, 1995).
28. J. M. Blakely, *Introduction to the Properties of Crystal Surfaces* (Pergammon Press, Oxford, 1973).
29. F. C. Larche and J. W. Cahn, *Acta Metall.* 33, 331 (1985)
30. E. Chason, J. Y. Tsao, K. M. Horn, S. T. Picraux, and H. A. Atwater, *J. Vac. Sci. Tech. A* 8, 2507 (1990)

Chapter 5 Quantum Confined Structures: Sn Nanowires and Nanocrystals

5.1 Introduction

Self-assembled nanocrystals and nanowires enable the achievement of small feature size using only large-scale lithography and utilize quantum confinement of carriers to produce a Si-compatible direct energy bandgap semiconductor. Diamond cubic Sn¹¹ is a semi-metal with conduction band minima below the Γ point of the valence band. The low electron effective mass of Sn^{1,2} suggests that quantum confinement effects should be manifest at relatively large nanocrystal radii, on the order of 40 nm. Thus, by manipulating the radii of Sn nanocrystals and Sn nanowires, a high degree of tunability of the bandgap energy is expected. A semi-empirical tight-binding bandstructure calculation predicted that the energy bandgap varies from 0 to 2.5 eV for bulk Sn

¹¹ The diamond cubic (α) to tetragonal (β) phase transition occurs at 13.2 °C for bulk Sn. The diamond cubic phase is stable below 13.2 °C.

to nanowires with 10 nm radii.³ Some possible applications for Sn nanocrystals and nanowires are as light-detecting, and light-emitting devices or Sn nanocrystals may be appropriate in quantum cellular automata logical devices.

This chapter summarizes the work on fabrication and characterization of Sn nanocrystals and nanowires using non-lithographic techniques. One focus was the fabrication of Sn nanowires. β -Sn nanowires were prepared by pressure injection of molten Sn into anodic alumina templates. The alumina templates were fabricated with pore diameters ranging from 30 to 40 nm by an electrochemical etching process. The pressure injection was performed in a high-pressure vessel using Ar gas to generate pressures up to 3000 psi. Sn nanowires were fabricated with diameters of 30 to 40 nm and lengths exceeding 1 μ m. Another focus was the fabrication and investigation of the optical properties of α -Sn quantum dots. Quantum dots were fabricated with radii less than 40 nm by post-growth annealing of MBE grown $\text{Sn}_x\text{Ge}_{1-x}$ alloys. Optical transmittance of the α -Sn nanocrystals demonstrated changes in the optical absorption attributed to quantum size effects.

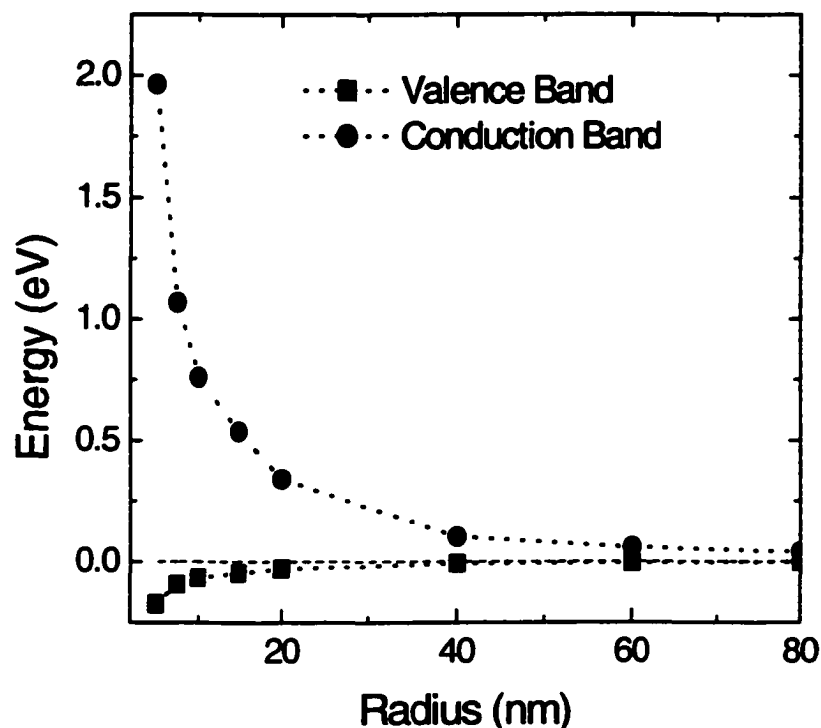


Figure 5.1: Energy of valence band and conduction band with nanowire radius from semi-empirical tight binding calculation.

5.2 Sn nanowires

5.2.1 Quantum confinement effects

Due to the small electron effective mass of α -Sn, $0.0236 m_0$, quantum confinement effects are expected at relatively large diameters, 40 nm or less.

In comparison, quantum confinement effects in Si nanocrystals are not expected until the radius is on the order of 5 nm⁴ and in Ge when the radius is 10 nm.⁵ A semi-empirical tight-binding bandstructure calculation was performed to predict the dependence of the energy bandgap on the nanowire

radius, Figure 5.1.³ The bandgap energy was predicted to be 0.4 eV for a nanowire with a 20 nm radius. Strong quantum confinement effects were predicted when the radius of the nanowire radius reached 5 nm where the bandgap energy was calculated as 2.5 eV. Thus, α -Sn nanowires were predicted to have a high degree of tunability of the energy bandgap with nanowire radius.

5.2.2 Overview: Sn nanowire fabrication

Sn nanowires were fabricated by pressure injection of Sn into hexagonally ordered pores in alumina templates. The template was fabricated from a polished aluminum foil, Figure 5.2 (a). By electrochemical etching and oxidation in oxalic acid (anodization), an initially disordered pore array in an alumina film was grown on an aluminum substrate, Figure 5.2 (b). As the anodization progressed, the pores began to order and then formed a hexagonally packed structure near the alumina/Al interface.⁶ The disordered film was etched leaving a patterned Al foil, Figure 5.2 (c). The second anodization step resulted in an ordered pore array, Figure 5.2 (d). A 500 nm layer of Sn was then deposited on the alumina template in ultra high vacuum (UHV), Figure 5.2 (e). The template was inserted in a high-pressure vessel for injection of Sn into the alumina templates to fabricate Sn nanowires, Figure 5.2(f).

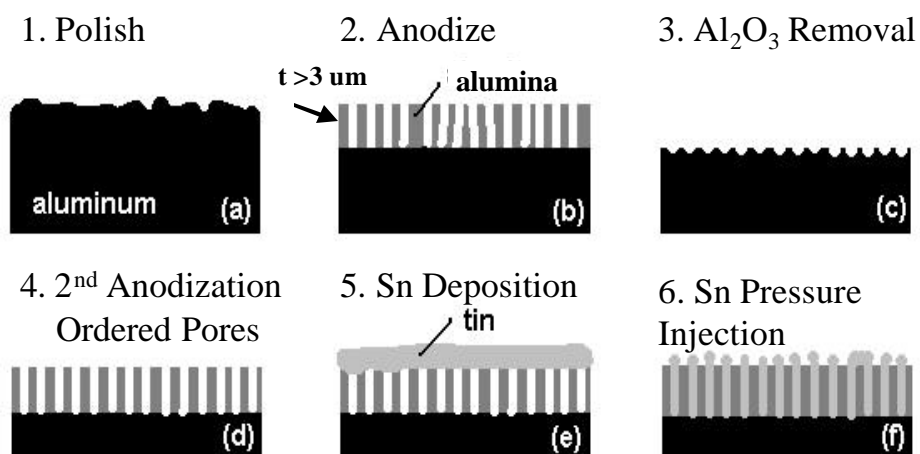


Figure 5.2: Sn nanowire fabrication: (a) Polish Al foil, (b) anodize foil in oxalic acid until ordering begins, (c) etch oxide to expose patterned Al foil, (d) anodize a second time to produce ordered arrays of pores, (e) deposit a layer of Sn in UHV and (f) inject Sn into pores with Ar gas at high pressures.

5.2.3 Template fabrication

The fabrication process of porous, hexagonally ordered alumina templates was first discovered over 4 decades ago.⁷ Applications for nanowires fabricated in hexagonally ordered alumina templates such as magnetic, electronic and optoelectronic devices have created a renewed interest in the fabrication of porous alumina templates.^{8,9} An aluminum foil of $130 \mu\text{m}$ in thickness and 99.999% purity was bonded to a polishing block using crystal bond adhesive and first mechanically polished on a Buehler table using 240 grit sandpaper until the surface was planar. The sample was then polished with 320, 400, and 600 grit sandpaper to remove the scratch marks from the previous polishing step. The Al

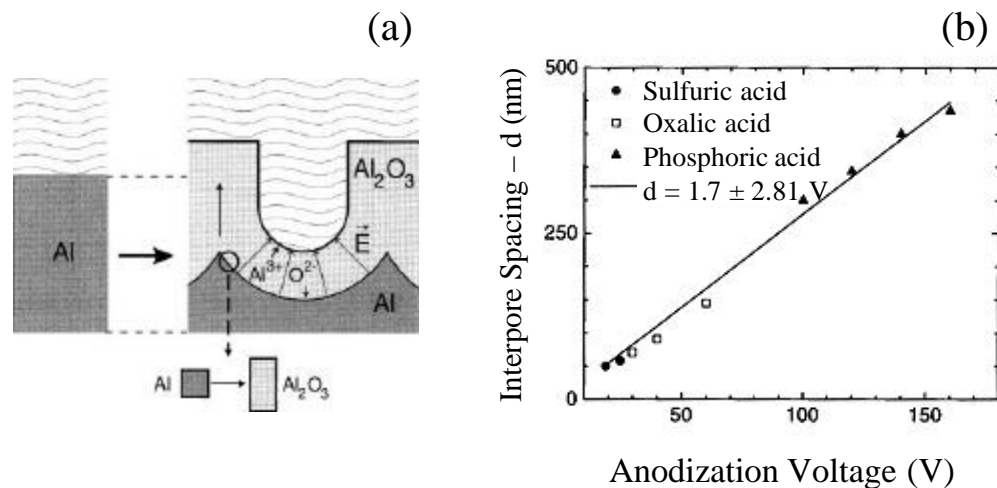


Figure 5.3: (a) Formation of pores during anodization process.[Jessensky,*et al.* 1998] (b) Variation of interpore spacing as a function of anodization voltage.[Li,*et al.* 1998]

foil was then mechanically polished with 6 μm diamond paste for 0.5 hour followed by a polishing step with 3, 1, and $\frac{1}{4}$ μm diamond paste, each step for 15 minutes. The Al foil was highly reflective after this step with some small grooves still visible on the surface. The Al foil was annealed for 2 hours at temperatures in excess of 250 $^{\circ}\text{C}$ to increase the average grain size in the foil. An electrochemical polish was performed in a 95 vol.% H_3PO_4 /5 vol.% H_2SO_4 /20 g/L chromic acid solution at 20 V and 85 $^{\circ}\text{C}$. In order to avoid excessive polishing, or surface pitting, the sample was examined every 5 seconds. This polishing step was performed for approximately 20 seconds total to obtain a mirror finish. Following the electrochemical polishing step, the sample was placed in water and the aluminum oxide layer on the surface was

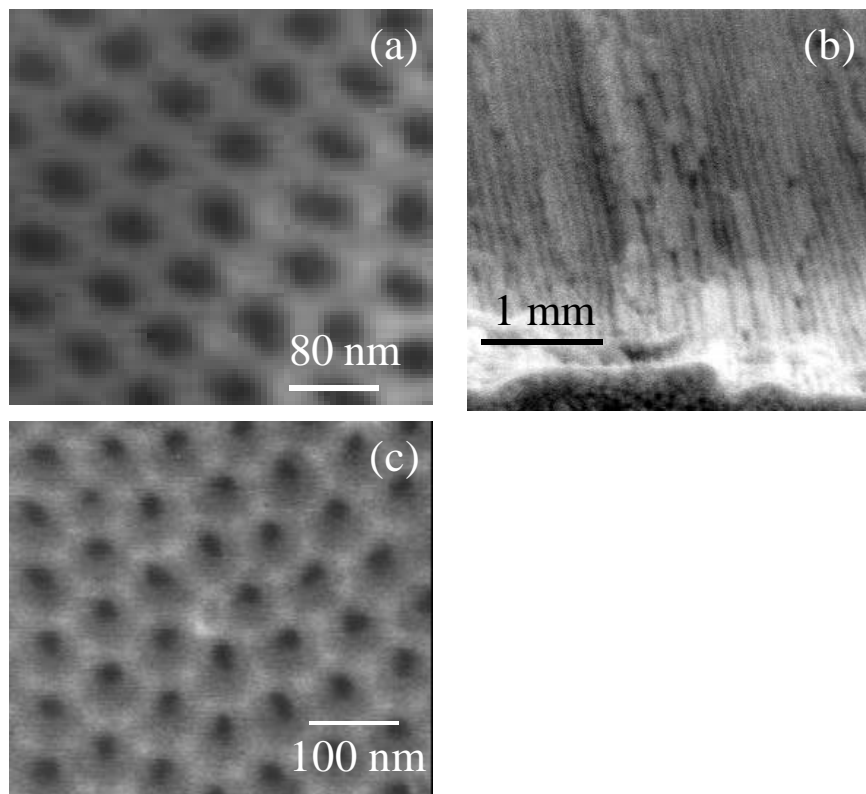


Figure 5.4: Alumina templates fabricated with (a) 45 nm pores at 20 V planar view, (b) cross-section and (c) 30 nm pores anodized at 15 V.

in a 3.5 vol.% H_3PO_4 /96.5 vol.% H_2O /45 g/L chromic acid solution for 2 minutes at 90 °C. Nail polish was applied on the edges of the sample to protect against preferential oxidation in the oxalic acid solution. When the nail polish dried, the sample was dipped in the oxide etching solution for 20 seconds and then dipped in water. The anodization process, Figure 5.3(a), was performed in a 4 wt% oxalic acid/ H_2O solution at 3°C and the applied voltage controlled the pore diameter, Figure 5.3(b). The first anodization step was performed for a

minimum of 3 hours. The optimal anodization time for forming hexagonally packed pores with the maximum ordered domain been determined to be approximately 12 hours.¹² The pores were disordered at the film surface with ordered pores at the alumina-aluminum interface. The alumina was then etched to expose the patterned Al surface. The anodization was then performed a second time to achieve highly ordered alumina templates. In Figure 5.4, some typical alumina templates were imaged in a scanning electron microscope at an accelerating voltage of 5 keV. The templates were fabricated using the above outlined procedure. In (a), the anodization voltage was 20 V and the second anodization step was performed for 3 hours. The pore diameter was measured as approximately 45 nm and the length was 3 μm . In (c), the pore diameter was measured as approximately 30 nm in diameter. This template was anodized at 15 V for one hour. The length of the pores was approximately 1 μm .

5.2.4 Sn nanowire fabrication

Before deposition of Sn on the surface of the alumina template, a pore widening step in 5 wt.% $\text{H}_3\text{PO}_4/\text{H}_2\text{O}$ was performed for 30 minutes. The alumina template was placed in an UHV chamber and was allowed to degas

¹² Unpublished work: Kornelius Nielsch of the Max Planck Inst Microstruct Phys, D-06120 Halle, Germany.

until the chamber pressure reached less than 8×10^{-10} Torr, which took approximately 1.5 hours. Sn was deposited on the template at room temperature using a Knudsen effusion cell with 99.9999% purity Sn. A high pressure vessel with the capability of achieving pressures up to 5000 psi and temperatures of 900 °C was used for the pressure injection of Sn. A high purity Ar gas was used to supply the pressure to the system. The sample was placed in the pressure vessel and the system was purged using the Ar gas. Two different methods for molten Sn injection into the porous alumina templates were investigated and are described following. In the first method, the system was sealed and Ar gas at 1800 psi was introduced at room temperature. The pressure vessel was heated to 470 °C that is beyond the melting temperature of Sn, 232 °C, and the pressure reached 3100 psi. In method 2, the pressure injection procedure was modified. A hydrogen-terminated Ge(001) wafer was placed on the Sn covered template and a block was placed on the back side of the Ge wafer. The Ge wafer served two purposes, that is, to keep the Sn layer in physical contact with the alumina template and to seed the nucleation of the α phase of Sn. In the pressure vessel, the sample was heated to the melting temperature of Sn, 232 °C, at atmospheric pressure. After 1 hour, Ar gas was introduced into the system to achieve a pressure of 1800 psi. The internal temperature of the pressure vessel was raised to 550 °C and the pressure increased to 2500 psi. In both methods, the internal

temperature of the pressure vessel was cooled over a 3 hour period. The sample was held at 10 degrees below the melting temperature of Sn for one hour for recrystallization.

5.2.5 Sn nanowire structural characterization

The Sn nanowires fabricated by pressure injection into porous alumina templates were analyzed in SEM and TEM. After fabricating a template using the procedure defined as method 1, the template was then cleaved open to image the cross-section shown in Figure 5.5. The accelerating voltage in SEM was 15 keV. Droplets of Sn with lateral dimensions on the order of 200 nm remained on the surface after pressure injection and the average length of the nanowires was measured as 300 nm, Figure 5.5(a). The diameter of the nanowire, 45 nm, appeared uniform along its length, and some nanowires grew to lengths of approximately 1 μm , Figure 5.5(c) and (d). Using method 1, Sn was injected into the pores but the filled area was less than 1%. Since Sn poorly wet the alumina surface, gaps between the Sn layer and the template surface may have allowed Ar gas into the unfilled pores. Hence the pressure differential, necessary for the injection of Sn, did not exist between the ambient and the pore. The second method produced a higher infiltration fraction. In Figure 5.6(a), an individual Sn nanowire with uniform 30 nm diameter and length of 1 μm was imaged in the

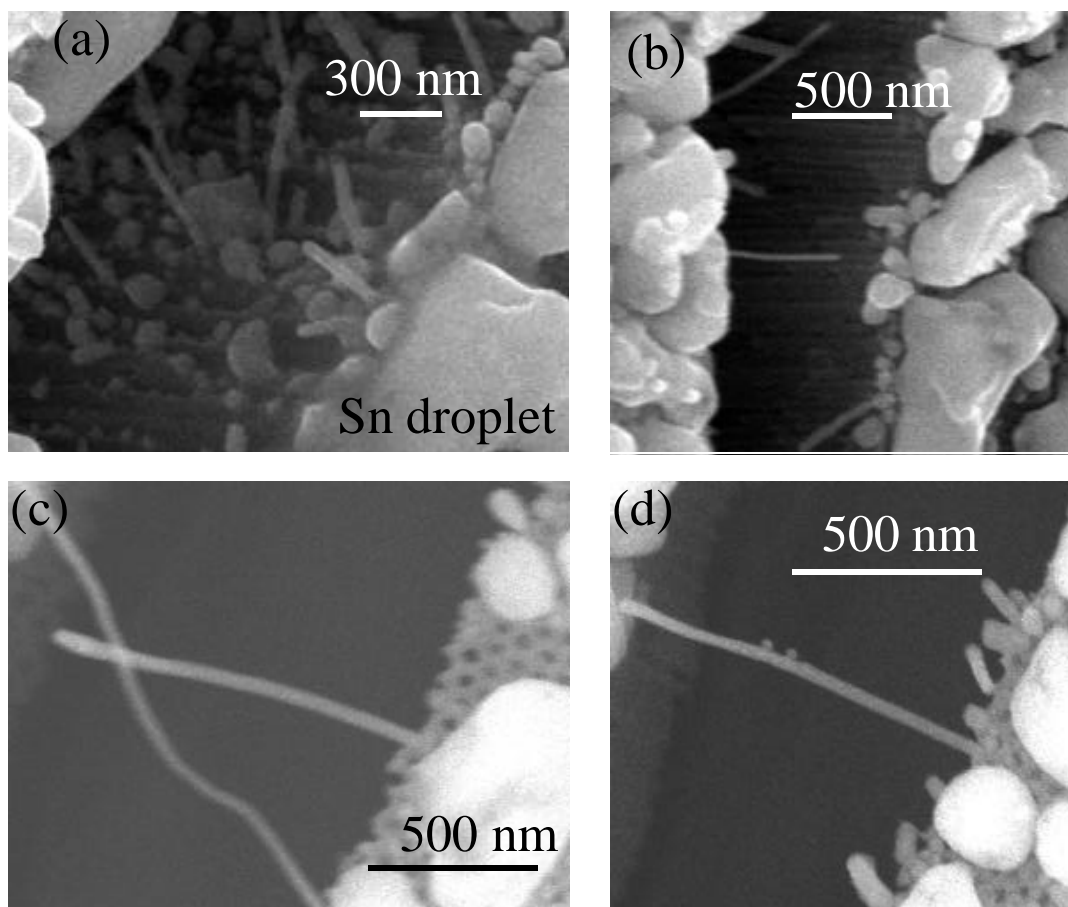


Figure 5.5: Sn nanowires in alumina templates fabricated by method 1. Images in (a) and (b) show the fraction of filled pores was less than 1%. In (c) and (d), 20 nm nanowires of lengths exceeding 1 μm are shown.

SEM. A cross-section imaged with nanowires still embedded in the alumina template demonstrated that some nanowires were injected in the pores but regions in the pores above the nanowires were empty. An abundance of residual Sn remained on the surface after the pressure injection, as seen in Figure 5.6. The

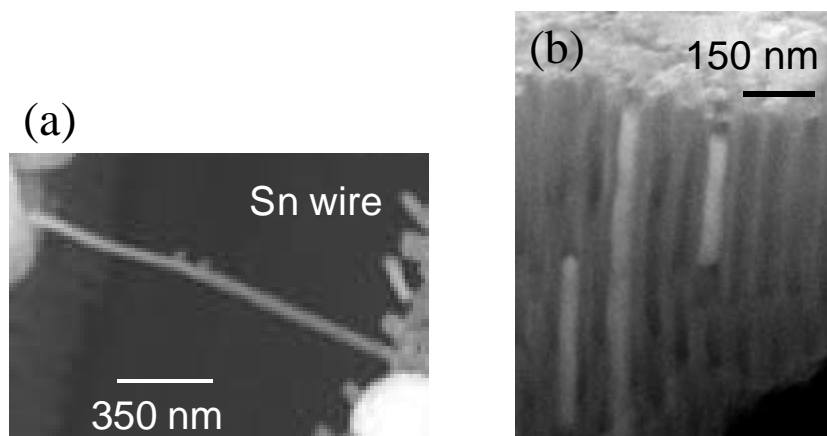


Figure 5.6: SEM images of Sn nanowires prepared by method 2: (a) individual nanowire and (b) nanowires embedded in alumina template.

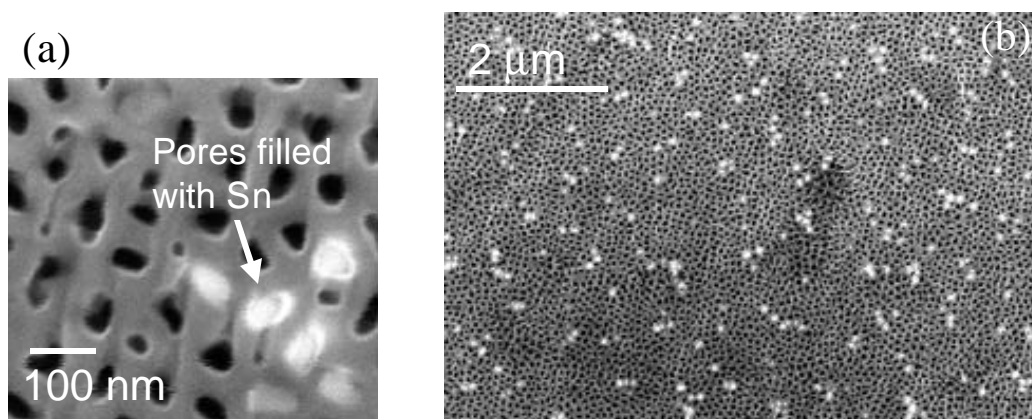


Figure 5.7: SEM images of templates after Sn pressure injection and Ar^+ ion etching.

incomplete infiltration was again attributed to the poor wetting properties of Sn on alumina. It may be possible to improve the wetting properties of the alumina surface by treating with a different electrolyte, such as H_2SO_4 .¹⁰ The excess Sn

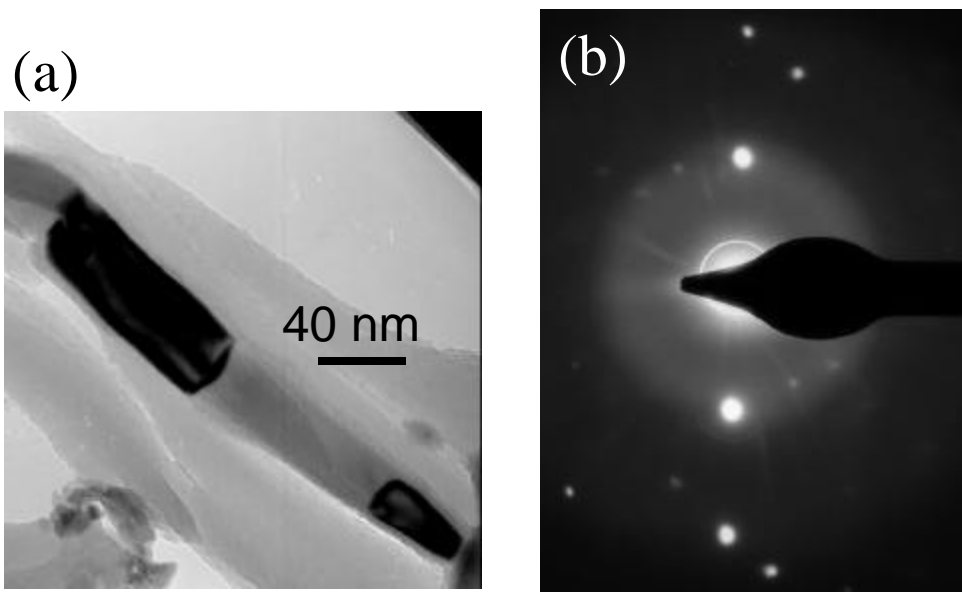


Figure 5.8: TEM analysis of single 40 nm nanowire: (a) dark regions corresponded to Sn and (b) the diffraction pattern demonstrated that the nanowire was a single crystal.

was removed from the surface by Ar^+ ion beam bombardment with an incident energy of 1.1 keV and an incident angle of 45 degrees for 3 minutes and 70 degrees for an additional 3 minutes. Some distortion of the surface occurred from the ion beam, seen in Figure 5.7 (a). The infiltration area was estimated as 10% from a planar view SEM image after Ar^+ ion etching, Figure 5.7 (b). The crystal structure of the Sn nanowires was characterized by TEM. In Figure 5.8(a), the TEM image demonstrated that the pressure injection method forced Sn to conform to the walls of the pores during solidification. The diffraction pattern of the nanowire demonstrated the nanowire recrystallized as a single crystal, Figure

5.8(b). Indexing of the reflections in this diffraction pattern showed that the Sn nanowire was in the β -phase. The sample was quenched on a cold stage in the electron microscope while taking diffraction patterns. Analysis of the diffraction patterns demonstrated the Sn nanowire did not transform to the α -phase when cooled to $T = -40\text{ }^\circ\text{C}$, below $13.2\text{ }^\circ\text{C}$ where the phase transition occurs in bulk Sn. The hindrance of the β to α phase transition has been reported for crystallites of less than 130 nm .¹¹ Furthermore, the placement of the Ge(001) hydrogen-terminated surface did not promote the nucleation of α -Sn in the pores. It is possible that Sn that was injected in the pores was not in contact with the Ge substrate during recrystallization. MBE growth of ultra thin α -Sn has been achieved on Si(001) substrates up to 1.3 monolayers in thickness.¹² Stabilization of the α phase may be achieved in a similar manner for nanowires. It has been reported that ordered pore arrays can be fabricated directly on Si(001) substrates by depositing an Al film, with thickness exceeding $20\text{ }\mu\text{m}$, on a Si(001).¹³ After template fabrication, the alumina barrier layer between the Si and the pore bottom can be removed by a series of electrical pulses¹⁴ leaving the Si surface exposed at the bottom of the pore. If preferential nucleation occurs at the Si substrate it may be possible to stabilize the α phase.

5.3 α -Sn quantum dots

5.3.1 Fabrication and structural characterization

Arrays of α -Sn quantum dots were embedded in epitaxial Ge(001) films by post-growth annealing of 1 μm thick, $\text{Sn}_x\text{Ge}_{1-x}$ films with $0.01 < x < 0.03$. The $\text{Sn}_x\text{Ge}_{1-x}$ films were grown by molecular beam epitaxy. The details of the deposition of the $\text{Sn}_x\text{Ge}_{1-x}$ films were given in section 2.2 of this thesis. The annealing furnace was first purged with dry nitrogen and then vacuum pumped with a turbo pump to 10^{-8} Torr before heating to prevent oxidation of the $\text{Sn}_x\text{Ge}_{1-x}$ sample. The dependence of the nanocrystal radius on the annealing temperature was investigated by annealing the $\text{Sn}_{0.03}\text{Ge}_{0.97}$ ¹³ sample at $T = 550, 650$ and 750 °C. The equilibrium solubility of Sn in Ge and Ge in Sn are both 0.005 at these temperatures.^{15,16} The Sn nanocrystals in the Ge matrix were characterized by cross-section TEM. Fourier transforms of high resolution TEM images of Sn nanocrystals were calculated to view the periodicity of the lattice fringes for a single nanocrystal, analogous to a diffraction pattern. From the diffraction pattern, the phase of the Sn nanocrystal was determined to be diamond cubic

¹³ This notation refers the average Sn composition in the alloy. The local composition fluctuates due to phase separation.

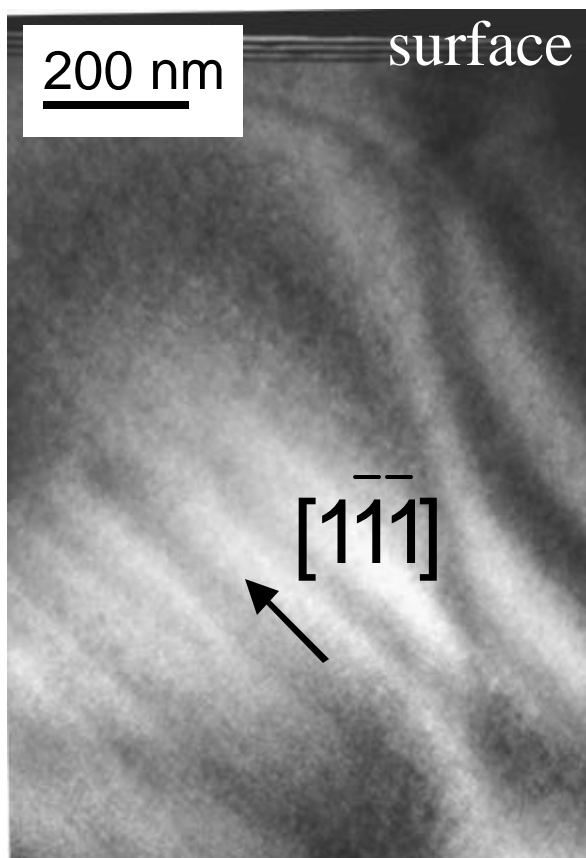


Figure 5.9: TEM image taken down the $[110]$ zone axis of $\text{Sn}_{0.01}\text{Ge}_{0.99}$ annealed at $T = 750\text{ }^\circ\text{C}$. Dark bands are seen to run along $[\bar{1}\bar{1}\bar{1}]$.

and the lattice constant revealed relaxation of the Sn nanocrystal in the Ge matrix.

A $\text{Sn}_x\text{Ge}_{1-x}$ alloy, with Sn composition of $x = 0.01$, was grown at a substrate temperature of $350\text{ }^\circ\text{C}$ and subsequently annealed at $T = 750\text{ }^\circ\text{C}$ for 30 minutes. The film was analyzed in cross-section TEM along the $[110]$ zone axis. The Sn composition in the alloy was near the equilibrium solubility limit, $x = 0.005$. Dark bands of contrast were observed along the $[\bar{1}\bar{1}\bar{1}]$ direction or along the $(\bar{1}\bar{1}0)$

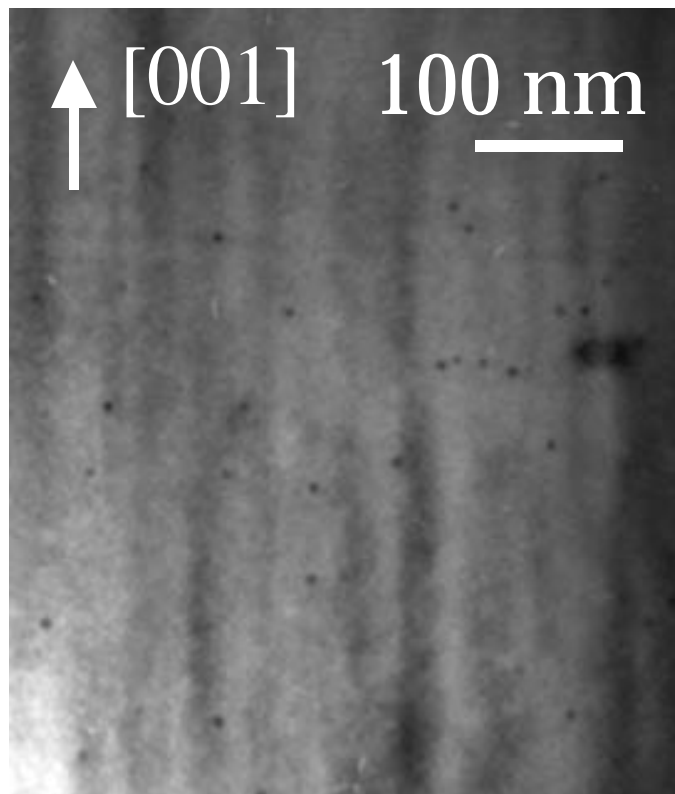


Figure 5.10: Cross-sectional TEM image down the [110] zone axis of a $\text{Sn}_x\text{Ge}_{1-x}$ film with $x = 0.03$ and annealed at $T = 550^\circ\text{C}$.

crystallographic planes, Figure 5.9. The period of the dark bands was measured to be 10 nm. Thus, Sn segregated along $\{110\}$ planes for compositions near the thermodynamic equilibrium solid solubility limit.

For the $\text{Sn}_{0.03}\text{Ge}_{0.97}$ film, cross-sectional TEM analysis was performed for the samples annealed at $T = 550^\circ\text{C}$ and 750°C . Both samples were annealed for 30 minutes. This $\text{Sn}_{0.03}\text{Ge}_{0.97}$ film was grown at 160°C and consisted of Sn enriched $\text{Sn}_x\text{Ge}_{1-x}$ rods oriented along $[001]$ ¹⁷ before annealing. Examination of Figure 5.10 revealed partial phase separation of Sn out of the Ge matrix occurred.

The average diameter of the Sn nanocrystals was measured as approximately 7 nm. At this annealing temperature of 550 °C, contrast along the [001] direction was observable indicating that some Sn remained in the $\text{Sn}_x\text{Ge}_{1-x}$ rods.

The same $\text{Sn}_x\text{Ge}_{1-x}$ sample was annealed at $T = 750$ °C and analyzed with TEM under $\bar{g} = [\bar{2}\bar{2}\bar{0}]$ 2 beam conditions, Figure 5.11. Dislocations were observed in the film confined to the region near the Ge substrate. Moiré fringes were discernable in some of the nanocrystals and were evidence of single crystallinity. By comparing with the sample seen in Figure 5.10, the size of the nanocrystals coarsened with the increased annealing temperature, 750 °C. The average nanocrystal radius was measured to be 16 nm. The diameter of the nanocrystals had an approximate 10% size variation around the average diameter, Figure 5.12.

High resolution TEM was performed on the sample that was annealed at $T = 750$ °C, shown in Figure 5.13. Two types of images of the nanocrystals are shown. In Figure 5.13(a), the cross-section has sliced the nanocrystal and in Figure 5.13(b), the nanocrystal is seen still embedded in the Ge matrix. In the second type of high resolution image, breaks in the lattice interference fringes were evidence of distortion of the Ge lattice around the Sn nanocrystals. Moiré fringes were also observed for the nanocrystals sliced by the cross-section. To examine the crystal structure of a single nanocrystal, a Fourier transform of the high-resolution image in Figure 5.13(a) was taken to obtain a diffraction pattern.

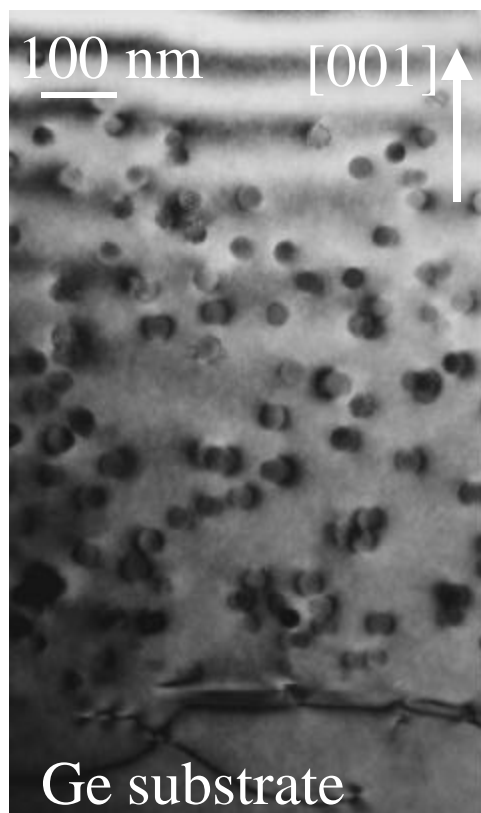


Figure 5.11: MBE Grown $\text{Sn}_x\text{Ge}_{1-x}/\text{Ge}(001)$ with average Sn composition of 3% annealed post-growth at $T = 750^\circ\text{C}$.

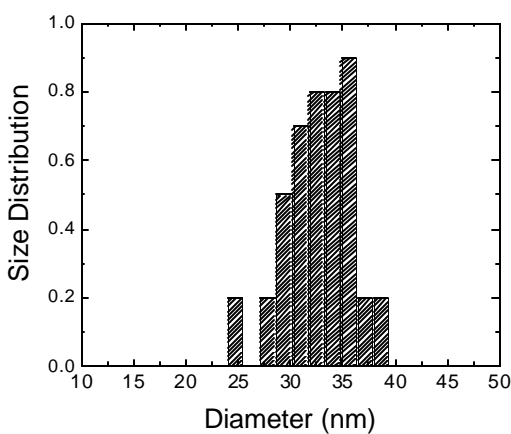


Figure 5.12: Size distribution of Sn nanocrystals in Ge matrix formed by post-growth annealing $\text{Sn}_{0.03}\text{Ge}_{0.97}/\text{Ge}(001)$ at $T = 750^\circ\text{C}$. The average nanocrystal diameter is 32 nm.

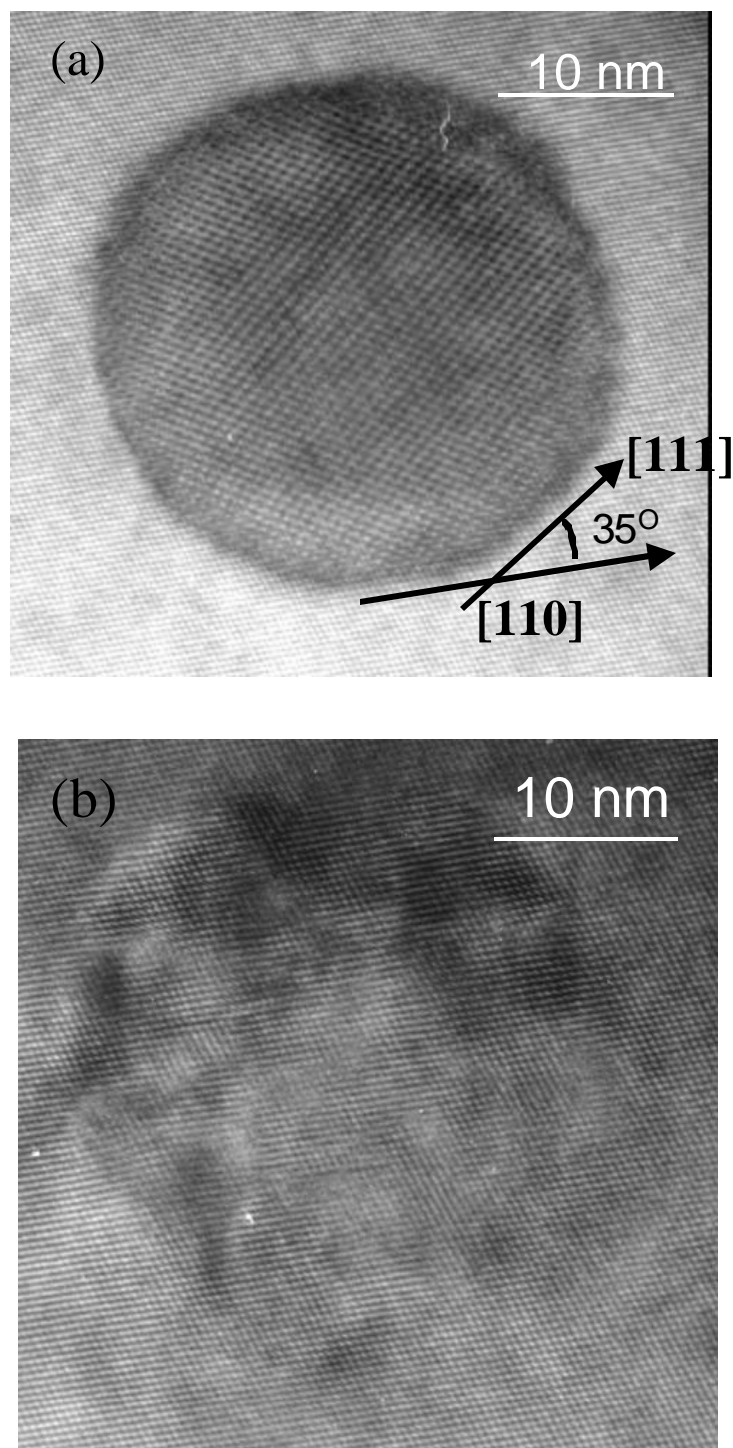


Figure 5.13: HR-TEM images down [110] zone axis of MBE grown $\text{Sn}_{0.03}\text{Ge}_{0.97}/\text{Ge}(001)$ annealed at $T = 750^\circ\text{C}$. (a) Cross-section slices a particle of diameter 28.4 nm and (b) a particle of diameter 26.5 nm is still embedded in the Ge matrix.

The diffraction pattern that is shown in Figure 5.14 consisted of reflections from both the Ge matrix and the Sn nanocrystal. In order to distinguish between the reflections associated with the Ge matrix and the Sn nanocrystal, a Fourier transform was taken of the high resolution image of the Ge matrix only. The Ge reflections were indexed, as indicated in Figure 5.15(a), and subsequently subtracted from the diffraction pattern shown in Figure 5.14. The inverse Fourier transform or back transform, in Figure 5.15(a), was then determined with the Ge reflections removed. The resulting image, Figure 5.15(b), obtained from the back transform included only lattice fringes from the Sn nanocrystal. The regions in the image that previously showed the Ge lattice fringes became blurred. The Ge lattice constant is well known; thus, the distance of the Ge reflections was used to calibrate the reflections observed in the Sn nanocrystal.

$$Rd_{hkl} = \lambda L \quad (51)$$

where R is the measured distance of the reflection from the center of the diffraction pattern, d_{hkl} is the interplanar spacing for planes (hkl) , and L is the camera constant or calibration factor determined from the Ge reflections. The diffraction pattern of the Sn nanocrystal (Figure 5.16) was indexed using equation (51). Table 5.1 lists the calculated value of the d -spacing for the reflections found in the diffraction pattern in comparison to the accepted values

of the d -spacing for α -Sn. The maximum and minimum values calculated for the d -spacing corresponded to the error in measuring the calibration constant in equation (51). The primary Sn reflections contributing to the lattice fringes seen in the HR-TEM image of Figure 5.13 were indexed as {110} planes. From the Sn (001) reflection and the Ge (002) reflection, a 5 degree tilt was observed between the Sn nanocrystal relative to the Ge matrix. Moiré reflections were also seen in the diffraction pattern. The distance of a Moiré reflection from the center was calculated for a 5 degree tilt and for a difference in lattice constants:

$$D = \frac{d_1 d_2}{\sqrt{(d_1 - d_2)^2 + d_1 d_2 \theta^2}} \quad (52)$$

where d_1 corresponded to the {111} lattice spacing of Ge, d_2 to the {110} lattice spacing of α -Sn and θ was the rotation angle between the two lattices. Using equation (52), the value for the spacing of the Moiré reflection was calculated as 11 Å, in agreement with the value calculated from the measured reflection. The lattice constants of the tetragonal (β) phase of Sn are 0.58317 and 0.31815 nm for the a and the c axes, respectively. The diffraction pattern analysis yielded a value for interplanar spacing of approximately 0.63 nm for one of the reflections; thus the Sn nanocrystal was not in the β phase. Based on the calculated values for the interplanar spacing from the reflections found in the diffraction pattern, the nanocrystal was determined to be the diamond cubic phase of Sn. The measured

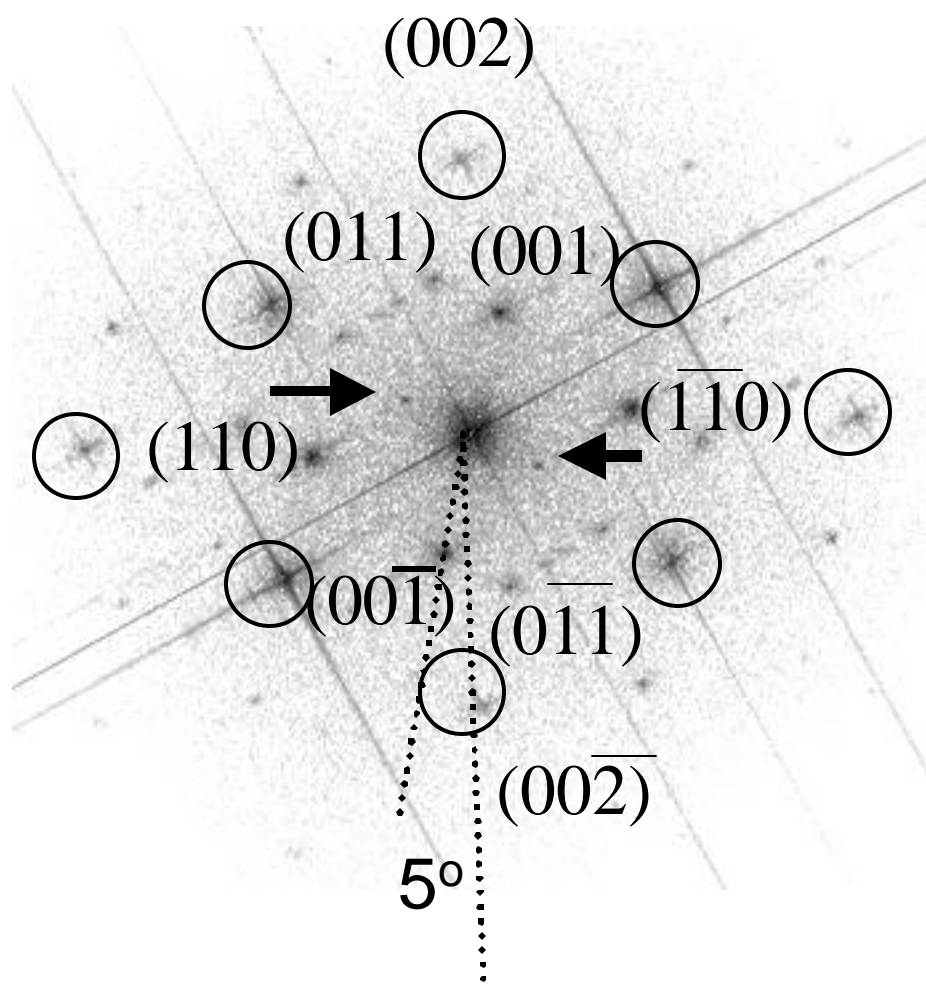


Figure 5.16: Indexed diffraction pattern of Sn nanocrystal observed in Figure 5.13. The Ge reflections are circled. A 5 degree tilt was observed along the [001] direction between the nanocrystal and the Ge matrix. Arrows point to Moiré reflections.

Meas. Reflection minimum (Å)	Meas. Reflection maximum (Å)	α -Sn: d-spacing (Å)	(<i>hkl</i>)
9.81	11.0	11	Moiré
6.06	6.53	6.489	(100)
4.58	4.86	4.59	(110)
3.3	3.45	3.24	(200)
2.33	2.42	2.29	(220)
2.04	2.11	2.05	(310)

Table 5.1: Interplanar spacing calculated from measured distance of reflection (columns 1 and 2) in comparison to known d_{hkl} spacing for α -Sn (column 3). The minimum (maximum) corresponds to the minimum (maximum) value calculated for the lattice spacing, taking into account measurement error.

interplanar spacing for the (200) and (220) reflections were slightly larger than the accepted values for the d -spacing of bulk Sn while taking into account measurement error. Nanocrystals of α and β Sn in Si have been reported to be under tensile strain and thus have a slightly larger lattice constant than observed in corresponding phase of bulk Sn.¹⁸

5.3.2 Optical characterization

Optical transmittance measurements were performed on the $\text{Sn}_{0.03}\text{Ge}_{0.97}$ samples before annealing and after annealing at $T = 550, 650$ and 750 °C using a Nicolet Magna 760 Fourier transform infrared (FT-IR) spectrometer. The system was purged with dry nitrogen to reduce IR absorption of H_2O and CO_2 found in the ambient. The transmittance measurements were taken between $1000\text{-}8000$ cm^{-1} at 300 K, Figure 5.17. The spot size of the beam was restricted to 5 mm by using a circular aperture. The optical transmittance was calculated by dividing by the through beam intensity through this aperture. The density of the α -Sn nanocrystals in the 1 μm thick film was estimated as 2% . From this value, the effective thickness of the α -Sn nanocrystals contributing to absorption of the infrared signal was estimated as 30 nm. A significant change in the transmittance curve was not evident until the annealing temperature was increased to 750 °C where an increase of absorption was observed near 4000 cm^{-1} . A decrease in the transmittance signal was observed with increasing annealing temperature. The difference in the transmittance signal below the energy bandgap between all the annealed samples was within the experimental error of the measurement, $\sim 1\%$. The decrease in transmittance between the annealed samples and the Ge substrate was not within experimental error and was attributed to free carrier absorption.

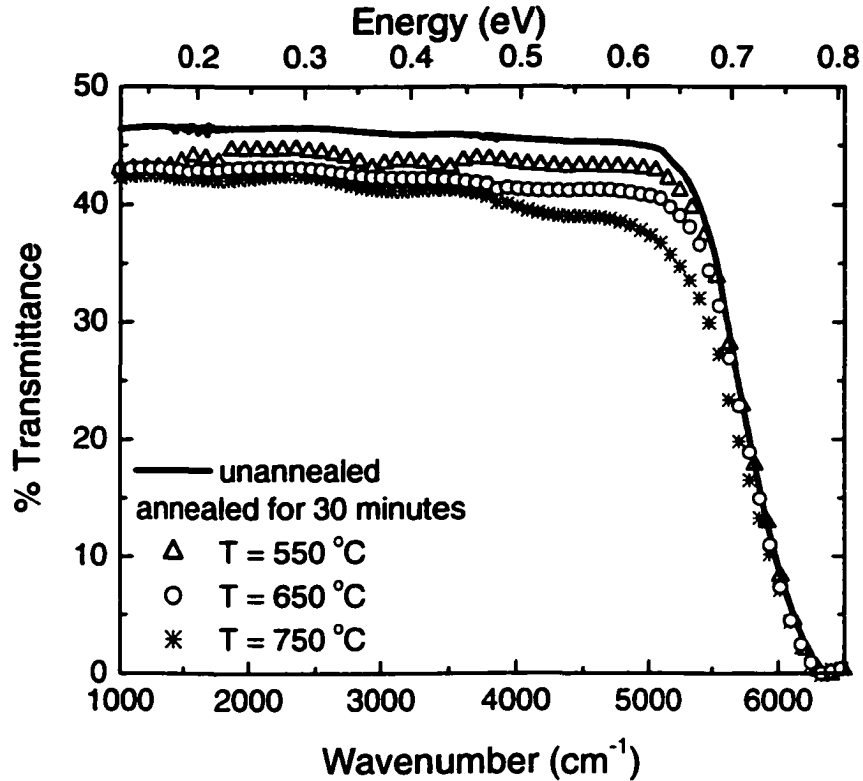


Figure 5.17: Transmittance versus wavenumber for $\text{Sn}_{0.03}\text{Ge}_{0.97}$: unannealed (line), annealed at $T = 550\text{ }^{\circ}\text{C}$ (circles), $650\text{ }^{\circ}\text{C}$ (crosses) and $750\text{ }^{\circ}\text{C}$ (triangles).

Using a commercial software package,¹⁴ the transmittance curve for the sample annealed at a temperature of $750\text{ }^{\circ}\text{C}$ was simulated between 3000 and 8000 cm^{-1} . The extinction coefficient and refractive index were varied to iteratively fit the simulated transmittance curve with the experimental spectrum. Once the best fit was obtained, the simulation results for the dispersion

¹⁴ SCI, Optical Thin Film Software

relationship for the extinction coefficient (k) was used to calculate that of the absorption coefficient (α):

$$\alpha(\omega) = 2\omega k(\omega) \quad (53)$$

where ω is the frequency in wavenumbers. Under a parabolic band approximation, the absorption edge has a power dependence on the direct energy bandgap of 0.5, and on the indirect energy bandgap of 2.¹⁹ The absorption versus wavenumber spectra generated by the best fit of the simulation with the experimental transmittance curve was fit to the functional form of the absorption coefficient using the parabolic band approximation. An Urbach tail was included in the functional form of the absorption coefficient to take into account defect states in the energy bandgap due to defects at the Sn-Ge interface.²⁰ In Figure 5.18, the absorption coefficient generated from the simulation (closed triangles) and the functional form of the absorption coefficient (open circles) are shown. The fit of the absorption coefficient was insensitive to the indirect energy gap but very sensitive to the direct energy gap contribution and the Urbach tail. The absorption coefficient was $3 \times 10^3 \text{ cm}^{-1}$ near the bandgap edge. The best fit to the absorption coefficient versus wavenumber spectrum using this method generated a value of 0.45 eV for the direct bandgap energy.

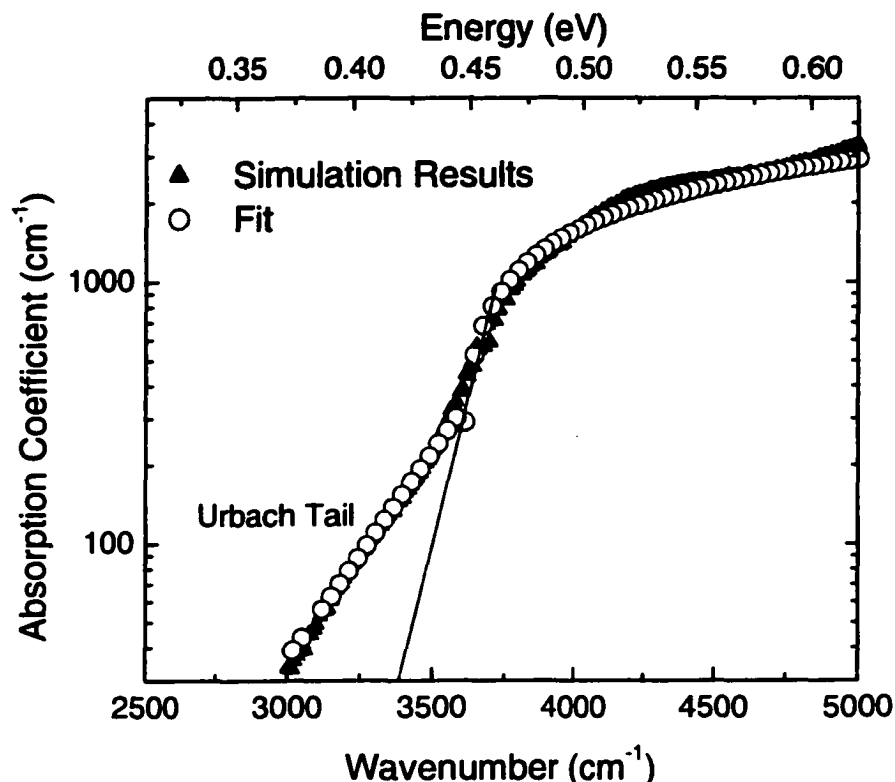


Figure 5.18: Absorption coefficient versus wavenumber calculated from best fit of simulation with experimental transmittance spectra (closed triangles) and the fit (open circles) using the functional form of the absorption coefficient for $\text{Sn}_{0.03}\text{Ge}_{0.97}$ annealed at $T = 550\text{ }^{\circ}\text{C}$.

5.4 Conclusion

β -Sn nanowires were fabricated in anodic alumina templates with lengths exceeding $1\text{ }\mu\text{m}$ and diameters on the order of 40 nm . Anodic alumina templates can be fabricated with ordered domains of hexagonally packed pores greater than $1\text{ }\mu\text{m}$ and pore densities on the order of 10^{11} cm^{-2} . High pressure injection of Sn into the pores was achieved with a filling fraction of 10%. The filling fraction may be improved by anodization in H_2SO_4 or with higher pressures.¹⁰ The

fabrication of the desired diamond cubic (α) phase of Sn in the nanowires was not achieved. It may be possible to stabilize the α phase by preferential nucleation of the nanowires on a Si(001) surface during recrystallization. It may be necessary to preferentially cool the Si substrate during recrystallization to achieve heterogeneous nucleation on Si instead of on the alumina walls. Nevertheless, the concept of single crystal nanowire fabrication using a pressure injection method has been demonstrated for Sn in porous alumina templates.

The fabrication of α -Sn quantum dots was achieved. By annealing 1 μm thick $\text{Sn}_x\text{Ge}_{1-x}$ films with $x = 0.03$ at $T = 750^\circ\text{C}$, 32 nm diameter quantum dots were fabricated with a 10% size variation. Optical transmittance measurements were performed on a 1 μm thick sample with 2% volume density of α -Sn quantum dots embedded in Ge. The transmittance spectra was simulated to obtain an experimental value of the absorption coefficient versus wavenumber. By modeling of the absorption edge, quantum confinement effects were seen to open the bandgap of the semi-metal to 0.45 eV. The value of the absorption coefficient near the bandgap was $3 \times 10^3 \text{ cm}^{-1}$. In summary, Quantum confinement effects were observed for quantum dot diameters on the order of 30 nm.

5.5 Bibliography

1. D. W. Jenkins and J. D. Dow, *Phys. Rev. B* **36**, 7994 (1987)
2. B. Bouhafs, F. Benkabou, M. Ferhat, B. Khelifa, J. P. Dufour, and H. Aourag, *Infrared Phys. & Tech.* **36**, 967 (1995)
3. V. Sih, senior thesis (Caltech, Pasadena, 2001).
4. C. Delerue, G. Allan, and M. Lannoo, *Phys. Rev. B* **48**, 11024 (1993)
5. N. A. Hill and K. B. Whaley, *Phys. Rev. Lett.* **75**, 1130 (1995)
6. H. Masuda and K. Fukuda, *Science* **268**, 1466 (1995)
7. F. Keller, M. S. Hunter, and D. L. Ronginson, *J. Electrochem. Soc.* **100**, 411 (1953)
8. R. J. Tonucci, B. L. Justus, A. J. Campillo, and C. E. Ford, *Science* **258**, 783 (1992)
9. T. W. Whitney, J. S. Jiang, P. C. Searson, and C. L. Chien, *Science* **261**, 1316 (1993)
10. Z. Zhang, J. Y. Yang, and M. S. Dresselhaus, *J. Mat. Res.* **13**, 1745 (1998)
11. D. R. G. Mitchell and S. E. Donnelly, *Philosophical Magazine A* **63**, 747
12. K. S. Min and H. A. Atwater, *Appl. Phys. Lett.* **72**, 1884 (1998)
13. S. Shingubara, O. Okino, Y. Murakami, H. Sakaue, and T. Takahagi, *J. Vac. Sci. Tech. B* **19**, 1901 (2001)
14. K. Nielsch, F. Muller, A. Li, and U. Gosele, *Adv. Mat.* **12**, 582 (2000)
15. C. D. Thurmond, *J. Phys. Chem* **57**, 827 (1953)

16. C. D. Thurmond, F. A. Trumbore, and M. Kowalchik, *J. Chem. Phys.* **24**, 799 (1956)
17. R. Ragan, C. C. Ahn, and H. A. Atwater, manuscript in prep. (2001)
18. M. F. Fyhn, J. Chevallier, A. N. Larsen, R. Feidenhans's, and M. Seibt, *Phys. Rev. B* **60**, 5770 (1999)
19. J. I. Pankove, *Optical Processes in Semiconductors* (Dover, New York, 1971).
20. A. Iribarren, R. Castro-Rodríguez, V. Sosa, and J. L. Peña, *Phys. Rev. B* **58**, 1907 (1998)

Chapter 6 Conclusions

A significant amount of challenges lies in the road ahead for the incorporation of novel materials with Si ULSI. The goal of this thesis was twofold; the fabrication of novel nanostructures from Si-compatible materials and the investigation of the optical properties of such nanostructures.

The $\text{Sn}_x\text{Ge}_{1-x}$ alloy system was chosen for the unique property of an indirect to direct energy bandgap transition in a group IV alloy. Previous work on relaxed $\text{Sn}_x\text{Ge}_{1-x}/\text{Si}(001)$ heterostructures demonstrated the occurrence of this transition at approximately 10% Sn composition. In order to investigate the feasibility of utilizing this material in device applications, higher quality material was necessary. In Chapter 2 of this thesis, the ability to grow coherently-strained $\text{Sn}_x\text{Ge}_{1-x}/\text{Ge}$ superlattices and single layer $\text{Sn}_x\text{Ge}_{1-x}$ epitaxial films on $\text{Ge}(001)$ substrates was demonstrated. The growth temperature was optimized to maximize the thickness for coherent epitaxial growth and to eliminate Sn surface segregation. The coherently-strained $\text{Sn}_x\text{Ge}_{1-x}$ epitaxial films exceeded a predicted thermodynamic critical thickness for relaxation. Yet, the film thickness was less than necessary for fabrication of an infrared detector. Future work may include growing Sn composition graded layers to achieve the thickness necessary for optoelectronic device applications.

The perturbation of the electronic structure resulting from coherency strain was studied both experimentally and theoretically to determine if further manipulation of the bandstructure was possible and this work was described in Chapter 3. Using deformation potential theory, $\text{Sn}_x\text{Ge}_{1-x}/\text{Ge}(111)$ was not predicted to undergo an indirect to direct bandgap transition due to coherency strain. The deformation potential model also predicted that coherency energy had little effect on the overall energy of the $\text{Sn}_x\text{Ge}_{1-x}/\text{Ge}(001)$ bandgap and this was confirmed experimentally.

In Chapter 4, The phenomenon of phase-separation during dynamic growth of thick $\text{Sn}_x\text{Ge}_{1-x}$ films was described. 1 μm thick $\text{Sn}_x\text{Ge}_{1-x}/\text{Ge}(001)$ epitaxial films with $0 < x < 0.085$ that evolved during growth into a dense array of Sn enriched $\text{Sn}_x\text{Ge}_{1-x}$ nanowires oriented along [001] were characterized. The phase-separation was correlated with a surface undulation and the fastest growing wavelength of the growth instability was measured. The experimental value was compared to a thermodynamic and kinetic model. The kinetic model yielded a value for the instability wavelength with much better correlation with the experiment than the thermodynamic model. Parameters such as surface diffusion and incoming flux appeared to dominate the period of the phase-separation. These two parameters can be controlled during growth with temperature and growth rate.

Optical transmittance measurements were performed on thick phase-separated $\text{Sn}_x\text{Ge}_{1-x}$ films with Sn composition between $0.05 < x < 0.085$. The energy bandgap was found to decrease with increasing Sn composition as in previous work. Unique to this work, we have determined that the energy bandgap decreased for the thicker phase-separated films and the absorption edge exhibited a sharp increase that is characteristic of a direct energy bandgap for the $\text{Sn}_{0.07}\text{Ge}_{0.93}$ alloy film.

β -Sn nanowires were fabricated in anodic alumina templates with lengths exceeding $1 \mu\text{m}$ and diameters on the order of 40 nm . Anodic alumina templates can be fabricated with ordered domains of hexagonally packed pores greater than $1 \mu\text{m}$ and pore densities on the order of 10^{11} cm^{-2} . High pressure injection of Sn into the pores was achieved with a filling fraction of 10%. The filling fraction may be improved by anodization in H_2SO_4 or with higher pressures. The fabrication of the desired diamond cubic (α) phase of Sn nanowires was not achieved. It may be possible to stabilize the α phase by preferential nucleation of the nanowires on a Si(001) surface during recrystallization. Alumina templates can be fabricated on Si(001) substrates by depositing Al layers exceeding $20 \mu\text{m}$ in thickness. It may be necessary to preferentially cool the Si substrate during recrystallization to achieve heterogeneous nucleation on Si instead of on the alumina walls.

The fabrication of α -Sn quantum dots was achieved. By annealing 1 μm thick $\text{Sn}_x\text{Ge}_{1-x}$ films with $x = 0.03$ at $T = 750\text{ }^\circ\text{C}$, 32 nm diameter quantum dots were synthesized with a 10% size variation. Quantum confinement effects were seen to open the direct energy bandgap of the semi-metal to 0.45 eV. The value of the absorption coefficient near the bandgap was $3 \times 10^3\text{ cm}^{-1}$.